TESI DI DOTTORATO

UNIVERSITÀ DEGLI STUDI DI NAPOLI "FEDERICO II"

DIPARTIMENTO DI INGEGNERIA ELETTRICA
E DELLE TECNOLOGIE DELL'INFORMAZIONE

DOTTORATO DI RICERCA IN
INGEGNERIA ELETTRONICA E DELLE TELECOMUNICAZIONI

NON-LOCAL METHODS FOR INSAR PARAMETERS ESTIMATION

FRANCESCOPAOLO SICA

Il Coordinatore del Corso di Dottorato
Ch.mo Prof. Daniele RICCIO

Il Tutore
Ch.mo Prof. Giovanni POGGI

Il co-tutore
Dr. Ing. Gianfranco FORNARO

A. A. 2015–2016

to Gino, Gena e Maria

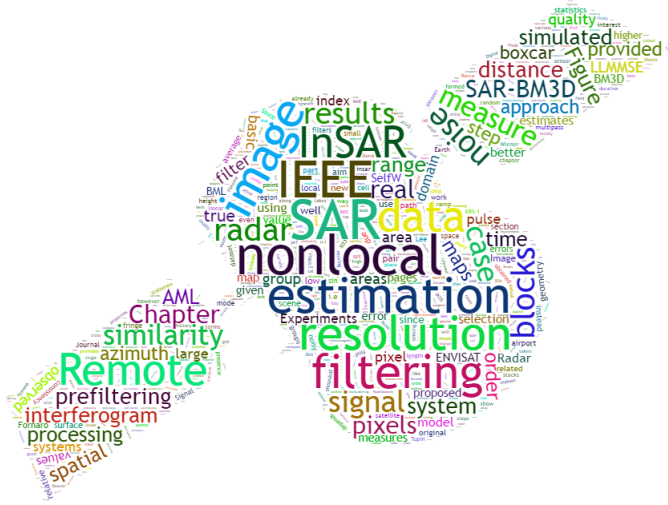

Figure 0.1: The thesis in short (www.wordcloud.com).

Contents

Introduction

Latest Remote Sensing technologies are having great impact on both research and applications. Differently from some years ago, when technological development was achievable only for large institutions, like space agencies, today the number of private companies developing and operating their own acquisition systems is increasing quickly. This trend is also due to the fact that the imaging system technology is becoming mature allowing for incremental improvements regarding performance and low-size/weigth implementation. A further enabling factor has been the evolution of image processing methodologies, with ever more powerful and effective tools, which made possible the development of new systems and even the creation of features and applications that were not imagined at the time of the system realization.

There are many remote sensing modalities, the most popular of which are related to optical, hyperspectral and radar sensors, each of them with specific peculiarities and purposes. For example, optical sensors have by design a higher resolution with respect to radar sensors due to their operative range frequency. But for the same reason they suffer from possible atmospheric occlusions, while the radar sensors do not.

Among the radar systems, the Synthetic Aperture Radar (SAR) has experienced an increasing popularity in the last decades, especially for Earth Observation purposes. Since the first missions, it demonstrated its effectiveness in providing reliable information about the

Earth's surface such as topography, morphology, roughness and dielectric characteristics of the backscattering layer. In fact, SAR systems demonstrated to possess many useful features, that made the difference compared to competitor systems. Since they operate in the microwave frequency range and provide their own illumination, SAR systems can operate almost independently of meteorological conditions and sun illumination. Geometric resolutions in the order of some meters are achieved with physical antennas of limited size, thanks to the synthetic aperture concept and to pulse compression techniques. The price to pay for these desirable properties is in the high transmit power, the considerable amount of signal processing required and, compared to optical imagery, the "unconventional" imaging geometry, as it will be shown in chapter 1.

Spaceborne remote sensing systems travel around the Earth over polar orbits at an altitude going typically from $200\,Km$ (space shuttle) to $800\,Km$ (satellites) at inclinations ranging from 57° to 108°. The SAR system ENVISAT, for example, has a spatial resolution in the order of $5\,m$ in azimuth and $25\,m$ in ground range, while most recent systems as TerraSAR-X and COSMO-SkyMed can reach a resolution of few meters. The imaged swath is about $50 - 100\,Km$ wide in standard imaging mode and up to $500\,Km$ with ScanSAR systems.

SAR Interferometry (InSAR) is today one of the most used techniques exploiting SAR imagery. Any image is a bidimensional representation of some features of interest. SAR interferometric images, in particular, measure the height information over the scene. They are generated by processing a pair of SAR images acquired from slightly different points of view, giving rise to the so called Digital Elevation Map. As it will be widely shown in chapter 2, the height information is codified in the *interferometric phase*, i.e. the phase difference between the two images. Going a step further, Differential InSAR (DInSAR) is

a tool for detection and mapping of terrain displacements over wide areas, with a precision comparable with fractions of the operative wavelength: millimeter range in case of X-band SAR. This is of great importance for risk management as in case of earthquakes or volcanic activity, for glaciology and ice sheet monitoring, for studying tectonic processes and monitoring ground subsidence due to mining, gas, water and oil withdrawal, etc..

The use of spaceborne SARs as interferometers became popular only in the last decades, although the basic principle dates back to the early 1970s. However, it was only in the early 90s that the first results on terrestrial applications were published. Before 1992 SAR data were only available to a limited group of scientists, the required data elaboration was expensive, and appropriate facilities existed only at few research centers. Interferometry data-sets became available to a larger set of researcher thanks to the ESA satellite ERS-1 launched in 1991. It provided a huge amount of SAR data-sets and a series of research groups began to investigate the method intensively and with success [3].

On July 08, 1993, the journal *Nature* showed to a wide public the first differential interferogram representing the deformation induced by the earthquake that affected the Californian area of Landers on June 28, 1992. The interferogram was produced by combining the pair of ERS-1 SAR images taken before (April 24, 1992) and after (August 7, 1992) the seismic event. This event was claimed as the first picture of an earthquake.

The ERS-1 satellite was followed by the twin ERS-2 in 1995. They weren't the first radars to introduce data suitable for interferometry, but they achieved the real breakthrough in SAR interferometry. The reason of their success was primarily due to the excellent results

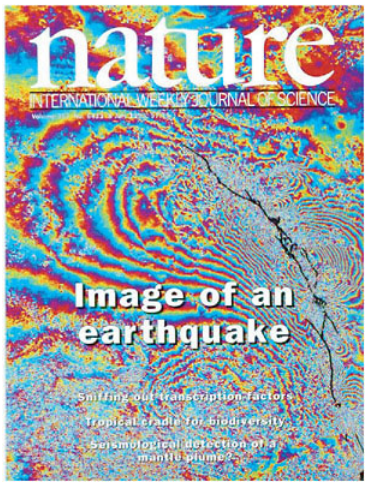

Figure 0.2: Cover of the journal Nature showing the first-ever image of an earthquake.

achieved in the area of repeat-pass interferometry. In fact the satellite orbit was very stable and it was determined with *cm* accuracy, the baseline control was very good and many orbit pairs met the baseline conditions for repeat-pass interferometry. ERS-2 was identical to ERS-1, had the same orbit parameter, and continued the ERS-program with the 35-days repeat period. This mission provided outstanding InSAR performance in the TANDEM mission where ERS-1 and ERS-2 were operated in parallel, reaching high coherence orbit pair. In fact ERS-2 followed ERS-1 on the same orbit at a 35 min delay thus, considering Earth's rotation, this orbit scenario assured that ERS-1 and ERS-2 imaged the same areas at the same look angle at a one day time lag. The orbits were deliberately tuned slightly out of phase such that a baseline of some hundreds meters allowed for cross-track interferometry. This separation between ERS-1 and ERS-2 could be kept very stable, because both satellites were affected by similar disturbing forces. The one day time lag was the key feature to

obtain high coherence interferograms and no other repeat-pass system could achieve it.

Nowadays, the latest SAR systems work in the X-band of the electromagnetic spectrum, that is with a wavelength of about 31 mm and provide images with a resolution of up to 1 m with revisit time of a few days. Today the major operational X-band SAR systems are the german TerraSAR-X and the italian COSMO-SkyMed. The former was launched on June 15, 2007 and has been in operational service since January 2008. As for ERS systems a second sister satellite TanDEM-X was launched in early 2010 and nowadays the two satellites act as a pair with the aim of Earth's Digital Elevation Model (DEM) reconstruction. The latter, COSMO-SkyMed, is a constellation composed of four satellites equipped with SAR sensors. The first satellite of COSMO-SkyMed constellation was launched on June 2007 whereas the full constellation is operational since 2010.

With SAR technology development, the need for digital signal processing and enhancement tools grew fast. One of the first application was the *despeckling*: the procedure of removing the *speckle* from the amplitude of the SAR images. Due to the presence of many single scattering mechanisms in the SAR resolution cell, the backscattered field results in a coherent superimposition of complex phasors that gives rise to constructive and destructive interference phenomena. From one resolution cell to the adjacent, the interference mechanism can vary completely implying a spatial amplitude variation even for areas with constant backscattering characteristics. The speckle phenomena is normally indicated as pseudo-noise, since it is a disturb that impairs the measured signal quality, but, at the same time, it is intrinsic of any coherent measurement system. In SAR images, the speckle impairs the visual interpretation and the performance of subsequent processes like image segmentation and classification. Many despeckling algo-

rithms have been proposed in the last decades [19, 38, 39, 53, 59, 62–64, 70, 71, 84].

In SAR Interferometry, the enhancement of the interferometric signal is a preliminary step for almost any application. The disturb in this case is mainly given by the degree of dissimilarity between the two images. The amplitude of the *normalized complex correlation* between the pair, the *coherence*, measures the degree of similarity between the two images while its argument is the interferometric phase. The estimation of the correlation allows to obtain first an estimation of the phase itself and secondly a measure of the reliability of the estimated phase through the coherence parameter. The classical approach for estimating the complex correlation index ia a moving-average filtering, which, assuming that the interferometric phase has slow spatial variations or, from a statistical point of view, it is locally a Wide-Sense-Stationary (WSS) process, turns out to be the Maximum-Likelihood estimator [95]. Such a filter has to trade off the low estimation variance, achievable with a large window, with image resolution. The resolution loss is due to a mix of heterogeneous contributions which takes place whenever the signal is not locally WSS as in the case of boundaries between regions with different backscattering characteristics, e.g. the edge between a field and a street. The work in InSAR parameter estimation has then mainly focused on improving this trade-off by trying to achieve a strong filtering intensity also in non-stationary areas. Back in the '90s, the Lee [67] and Goldstein [49] filters provided two different solutions working in the spatial and frequency domain, respectively. The former adapts the shape of the filtering window to the local phase edges. The latter, instead, enhances the useful spectrum components, assuming that the non-stationary signal is defined in a narrow band while the noise spreads over the whole spectra. The solutions proposed during last decades can be divided as well in spatial

and transform domain approaches. The state-of-the-art filters [20, 22] extend the ML estimation to a weighted average in the framework of the nonlocal filtering. This paradigm, rather than using the geometrically closest pixels as in the moving average, selects the pixels that are more similar to the target pixel enforcing in this way the stationarity hypothesis on the average group. In [20, 22] new similarity measures are defined to deal with the InSAR statistic and perform then a Weighted-ML estimation.

In this thesis work the nonlocal paradigm has been investigated in the framework of Multitemporal SAR Interferometry, e.g. Differential Interferometry, Tomography, etc., and single InSAR pair, e.g. DEM generation. In the former, Adaptive Multi-Looking methods have been developed for the generation of interferometric data-stacks. Following the nonlocal approach, the proposed methods rely only on similar pixels according to a suitable similarity measure that exploits the stack's temporal information. An hybrid approach that jointly uses the nonlocal paradigm and transform domain filtering has been investigated for InSAR pair phase estimation. On the track of the BM3D [16] and SARBM3D [84] algorithms, different approaches to the filtering in the transform domain are investigated. Furthermore, a novel approach to the similarity computation and filtering, based on a relative-topography content of the interferometric phase rather than its absolute value, is proposed.

The thesis is organized as follows: chapter 1 introduces to the SAR acquisition system, its resolution and main working principles. In chapter 2 the basic concepts of Interferometry are provided, together with its geometry and its various applications. The problem of InSAR parameter estimation is described in chapter 3, presenting several state-of-the-art filters. Chapter 4 and Chapter 5 describe the research work carried out on InSAR parameter estimation in the context of

Multitemporal and single-pair Interferometry, respectively. Finally, in chapter 6, the main results are summarized and commented, and future work is outlined.

1 Synthetic Aperture Radar

1.1 Overview

The Synthetic Aperture Radar (SAR) is a system that operates in the microwave domain at the aim of acquiring images of the terrestrial surface. The SAR is an active system, in the sense that it provides its own source of radiation, meaning that it can acquire images during both day- and night-time. The microwave operative range lend to the system the ability of watching through clouds and other atmosferic disturbs, since these are practically invisible at this frequency range. The ability of acquiring independently from sunlight and weather conditions made the SAR being very attractive for remote sensing pourposes. During last decades the SAR became a wide spreaded tool complementary to others as the optical and multi/hyper-spectral imaging systems. Clearly, there are other important characteristics as the *coherent receiving* of the backscattered signal: the capability of mesuring the signal in its amplitude and phase. The phase information allows, from at least a pair of acquisitions, to measure the altitude of the imaged area (*Digital Elevation Model* - DEM) or detect ground deformation over time of the order of centimeter (*Deformation Monitoring*)[14]. This applications, that are named respectively *Interferometry* and *Differential Interferometry,* will be shown in details in the next chapter.

In the following, with reference to Fig. 1.1, the simplest SAR acquisition geometry is depicted in order to show the basic SAR working principles and its prime characteristics. The radar is carried on a moving platform that can be an aircraft or a satellite moving at speed V in a straight trajectory at constant altitude H. The commonly used SAR acquisition mode is the strip-map mode as the one in Fig. 1.1, but other SAR mapping modes are of interest: Spotlight and ScanSAR, that differ from the standard strip-map respectively for the improved resolution and for the wider achieved coverage. In addition there is the most recent TopSAR mode that tries to trade off the benefits coming from the last two mentioned modes. In this context only the standard strip-map mode is used to present the SAR working principles.

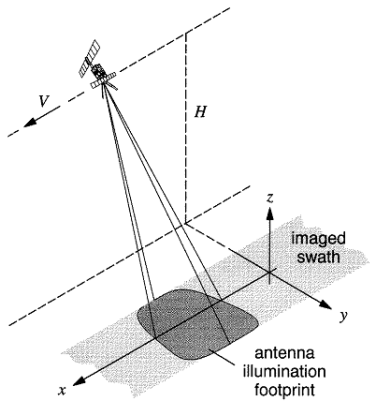

Figure 1.1: SAR imaging geometry [3].

The sensor is moving along its assumed straight path, i.e. the *azimuth* direction and it sends pulses at its *pulse repetition frequency (prf)* and receives coherently the echoes scattered from the Earth's surface. Each transmitted pulse sweeps across the swath at the velocity of light c and simultaneously the scene is scanned along the azimuth direction at the radar flight speed V. Since the two timescales differ

of several grade of magnitude, the two mechanisms can be considered indipendently. The *start-stop approximation is usually* assumed: the radar occupies only some positions in space along its flight path, when the radar sends the pulse it is considered motionless: it waits to receive the scattered echo and then move to the next position. This simplifies the analytical system description and suggests arranging the received echoes *side-by-side* to form a raw data matrix. The raw data acquired by a coherent radar resemble to an hologram rather than an image and hence, require a considerable amount of signal processing for image formation, these procedures are indicated in one term as *focusing*. The coordinates of the 2D focused SAR image are *range* r for the distance of the scattered object from the radar and *azimuth* x for the position of the scatterer along the sensor path. The value of the SAR image in the pixel (x, r) depend from the points belonging to the observed scene at coordinates (x', r') through the following expression:

$$u(x,r) = \iint\limits_{\triangle x \triangle R} u(x',r')\, e^{i\phi(x',r')} sinc(x'-x)\, sinc(r'-r)\, dx' dr' \tag{1.1}$$

where $\triangle x$ and $\triangle R$ are respectively the azimuth and range *resolution cell* dimensions.

The *geometric resolution* depends on the acquisition geometry, the working parameters and the acquisition mode and it is a prime characteristic of an imaging system, so that different systems are in first approximation often compared only by that parameter. In the following the general expressions of the range and azimuth resolutions will be derived for a satellite based SAR, working in strip-map mode.

In order to better understand the measured backscattered field in 1.1,

an ideal system with infinite bandwidth is considered: the two *sinc* functions become dirac pulses. The 1.1 become:

$$u(x,r) = \iint_{\triangle x \triangle R} u(x',r')\, e^{i\phi(x',r')} \delta(x'-x)\, \delta(r'-r)\, dx' dr' = \tag{1.2}$$

$$= |u(x,r)| \cdot e^{j\phi(x,r)} = M(x,r) \cdot e^{j\phi_0} \cdot e^{j\frac{4\pi}{\lambda}r}$$

The amplitude, renamed as $M = |u(\cdot)|$, of the received signal is related to the amount of energy that is backscattered from the scene and depends on the dielectric behaviour of materials as well as on their physical properties. The phase instead is the sum of three distinct contributions:

- the two-ways travel path: sensor-target-sensor;
- the electromagnetic interaction between the incident electromagnetic (e.m.) waves and the scatterers within the ground resolution cell;
- the phase shift induced by the processing system used to focus the image.

In particular, referring to eq. 1.2, the term $\phi_r = \frac{4\pi}{\lambda}r$ is the two-ways travel path, while the term ϕ_0 accounts for the last two contributions. Generally of a single SAR acquisition (*Single Look Complex* - SLC) only the amplitude is of interest, since the phase, as it will be depicted in the following, don't bring information, but if interferometric applications are the aim, the phase plays an important role. The term ϕ_0, that depends only from the acquired scene, is normally supposed to be the same for the two interferometric acquisitions and hence can be neglected. The difference of the ϕ_r terms is related to the two different

travel path associated with the two acquisitions and hence it is used to retrieve information about the topography and/or the displacement affecting the imaged area.

1.2 Geometric resolution

As seen till now, the SAR system is able to identify a point in a bi-dimensional range-azimuth coordinate system. The *range* direction is the one that connects the sensor to the target and it is identified by the radar look-angle. This direction is indicated as *slant-range* to differenciate it from the *ground-range* direction that corresponds to its projection on the ground surface. This second definition is introduced since it provides an handier and more intuitive dimension to describe the imaged targets ground displacement. The *azimuth* direction instead corresponds to the fligth path and is the direction along which the SAR antenna is synthesized.

This kind of 2D vision, also if doesn't allow to separate targets that are at the same distance from the sensor, suits well the problem of a terrestrial surface sensing since the scattering is supposed to come from only one direction: the hypothesis that only a superficial scattering mechanism is present. The image distortions due to the radar acquisition aand its geometry are a crucial issue in SAR imaging but are not the aim of this paragraph.

The *geometric resolution* is defined as the minimum separation (in range or in azimuth) between two points that can be distinguished as separate by the system [14]. The *resolution cell* is then given by the slant-range and azimuth resolutions and it is the smallest dimension that the system can sense. If one considers the ground-range measure in place of the slant-range one, in first approximation and without con-

sidering oversampling processes needed in the image formation step, it can be possible to identify the image's pixel with the resolution cell.

1.2.1 Range resolution

Refering to Fig. 1.1 it is assumed that the radar beam is directed perpendicular to the flight path of the SAR antenna and downwards at the surface of a flat earth, pointing with a look angle θ respect to the *nadir* direction. The antenna's dimensions are indicated with W_a and L_a respectively for the *(y,z)* cross section (*width*) and the *(x,z)* cross section (*length*). In figure Fig. 1.2 is represented the cross section of the acquisition system geometry depicted in Fig. 1.1 in the plane *(y,z)*. This view will allow us to retrieve the slant-range resolution from the acquisition geometry.

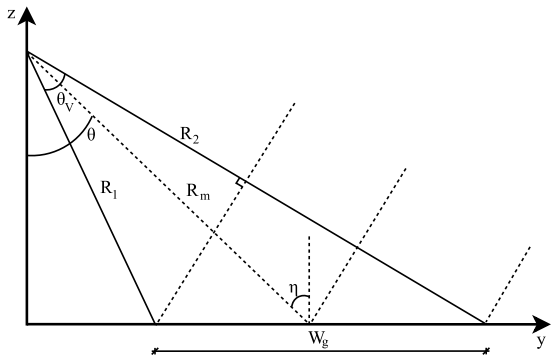

Figure 1.2: Cross section: (y, z) plane

The antenna's beamwidth in the *(y,z)* cross section is indicated as *vertical beamwidth* θ_V, it depends from the antenna's width W_a and the working wavelength λ through the relationship: $\theta_V = \frac{\lambda}{W_a}$. From this parameter depends the coverage area of the radar, also known as *ground swath* and here indicated with W_g. Since in all the real

systems usually $W_a \gg \lambda$ the hypothesis of small angles is reasonable: $\theta_V \ll 1$. Let R_m be the slant-range distance between the radar and the midswath point on the ground, further noticing that η, the angle formed between the midswath ray and the normal to the terrain surface, is the same of the look angle θ, from the system geometry comes that:

$$W_g \cong \frac{\lambda \cdot R_m}{W_a \cos\theta} \tag{1.3}$$

In order to have an idea about the dimension of the involved quantities, the ENVISAT SAR system is taken as a reference. The ENVISAT antenna has the following characteristics:

$$W_a = 1\,m \qquad R_m \simeq 800\,km \qquad \lambda = 5.6\,cm \qquad \theta = 25°$$

Substituting these parameters to the previous formula, it results $W_g \simeq 50\,km$.

For a *continous wave* (CW) radar, i.e. a continous waveform is trasmitted, the two targets would be separated only if they are not illuminated by the same beam, hence W_g is identified with the ground-range resolution leading then to an unreasonable solution. This is the reason of why the SAR uses a transmission of short monochromatic pulses. In this way the resolution is related to the time duration of the pulse and not uniquely to the acquisition geometry. Indeed, let τ be the time extent of the radar pulse, two targets are distinguishable if their echoes are not superimposed, this is quite a less restrictive situation with respect to the continous wave transmission. The minimum separations of two resolvable points, respectively in slant and ground range

are then expressed analitically as:

$$\triangle R_s = \frac{c \cdot \tau}{2} = \frac{c}{2B} \tag{1.4}$$

$$\triangle R_g = \frac{\triangle R_s}{\sin\theta} = \frac{c}{2B \cdot \sin\theta} \tag{1.5}$$

where c is the speed of light and B is the pulse bandwidth: $B \approx 1/\tau$.

The slant-range resolution is then directly proportional to the pulse duration. The smaller is the τ value the better is the resolution, but this behavior should be traded with an energy constraint: the required pulse duration τ may be too short to deliver adequate energy-per-pulse to produce a sufficient echo's *Signal to Noise Ratio* (SNR) for reliable detection. In particular the smaller is the pulse duration and the higher would be the peak value of the trasmitted power, this leads to solutions that are not feasible in practice.

A *pulse compression* technique is normally employed to achieve both high resolution and high SNR. As in traditional radar systems the signal trasmitted by a SAR is a linear *chirp* modulated pulse.

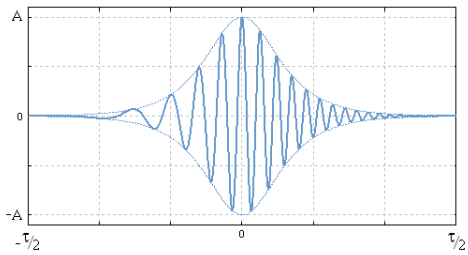

Figure 1.3: Chirp signal

A linear chirp of duration τ is an impulse whose istantaneous fre-

quency varies linearly with time:

$$s(t) = A\cos\left(2\pi\left(f_0 + \alpha t\right)t + \varphi_0\right) rect\left[\frac{t}{\tau}\right] \tag{1.6}$$

The amplitude of $s(t)$ is depicted in Fig. 1.3.

Particularly, the chirp pulse has the following istantaneous frequency:

$$f_{ist} = f_0 + \frac{\alpha}{2\pi}\cdot t \qquad t\epsilon\left[-\frac{\tau}{2};\frac{\tau}{2}\right] \tag{1.7}$$

where f_0 is the frequency at time $t = 0$ and α is the increasing (or decreasing) chirp rate.

Depending from its basic parameter α it is an up-chirp ($\alpha > 1$) in which the frequency increase with time or otherwise a downchirp ($\alpha < 1$).

Thus the chirp bandwidth can be approximeted as:

$$B_c \cong \triangle f = f_{fin} - f_{in} = \left|\frac{\alpha\cdot\tau}{2\pi}\right| \tag{1.8}$$

and the resolution is:

$$\delta R_s = \frac{c}{2B_c} \tag{1.9}$$

The bandwidth of a chirp pulse and its duration are proportional: $\alpha\tau = 2\pi B$. From the relation in 1.4, in order to achieve better resolution, the pulse bandwidth can be increased by increasing its duration.

In this way the trade-off between pulse bandwith and transmitted energy is overtaken. The radar system range resolution is then determined by the type of pulse coding and the way in which the return from each pulse is processed. The slant-range resolution for the ENVISAT system is of $\delta R_s = 20\,m$ and it is achieved with a pulse of bandwidth $B = 160\,MHz$ and $\tau = 2.7 \cdot 10^{-5}$.

1.2.2 Azimuth resolution

The capability of distinguish two adjacent targets in the fligth path direction is called *azimuth resolution*. At the aim of deriving its analitical expression in dependance from the working parameters and the acquisition geometry, the cross section in the (x,z) plane is considered. In practice, given the side-looking configuration, the midswath, the direction connecting in a straigth trajectory the radar sensor with the target, is taken as reference direction in place of the z-axis. This lead to a coordinate system often indicated as *azimuth-range* as shown in Fig. 1.4.

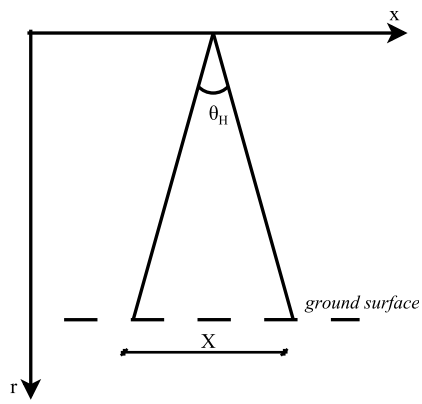

Figure 1.4: Cross section: azimuth-range

As seen for the range resolution, the first quantity that should be

considered in the azimuth resolution formula derivation is the antenna dimension in the considered cross section. The radar antenna in the azimuth dimension was previously indicated with L_a, then the radar beam has an angular spread in that dimension of $\theta_H = \frac{\lambda}{L_a}$, where λ is the wavelenght of the trasmitted signal. The *orizontal beamwidth* θ_H determines the azimuth footprint (X), in fact, considering that usually $L_a \gg \lambda$ and hence $\theta_H \ll 1$ as for the range case, it results that for a given range distance R to the target, the azimuth footprint is:

$$X = R \cdot \theta_H = \frac{R \cdot \lambda}{L_a} \tag{1.10}$$

Two objects at the same range distance R can be distinguished in azimuth only if they are in different radar beams, hence the azimuth resolution can be identified with the azimuth footprint $\Delta_x = X$. A system whose resolution is influenced by the actual antenna dimension is called *Real Aperture Radar* (RAR).

It is worth noting that the azimuth footprint depends from R, hence different resolutions values are obtained for near and far range: R_1 and R_2 in Fig. 1.2 respectively. This resolution, with the ENVISAT antenna length $L_a = 10\,m$ and for $R = R_m$, results: $\Delta_x = 5\,km$.

To improve the along-track resolution at some specified range distance R and wavelenght λ, it is necessary to increase the antenna length in the along-track dimension, but this has strong limits. In fact, apart the problem of placing a big antenna on a flying device, the are mechanical limitation in its construction. Obtaining a surface precision accurate to within a fraction of the wavelength is as more difficult the bigger is the antenna dimension so that a value of $\frac{L_a}{\lambda}$ greater than a few hundred is hard to achieve [14].

For example, for the ENVISAT satellite, azimuth resolution of the

order of $\Delta_x = 10\,m$ had required the use of an antenna of length $L_a = \frac{R\lambda}{\Delta_x} \simeq 4.5\,Km$.

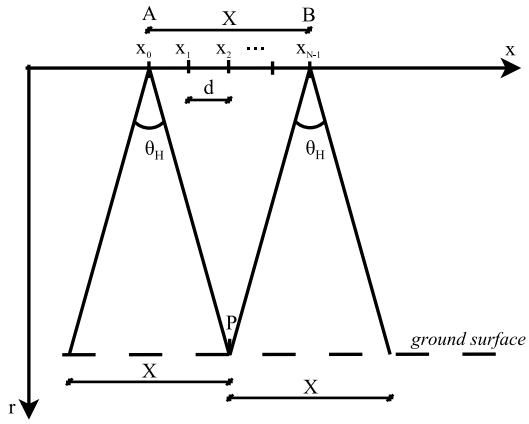

Figure 1.5: Synthetic Aperture principle

The basic principle that leads to the use of SAR sensors relates the possibility of simulating an antenna array with just one small sized antenna moving on a straight trajectory. Refering to Fig. 1.5, let the sensor assume N different positions with a constant step d while moving from A to B, as in the *start-stop approximation*. Then the point P is seen N times from the antenna. This behavior is the same of a N-antennas array, in other words the overall system behaves as a longer antenna of length:

$$L = N \cdot L_a \tag{1.11}$$

The resultant antenna goes under the name of *Synthetic Aperture*.

The N acquisitions of point P are then combined in a process called *beamforming* at the aim of separating the contributions coming from the point P to the one coming from a point P' located at a direction that differs of β from the direction perpendicular to the antenna as

shown in ref_fig.

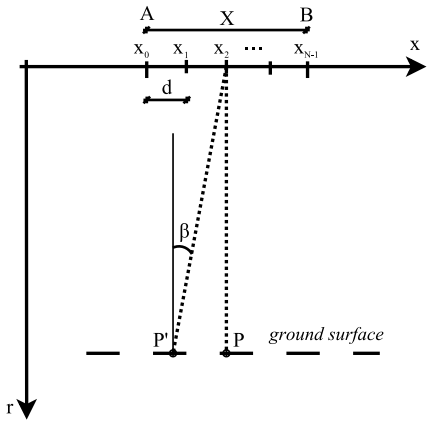

Figure 1.6: Synthetic Aperture principle

The hypothesis of plane and monochromatic waves suffices for deriving the formula of the azimuth resolution. The 2-way gain of the synthetic antenna is obained summing all the contributions from the N transmissions:

$$\frac{|G(\beta)|}{|G(0)|} = \frac{1}{N}\left|\frac{sin\left(\pi\frac{2L}{\lambda}sin\beta\right)}{sin\left(\pi\frac{2}{\lambda}sin\beta\cdot d\right)}\right| \tag{1.12}$$

that under the realistic hypothesis of small angles β, the 1.12 can be approximated as:

$$\frac{|G(\beta)|}{|G(0)|} = \left|sinc\left(\frac{2L}{\lambda}sin\beta\right)\right| \tag{1.13}$$

as for a real aperture but with half wavelength.

Since the antenna is discretized in a finite number of radiative elements, the radiating pattern is periodic of frequency:

$$f_x = \frac{2}{\lambda} sin\beta = \frac{n}{d} \qquad n\epsilon\mathbb{Z} \tag{1.14}$$

In order to avoid the replicas superimposition, the correct sampling frequency, and hence d, should be find. If a sampling frequency greater than the Nyquist limit is considered we obtain:

$$d < \frac{1}{2\,|f_x|} = \frac{\lambda}{4} \tag{1.15}$$

that implies the following lower limit on the pulse repetition frequency:

$$prf > \frac{4}{\lambda} \cdot V \tag{1.16}$$

This last consition cannot be achieved since it wouldn't guarantee a condition of non-ambiguity in the range direction: if trasmitted pulses overlap than range ambiguity arises.

Hence the last condition should be relaxed using directional antennas (so that $\Delta\beta < \frac{\lambda}{L_a}$) that limits the illumination cone only to those contributions coming from the closest angular directions. This works as an anti-alias filter needed because a frequency lower than the Nyquist limit is used. Hence it comes out a new *prf* lower bound that, jointly

with the range *prf* upper bond, become:

$$\frac{2V}{L_a} < prf < \frac{c}{2\delta_R} \tag{1.17}$$

The operative prf should be chosen in the above range.

The directional antenna of length L_a limits the number of times the point P is seen from the radar, and hence the length of the Synthetic Aperture, to:

$$L = R_m \Delta\psi = R_m \frac{\lambda}{L_a} \tag{1.18}$$

Under this condition, the highest *prf* that respects the conditions in 1.17 leads to the best azimuth resolution achievable while having range non-ambiguity:

$$\Delta_x \geq R_m \frac{\lambda}{2L} = R_m \frac{\lambda}{2\frac{\lambda}{L_a}} = \frac{L_a}{2} \tag{1.19}$$

The antenna's actual dimension influences also in this case the azimuth resolution $\delta_x = \frac{L_a}{2}$, but now in the opposite way. The smaller is the antenna size the better is the resolution. It is worth noting that the azimuth resolution for a synthetic aperture radar is independent from R and a constant value for near and far range points. Substituting the ENVISAT antenna length in the last formula it results $\delta_{x_{ENVISAT}} = 4\,m$.

1.3 Single Look Complex statistic

In view of SAR image processing a statistical description for the SAR image, the Single Look Complex (SLC), is provided in the following. In the previous paragraph, the image formation process has been described as well as the system resolution. Having identified a pixel with the resolution cell, it is clear that a pixel value should account for all the scattering mechanisms that happen within the resolution cell.

The possible scattering mechanisms are related to the kind of scattering: superficial scattering, when only an interaction with the surface is supposed, or volumetric scattering, when the wave penetrate the ground and the scattering is seen as a radiating mechanism coming from the interested volume. Scattering mechanism interests the phisical and electromagnetical properties of the target and may be quite vary and complex.

The electromagnetic (EM) wave interacts with the surface in a way that depends from the working wavelength (λ): only objects with size comparable to λ react to the EM illumination. Every scatterer should be known within a small fraction of a wavelength (usually centimeters) in order to describe completely the imaged scene. This requirement never met for natural distributed scenes like rough surfaces. Hence the SAR images are preferably treated as random processes.

Generally the resolution cell has a greater order of magnitude with respect to the wavelength (for example for the ENVISAT system the azimuth-range resolution is $4\times20m$ and a wavelength of $5.6cm$), hence it is realistic to assume that within the resolution cell many elementary scattering mechanisms happen. This is the main assumption that leads to the formulation of a statistical model for the SAR SLC. The monochromatic nature of the SAR implies that all the elementary scattering mechanisms interfere between them in a constructive or

destructive way. The value of the pixel is the coherent sum of these elementary contributions and it is also indicated as *random walk* to refer at the representation of the sum in the complex plane as shown in Fig. 1.7.

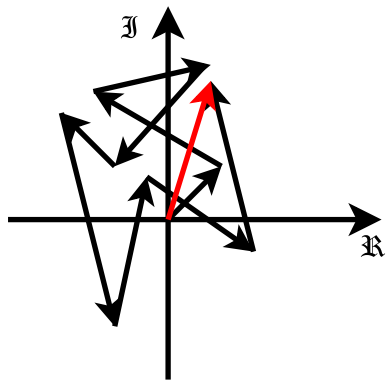

Figure 1.7: Random walk

A pixel value results from the superimposition of several interference phenomena. As a consequence, the pixel can differ in value from the neighboring pixels even for homogeneous areas (phisical property constant in space). This result is evident on the SLC's amplitude as a *salt and pepper* disturb and it is known as *speckle effect* [14, 81]. This phenomena is present in any sensing technique that uses a coherent receiver as, for example, ultrasound, laser optics, etc..

Since the scattering mechanism can be seen as a summation of N discrete contributions, the integrals in 1.1 can be replaced by summations. If we consider also its representation in the complex plane:

$$u\left(x,r\right)=\sum_{n=1}^{N}u\left(x',r'\right)e^{i\phi\left(x',r'\right)}sinc\left(x'-x\right)sinc\left(r'-r\right)dx'dr'=$$

$$=M\left(x,r\right)\cdot e^{j\phi\left(x,r\right)}=\Re\left\{u\right\}+j\Im\left\{u\right\}$$

(1.20)

where $\Re$ and $\Im$ indicate respectively the real and the imaginary part, one can rewrite the expression separately as:

$$u(x,r) = \sum_{n=1}^{N} D_n e^{j\phi_n} \tag{1.21}$$

$$\Re\{u\} = \sum_{n=1}^{N} D_n cos\phi_n \tag{1.22}$$

$$\Im\{u\} = \sum_{n=1}^{N} D_n sin\phi_n \tag{1.23}$$

The statistical description of a SAR SLC is based on the following hypothesis [14, 51]:

- the amplitude and the phase of the elementar scatterers are statistically independent of each other and from the amplitude and phases of all other elementary scatterers;
- the phases of the elementary scatterer can lie with same probability anywhere in the interval $(-\pi, \pi($.

The first assumption is accomplished given that the propagation phase delay is independent from the scattered wave strength. The second, instead, comes directly from the fact that coherent summation of incorrelated scattering mechanism results in random phase values that are uniformely distributed in $(-\pi, \pi($ once folded in that interval. Normally the hypothesis of a large number of elementary scatters in the

resolution cell is made. Under the assumption that the fuctions of $\Re$ and $\Im$ respect the central limit theorem, we know that they are distributed as a Gaussian probability function with zero mean:

$$E\left\{\Re\left\{u\right\}\right\} = \sum_{n=1}^{N} E\left\{D_n cos\phi_n\right\} = \sum_{n=1}^{N} E\left\{D_n\right\} E\left\{cos\phi_n\right\} = 0 \quad (1.24)$$

$$E\left\{\Im\left\{u\right\}\right\} = \sum_{n=1}^{N} E\left\{D_n sin\phi_n\right\} = \sum_{n=1}^{N} E\left\{D_n\right\} E\left\{sin\phi_n\right\} = 0 \quad (1.25)$$

and with variance:

$$E\left\{\Re^2\left\{u\right\}\right\} = \sum_{n=1}^{N} E\left\{D_n^2\right\} E\left\{cos^2\phi_n\right\} = \frac{N}{2} \cdot E\left\{D_n^2\right\} \quad (1.26)$$

$$E\left\{\Im^2\left\{u\right\}\right\} = \sum_{n=1}^{N} E\left\{D_n^2\right\} E\left\{sin^2\phi_n\right\} = \frac{N}{2} \cdot E\left\{D_n^2\right\} \quad (1.27)$$

where E stands for the statistical mean operator. Furthermore one has to notice that real and imaginary part are incorrelated:

$$E\left\{\Re\left\{u\right\}\Im\left\{u\right\}\right\} = \sum_{n=1}^{N}\sum_{m=1}^{N} E\left\{D_n D_m\right\} E\left\{cos\phi_n sin\phi_m\right\} = 0 \quad (1.28)$$

This last result follows from the simmetry of the pdf of the elementary

scatterers. Renaming with x and y the real and imaginary part:

$$p_x(x) = \frac{1}{\sqrt{2\pi\sigma^2}} e^{-\frac{1}{2}\left(\frac{x}{\sigma}\right)^2} \qquad x\epsilon(-\infty,\infty) \tag{1.29}$$

$$p_y(y) = \frac{1}{\sqrt{2\pi\sigma^2}} e^{-\frac{1}{2}\left(\frac{y}{\sigma}\right)^2} \qquad y\epsilon(-\infty,\infty) \tag{1.30}$$

where the σ is the standard deviation computed from formulas 1.26 and 1.27. Both distributions are gaussian with zero-mean and same variance hence the backscattered field u is defined as a *circular complex gaussian* process.

From the last relationship on real and imaginary part it is possible to derive the pdf of amplitude $M = \sqrt{x^2 + y^2}$ while the pdf for the phase is a uniform distribution. The phase and amplitude pdfs are separable.

$$p_M(M) = \frac{M}{\sigma^2} e^{-\frac{M^2}{2\sigma^2}} \qquad M\epsilon[0,\infty) \tag{1.31}$$

$$p_\phi(\phi) = \frac{1}{2\pi} \qquad \phi\epsilon[-\pi,\pi) \tag{1.32}$$

The amplitude is distributed as a Rayleigh while the phase is uniform and hence it doesn't depend on the scatterer, that means that the phase of the SLC doesn't bring any information. The Rayleigh pdf is described by only one parameter: its standard deviation σ. In fact the mean and the variance are respectively given by: $E\{M\} = \sigma\sqrt{\pi/2}$

and $\sigma_M^2 = (2 - (\pi/2))\,\sigma^2$

The intensity is instead distributed as an exponential random variable, defining $I = M^2$:

$$p_I(I) = \frac{1}{2\sigma^2} e^{-\frac{I}{2\sigma^2}} \qquad I\epsilon[0,\infty) \tag{1.33}$$

with equal mean and variance: $E\{I\} = \sigma_I^2 = 2\sigma^2$.

A target that meet the property of N independent scatterers, with no scatterer that remarkably dominates the others is defined *gaussian scatterer* (for the reason we have already seen) or *distributed scatterer* and the model described before holds [14, 109]. For medium resolution (tens of meter) SAR images, this description is met for most of the natural scatterers such as forests, agricultural fields, rough water, soil or rock surfaces. In the literature, the speckle resulting from the imaging of a distributed scatterer is defined as *fully developed speckle* [14, 70, 109]. This condition is violated when one or few scatterers are predominant with respect to the others in the resolution cell as it happen for artificial objects, urban areas or with very-high resolution SAR acquisitions. These last situations refer to the *point scatterer* case in which the pixel value is deterministic and the speckle is defined as *partially developed speckle* [14, 70, 109].

2 SAR Interferometry

2.1 Overview

In the previous chapter the Synthetic Aperture Radar and its peculiarities have been presented. A single SAR image has been described as a plane representation in the azimuth and range directions of the three-dimensional observed scene. When also the height of the imaged scene is of interest, a different application is needed. As for the Stereoscopy, in which two different views are necessary in order to achieve the optical depth information, also in the SAR vision two acquisitions are needed in order to acquire the heigth information. If two SAR images acquired from two slightly different view angles are considered, their phase difference can be usefully exploited to generate Digital Elevation Maps (DEMs) and/or monitor terrain changes (deformation velocity map) [14, 52].

Under the name of *SAR Interferometry* (InSAR) are indicated all the methods that employ at least two complex-valued SAR images, indicated as *interferometric pair*, to derive additional information about the sensed target by exploiting the phase of the SAR signals. Depending on the information that has to be estimated, the two SAR images have to differ at least for one imaging parameter. Which parameter this is, determines the type of the interferometer, e.g. flight path for *across-track interferometry*, acquisition time for *along-track interferometry* (or *differential interferometry* - DInSAR), etc. [3].

Interferometric SARs can be operated from aircraft or satellite. The latter provide data that are at least one order of magnitude cheaper than airborne data and this is particularly true for inaccessible areas of the Earth. Aircraft SAR however ensures high flexibility that is of primary importance in emergency situations, when SAR products are required as quick as possible.

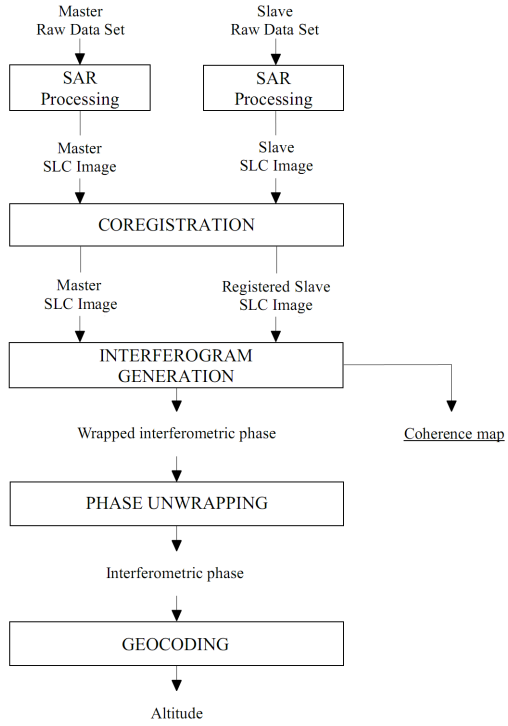

Figure 2.1: SAR interferometry processing chain

Fig. 2.1 shows the InSAR processing chain starting from the two focused SAR images. Since the real scene has been imaged from two different view angles, the position of the scene in the two images is normally different. So, before any other processing the two images

have to be aligned. In the specific, the image taken as reference is defined as *master* and the *slave* is morfologically transformed in order to be aligned to the master. This operation, that goes under the name of *coregistration,* is a crucial step in the SAR processing chain and it can hardly influence the system performances. Multiplying the master SLC by the complex conjugate of the slave SLC, the *complex interferogram* is obtained. In this step, a filtering procedure is normally exploited in order to mitigate the interferometric phase noise. This operation is normally indicated as *complex multilooking* and improve the phase reliability at the cost of spatial resolution impairment. In the next chapters, starting from a statistical description of the interferometric phase, the complex multilooking will be extensively discussed in addition to other interferometric phase estimation methods.

Since the received phase is measured in the interval $(-\pi, \pi($, there exist an ambiguity of the phase to within integer multiples of 2π due to the wrapping of the absolute phase values in the above mentioned interval. The 2π cycle of phase is indicated as *interferometric fringe* and the procedure that allows to obtain the absolute values of ψ from the measured phase is stated as *phase unwrapping.* In order to obtain the absolute height value some ground reference points of known altitude (generally given by mean of *corner reflector*) are needed. Eventually a procedure of *geocoding* is necessary to correctly positioning the measured height values on the earth surface.

2.2 Across-track Interferometry

The Digital Elevation Model generation has been one of the first goal that brought to the development of the SAR interferometry technique. This is accomplished in the so called *across-track interferometry* that

is an InSAR configuration that resembles to a stereo arrangement: two SAR sensors fly on ideally parallel tracks and view the terrain from slightly different directions [52, 87, 90, 119]. Across-track InSAR is a mean to measure the elevation angle θ as a third coordinate, beside azimuth and range, and it allows thus to recover the point's location in space. Fig. 2.2 shows the across-track geometry in the *(y,z)* cross-section.

Depending from the way the two images are acquired, the across-track configuration is indicated as *single-pass interferometry*, when the images are acquired at the same time by means of two radars flying simultaneously, or alternatively *repeat-pass interferometry* if only one radar is used and the scene is imaged in two different satellite passages. In this last case, the time between the two acquisitions, named as *temporal baseline*, strongly affects the quality of the InSAR acquisition. As it will be shown extensively in the following, also the spatial distance between the radars at the time of acquisition, the *spatial baseline*, is even a more important parameter that defines the quality of the interferometer [12, 60].

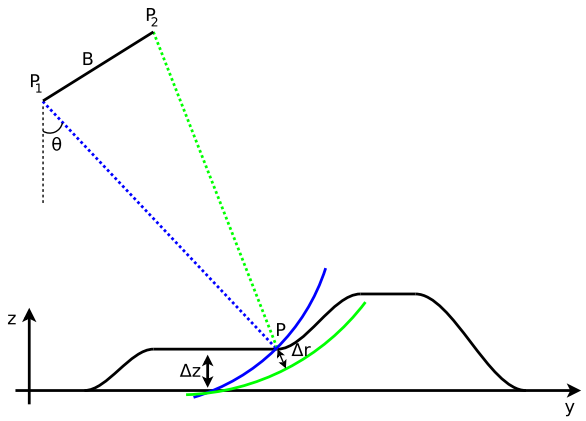

Figure 2.2: Interferometric SAR principle.

As one can see in Fig. 2.2, for a generic point P on the ground surface, the information on the height z is codified in the difference $\triangle r$ of the electromagnetic paths related to the 2 acquisitions.

Let $u_1(\cdot)$, $u_2(\cdot)$ be the two focused SAR images:

$$u_1(x,r) = \int\int \gamma(x',r')\, e^{-j\frac{4\pi}{\lambda}r'} sinc\left[a(x'-x)\right] \cdot \cdot sinc\left[b(r'-r)\right] dx'dr' \tag{2.1}$$

$$u_2(x,r) = \int\int \gamma(x',r')\, e^{-j\frac{4\pi}{\lambda}(r'+\triangle r)} sinc\left[a(x'-x)\right] \cdot \cdot sinc\left[b(r'-r-\triangle r)\right] dx'dr' \tag{2.2}$$

where the pair (x,r) refers to the image coordinate and (x',r') refers to the observed scene coordinate.

Assuming the image $u_1(\cdot)$ as the master SLC, under the hypothesis of perfect coregistration and independency of $\triangle r$ from x and r, the coregistered image $u_2(\cdot)$ is:

$$u_2(x, r+\triangle r) = \rho_c(x,r) \cdot u_1(x,r) \cdot e^{-\frac{4\pi}{\lambda}\triangle r} \tag{2.3}$$

where the quantity ρ_c is a complex quantity, defined as complex coherence, that takes into account the possible decorrelation phenomena between the master and slave SLCs and will be in the following exstensively described.

The *complex interferogram* is then formed by multipling the master

SLC by the complex conjugate of the slave SLC:

$$\Gamma(\cdot) = u_1(\cdot)u_2^*(\cdot) = |u_1(\cdot)||u_2(\cdot)|e^{j\psi(\cdot)} \tag{2.4}$$

with $\psi(\cdot) = \phi_1(\cdot) - \phi_2(\cdot)$ defined as *interferometric phase*:

$$\psi = m \cdot k \cdot \triangle r = m\frac{2\pi}{\lambda}\triangle r \tag{2.5}$$

where k is the wavenumber and m is an integer number that depends from the across-track configuration. In particular $m = 1$ when the path difference depends only from the return path (single-pass configuration), instead $m = 2$ when the path difference accounts for the trasmission plus receiving path (repeat-pass configuration).

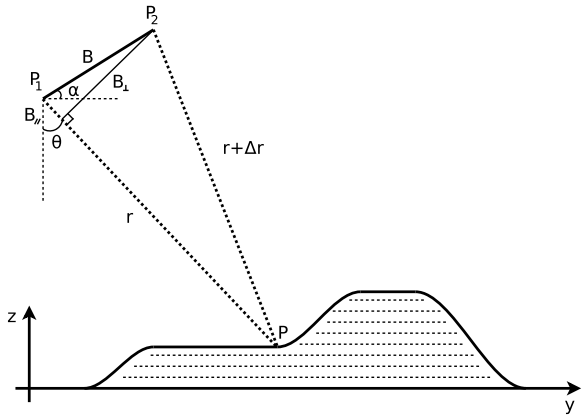

Figure 2.3: InSAR acquisition geometry in the (y,z) plane.

Assuming a repeat-pass configuration and referring to Fig. 2.3, the quantity $\triangle r$ is derived from the system geometry. Considering the

triangle between the points $P_1 - P_2 - P$, the following relation holds:

$$(r + \triangle r)^2 = \left(r - B_{\parallel}\right)^2 + B_{\perp}^2 \tag{2.6}$$

where $B_{\parallel}$ and $B_{\perp}$ are respectively the parallel and the perpendicular baselines, whose expressions are linked to the spatial baseline B as:

$$B_{\parallel} = B \cdot sin\,(\theta - \alpha) \tag{2.7}$$

$$B_{\perp} = B \cdot cos\,(\theta - \alpha) \tag{2.8}$$

Observing that $(B, \triangle r) \ll r$, an approximation for the term $\triangle r$ is derived from eq. 2.6 by neglecting $\triangle r^2$ with respect to r^2 and B with respect to r:

$$\triangle r \cong B \cdot sin\,(\theta - \alpha) \tag{2.9}$$

and consequently, from eq. 2.5, a value for ψ:

$$\psi = \frac{4\pi}{\lambda} \cdot \triangle r \cong \frac{4\pi}{\lambda} \cdot B \cdot sin\,(\theta - \alpha) \tag{2.10}$$

2.2.1 Double differences

The derived phase in eq. 2.10 is the measured phase in one pixel. By itself, this quantity is not useful bacause it still contains the range information and because the phase is wrapped. This means that the measured interferometric phase cannot be taken in an absolute sense, but it should be meant as a differential measurement. In fact, in order to remove the range information in the interferometric phase measurement, the relative phase with respect to a reference point in the image is normally considered. This is the reason of why often this mechanism is described as *double differences*: the first is the one between SLCs in the interferogram generation step at the aim of removing the intrinsic phase of the target: the ϕ_0 contribution in eq. 1.2. The second difference is done between interferometric phases in order to remove the range absolute path dependence.

If the interferometric phase difference between two adjacent pixels P and P' is considered:

$$\triangle\psi = \frac{4\pi}{\lambda} \cdot \triangle\left(\triangle r\right) \tag{2.11}$$

From the geometry in Fig. 2.4, the variation $\triangle\left(\triangle r\right)$ from the point P to P' can be determined. In particular, considering the variation in the look angle $\triangle\theta$, the previous equation can be written as:

$$\triangle\psi = \frac{4\pi}{\lambda}\left[B \cdot sin\left(\theta - \alpha\right) - B \cdot sin\left(\theta + \triangle\theta - \alpha\right)\right] \tag{2.12}$$

Expanding the second term on the basis of the addition formula for the sine function as $sin\left(\theta + \triangle\theta - \alpha\right) = sin\left(\theta - \alpha\right) \cdot cos\left(\triangle\theta\right) + cos\left(\theta - \alpha\right) \cdot$

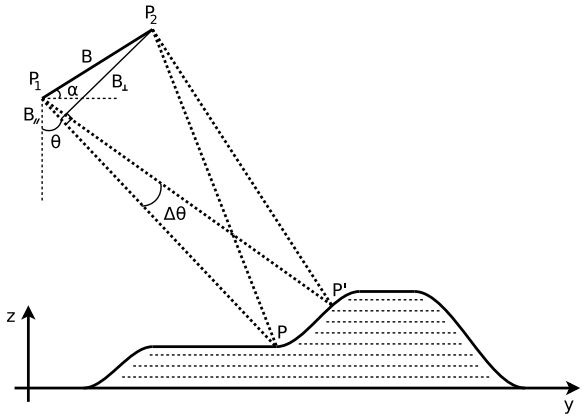

Figure 2.4: InSAR double differences principle.

$sin\,(\triangle\theta)$ and considering the fact that $\triangle\theta \ll 1$ since the two pixels are adjacent, the approximation $sin\,(\triangle\theta) \cong \triangle\theta$ can be done and the last equation become eventually:

$$\triangle\psi = \frac{4\pi}{\lambda}\triangle\theta B \cdot cos\,(\theta - \alpha) = \frac{4\pi}{\lambda}\triangle\theta B_{\perp} \tag{2.13}$$

In order to derive the expression of $\triangle\theta$ from the geometry in Fig. 2.4, it should be noted that it depends from two contributions, one due to the range difference between acquisitions ($\triangle r$) and another one due to the height difference ($\triangle z$). This two contribution can be separated and indicated respectively as *flat-earth* and *topography* contributions:

$$\triangle\psi = \triangle\psi_{flat} + \triangle\psi_{topo} \tag{2.14}$$

For the first contribution, under the usual assumption of $\triangle\theta \ll 1$, it comes that $r \cdot sin\,(\triangle\theta) \cong r \cdot \triangle\theta = \triangle r / tan\,(\theta)$ and the equation 2.13

can be written as:

$$\triangle\psi_{flat} = \frac{4\pi}{\lambda}\frac{B_{\perp}\triangle r}{r \cdot tan\,(\theta)} \tag{2.15}$$

That means that the flat earth generates a linear interferometric phase pattern.

The topography component is derived under the assumption of no range difference but only height difference and from the usual geometry it results $r \cdot sin\,(\triangle\theta) \cong r \cdot \triangle\theta = \triangle z / sin\,(\theta)$, obtaining eventually:

$$\triangle\psi_{topo} = \frac{4\pi}{\lambda}\frac{B_{\perp}\triangle z}{r \cdot sin\,(\theta)} \tag{2.16}$$

This last equation shows the relationship that holds between the height variation and the interferometric phase variation between adjacent pixels. When the aim is to measure the topography (DEM), the flat-earth contribution is removed and a phase-to-height conversion is done. The derived height information is relative to a reference point, as explained above, hence ground-reference points of known altitude are necessary in order to obtain the absolute height measurement of the imaged scene.

2.2.2 System sensitivity and critical baseline

Equation 2.16 states the capability of the system to measure height variations, in other words, the interferometer *sensitivity* to the topography. This parameter can be derived from eq. 2.16 dividing by

$\triangle z$:

$$\frac{\triangle \psi}{\triangle z} = \frac{4\pi}{\lambda} \frac{B_{\perp}}{r \cdot sin\,(\theta)} \tag{2.17}$$

It is evident that the system sensitivity depends mainly from the ortogonal baseline $B_{\perp}$ and from the λ. While the λ is generally fixed depending on the application, the ortogonal baseline is a parameter that can be set in accordance to design constraints as for example in the DEM generation application. In order to improve the system sensitivity, the orthogonal baseline can be increased: the farther the two satellite paths are, the more sensible the system is. At the same time an higher sensitivity means that, for a same slope, the phase wrapping is more frequent (higher fringe density), leading to a more difficult phase unwrapping and height information extraction. This behavior leads to interferometric phase impairment and it is indicated with the name of *baseline decorrelation*. The limit to the maximum orthogonal baseline that causes complete decorrelation is indicated as *critical baseline* and it is defined as the baseline that causes a 2π jump in the interferometric phase for a unitary slant-range variation of the topography. The equation for the critical baseline can be derived from equation 2.15 by setting $\frac{\triangle \psi}{\triangle r} = 2\pi$:

$$\frac{\triangle \psi}{\triangle r} = \frac{4\pi}{\lambda} \frac{B_{\perp}}{r \cdot tan\,(\theta)} = 2\pi \tag{2.18}$$

and eventually:

$$B_{\perp,critic} = \frac{\lambda}{2} r \cdot tan\,(\theta) \tag{2.19}$$

Normally, in the generation of the DEM, the useful baseline value is far away from the critical baseline. By substituting the relative operating parameter, the ENVISAT system has a critical baseline of circa $9\,km$.

2.2.3 Height of ambiguity

If the same reasoning made for deriving the critical baseline is also made starting from equation 2.16, it is possible to derive an important parameter for the interferometric system. So imposing $\triangle\psi = 2\pi$ in equation 2.16 and deriving the height it results:

$$z_{amb} = \frac{\lambda r \cdot sin\,(\theta)}{2B_{\perp}} \tag{2.20}$$

This parameter expresses the height variation that generates a phase change of 2π or, in other words, the height that is encoded in one interferometric fringe and is defined as *height of ambiguity*. This parameter expresses something similar to the system sensibility in eq. 2.17. The more sensitive is the system, the smaller the height of ambiguity is. Generally in DEM generation campaigns the height of ambiguity is a requirement on the final product. In order to achieve the desired minimum requirements often multiple acquisitions are made and only the one that respect all the requirements on SNR and height of ambiguity is chosen for the phase to height conversion and DEM generation.

2.2.4 Spectral shift

Given that the operating orthogonal baseline should be much smaller than the critical baseline value, under this limit there is another degra-

dation due to the diversity of the view angles that can also be accounted as baseline decorrelation. In [44, 88] it has been shown that the spectra of the SAR images acquired from two different view angles are different bands of the ground reflectivity's spectrum. In fact, with reference to Fig. 2.4, supposing that the slope from P to P' is constant and form an angle β with respect to the ground, the ground-range wavenumber is:

$$k_y = \frac{4\pi}{\lambda} sin\,(\theta - \beta) = \frac{4\pi f}{c} sin\,(\theta - \beta) \tag{2.21}$$

By differentiating with respect to θ, the variation in the ground-range wavenumber $\triangle k_y$ related to a variation $\triangle\theta$ in the look-angle is obtained:

$$\triangle k_y = \frac{4\pi f \triangle\theta}{c} cos\,(\theta - \beta) \tag{2.22}$$

A variation in the look-angle causes a shift and a stretch of the imaged terrain spectra. The shift is due to the term $\triangle\theta$ and the presence of f gives a not uniform translation along the frequency (frequency-dependent shift) and than stretches the spectra. This behavior is defined in [44] as the *wavenumber shift* or *spectral shift*. By imposing that the system bandwidth is small with respect to the central frequency f_0, it is possible to ignore the stretch by approximating the previous formula as:

$$\triangle k_y = \frac{4\pi f_0 \triangle\theta}{c} cos\,(\theta - \beta) \tag{2.23}$$

This equation indicates that two SAR surveys acquire two different bandwidth of the ground reflectivity's spectra in dependance from the acquisitions' look-angle. The frequency shift between the two acquired spectra is derived by differentiation of eq. 2.21 with respect to f:

$$\triangle f = -\frac{cB_{\perp}}{r\lambda tan\,(\theta - \beta)} \tag{2.24}$$

Because of the wavenumber shift the two SAR signals are not fully correlated. As seen in the last equation, this decorrelation is higher as larger the orthogonal baseline is and, for this reason, it is accounted as baseline decorrelation. In fact it is worth noting that by imposing $\triangle f$ equal to the system bandwidth, the critical baseline is again obtained. In order to reduce the decorrelation between the two SAR signals a band-pass filtering, that limits the two spectra to the common band, is performed before the interferogram generation. This operation is named *common band filtering* and described in details in [44].

2.3 Differential and along-track Interferometry

As shown in the previous section, one way to perform across-track interferometry is by means of repeated passes from the same radar and image the scene in two different times. If a ground deformation occurs, and this is the case of subsidence phenomena, earthquakes, landslides, etc., there is a further contribution that appears in the interferometric phase expression. In order to detect the correct topography, this quantity should be measured and taken into account. When instead the deformation phenomena is the quantity to measure, on-pourpose systems are designed as in the cases of Differential

interferometry (DInSAR) and along-track interferometry. This *deformation contribution* is independent from the spatial baseline and depends only from the operating wavelength and the projection on the slant-range direction of the occurring deformation (d):

$$\psi_{def} = \frac{4\pi}{\lambda} d \tag{2.25}$$

In along-track interferometry the two SLCs are acquired by means of two antennas aligned with the fligth path or two satellites flying within the same orbit. The absence of a spatial diversity between the points of view make the topographic contribution being null and only the deformation contribution arises. In the general case of no perfect alignment along the orbit it comes again an across-track configuration, the application goes under the name of Differential InSAR and both topographic and deformation contributions are present. This is the most general case since it is difficult to obtain perfectly aligned orbits between acquisitions.

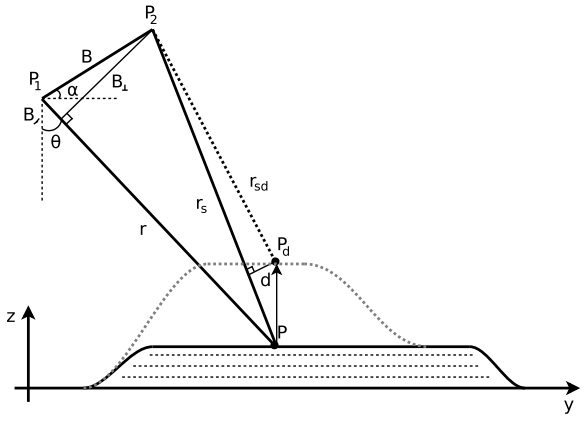

Figure 2.5: DInSAR geometry.

Considering Fig. 2.5 and the movement d along the slant-range direction (from the point P to P_d). Said S_1 and S_2 the two satellites positions, $B_\perp$ the orthogonal spatial baseline, r_s and r_{sd} the slant-range distances of the target positions P and P_d from S_2, the interferometric phase is:

$$\psi = \frac{4\pi}{\lambda} r_{sd} - \frac{4\pi}{\lambda} r \tag{2.26}$$

The previous expression can be rewritten so that the deformation d and topography $\triangle r$ terms are separated:

$$\frac{\lambda\psi}{4\pi} = r_{sd} - r_s + r_s - r = d + \triangle r \tag{2.27}$$

and hence:

$$\psi = \psi_{topo} + \psi_{def} = \frac{4\pi}{\lambda}\triangle r + \frac{4\pi}{\lambda} d \tag{2.28}$$

By removing the flat-earth component, from eq. 2.16 it results:

$$\triangle\psi = \frac{4\pi}{\lambda}\frac{B_\perp \triangle z}{r \cdot sin\,(\theta)} + \frac{4\pi}{\lambda} d \tag{2.29}$$

As previously said, it should be noted that, in constrast with the topographic contribution, the deformation term does not depend from the spatial baseline $B_\perp$. The last equation is important since it shows that a variation of d of half the wavelength can bring a 2π jump in

the measured interferometric phase. This means that the system is much more sensitive to deformations than to the topography. In order to have an idea of the order of magnitude of the detectable deformation, the ENVISAT system parameters (taking a value of orthogonal baseline of 150 m) are substituted and it results:

$$\triangle\psi = \frac{\triangle z}{10} + 225d \tag{2.30}$$

The higher sensitivity to the deformation can be noticed in the difference of the terms that multiply the quantities $\triangle z$ and d . For the ENVISAT system then the sensitivity is 2.8 cm.

The deformation term can be separated from the topographic one in different ways:

1. the pair is acquired with a very small baseline so that the topography contribution is zero as in the along-track interferometry.
2. If an accurate DEM is available, the topography can be estimated and subtracted from the measured phase. The remaining phase will account for the deformation and the unavoidable errors on the DEM.
3. With three SLCs, a DEM can be generated from a pair and used as in point (2).
4. A set of coregistered SLCs is available and a model for topography and deformation velocity can be set at the aim of the estimation of a constant rate of displacement or a singular motion event.

Other contributions to the interferometric phase should be taken into account. In a realistic scenario, the interferometric phase will also

account for the following terms:

$$\psi = \psi_{topo} + \psi_{def} + \psi_{prop} + \psi_{scat} \tag{2.31}$$

where the single terms are:

- ψ_{topo} is the topography contribution;
- ψ_{def} accounts for a possible displacement of the scatterer between observations;
- ψ_{prop} is a possible phase delay difference due to ionospheric and atmospheric propagation conditions: tropospheric water vapour and rain cells are dominant sources for this phase error;
- ψ_{scat} stands for the influence of any change in the scattering behaviour.

Propagation medium effects ψ_{prop} enter the DInSAR measurement directly, it can only be suppressed when a multi-temporal dataset is available and averaging several observations. Instead a phase shift ψ_{scat} due to changes in the scattering properties cannot be distinguished from the deformation term and will affect the estimation.

2.3.1 Multi-pass Differential Interferometry

The advent of new satellite systems with a better control of fligth orbits has made possible the acquisition of set of images related to the same area. This allows to observe a same area over a long time span and model the deformation along the time. Multi-pass DInSAR techniques start from a dataset of N images of the same scene, acquired at different time $t_1, t_2, \ldots, t_N$. A number of M interferograms are

generated, where $M \leq N\,(N-1)\,/2$. Each interferogram has its own temporal and spatial baseline, that are organized in the multitemporal/multibaseline stack (MT/MB). One of the possible strategies aimed for making the choice of M interferograms can try to minimize the temporal and spatial baseline in order to reduce temporal and spatial decorrelation respectively.

Let us approximate the trajectory as straight in the observation time so that the deformation can be expressed as $d\,(t_i, P) = v\,(P)\,(t_i - t_0)$, where $v\,(\cdot)$ is the *velocity of deformation*. Not considering the disturbs on the interferometric phase, only the topographic and deformation contributions remain and the phase of the i-th interferogram related to a pixel P can be expressed as:

$$\psi_i\,(P) = -\frac{4\pi}{\lambda}\frac{B_{\perp i}}{r\,sin\theta}z\,(P) + \frac{4\pi}{\lambda}v\,(P)\,(t_i - t_0) \tag{2.32}$$

For each point P then we have a linear term in the *baseline dimension* and one linear term in the *time dimension*. In order to estimate the topography and the velocity of deformation, a model for the interferometric phase is assumed. Generally this is a bidimensional complex exponential whose frequencies are proportional to topography and deformation:

$$s\,(i, B_n; P) = e^{j\psi(i,B_n;P)} \tag{2.33}$$

The ML estimates of topography and velocity (z, v) is then the maximization of the 2D periodogram in the *baseline-time* domain [29, 32, 36].

As seen in the previous paragraph, the propagation contribution ψ_{prop} cannot be easily removed from a single interferometric acquisition. This contribution, mainly due to atmospheric effects, causes different propagation delays along the image. When a multi-pass dataset is available, the atmospheric disturb can be neglected by incoherently averaging it over the different acquisitions.

PS technique

The first approach that has shown the effectiveness of the use of multiple interferometric surveys for terrain deformation monitoring is the *Permanent Scatterer Interferometry* (PSI) technique proposed in [29, 30]. This approach aims to estimate the pair (z, v) only on specific reliable targets, named *permanent scatterer* (PS), characterized from extremely low temporal and spatial decorrelation. Such a kind of scatterer can be found in mountainous and urban regions as rocks and man-made structures. Choosing targets that do not suffer from baseline decorrelation implies that the processing does not need any pre-estimation of interferometric phase and coherence, allowing in this way a full resolution processing.

In this approach one SLC is chosen as master image and all other interferograms are generated with respect to it. A set of M non-linear equation results by generating $M = N - 1$ interferograms.

While no pre-processing to estimate the phase is not needed, the preliminar and crucial step of PS *selection* should be carefully performed. Since the phase is affected by several disturbs, in order to find the PS only the pixel amplitude is considered over the N available SLCs and the most stable pixels are choosen.

This technique shown for the first time the capability of neglecting the atmospheric disturb, i.e. the $\triangle\phi_{prop}$ term in eq. 2.31, by means

of the Atmospheric Phase Screen (APS) [54, 55]: the phase of the PSs is averaged on a spatial distance smaller than the usual atmosphere spatial correlation (around *500 meters).*

SBAS technique

The *Small BAseline Subset* tecnique extend the single pair Interferometry to stack of multipass acquisitions. In opposition to the PS technique, that provides an estimation on single isolated points, the SBAS technique allows to analyze larger areas defined, by extension of the PS concept, as *distributed scatterers* (DS). Clearly, in this application the spatial and temporal decorrelation has a central role. As the name suggest, only a subset of interferograms is used among all the possible SLCs combinations. In particular considered a set of N images the number of M interferograms respect the following inequality:

$$N - 1 \leq M \leq N \left(\frac{N-1}{2} \right) \tag{2.34}$$

The matching is made by choosing all the interferometric pair that have small spatial and temporal baselines. The matching is generally shown on a space-time baseline graph, where the nodes are the acquisitions and the arcs are the matching between them. An example of matching is provided in Fig. 2.6.

As for classical Interferometry, the SBAS technique needs phase and coherence estimation before using it in the model described in 2.33 and 2.32.

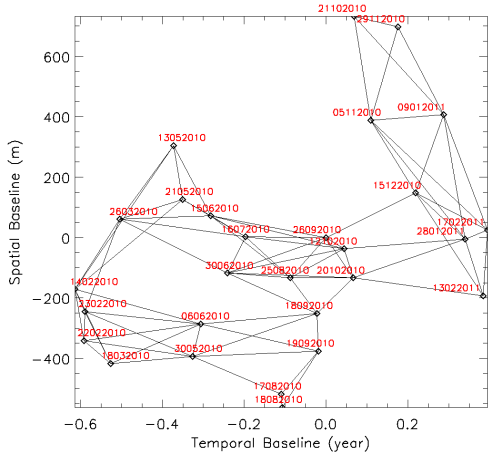

Figure 2.6: SBAS matching example.

2.4 Interferometric phase statistic

2.4.1 Phase difference noise model

The interferometric phase noise ν can be described, as shown in [66], as a additive gaussian noise whos standard deviation depends from the coherence.

$$\psi = \psi_0 + \nu \tag{2.35}$$

Accepting the idealization assumed for distributed scatterer, e.g. Gaussian scattering is introduced as a tractable model, it is possibile to give analytic expression for the probability distributions of interferograms and related entities [3].

The random processes u_1 and u_2 are assumed to be jointly circular

Gaussian. Hence, their joint *pdf* is given by:

$$pdf(\boldsymbol{w}) = \frac{1}{\pi^2 |\boldsymbol{C}|} \exp\left\{-\boldsymbol{w}^H \boldsymbol{C}^{-1} \boldsymbol{w}\right\} \tag{2.36}$$

where

$$\boldsymbol{w} = \begin{pmatrix} u_1 \\ u_2 \end{pmatrix} \tag{2.37}$$

and, introducing $\bar{I} = \sqrt{\bar{I}_1 \bar{I}_2} = \sqrt{E[|u_1|^2] E[|u_2|^2]}$, the covariance matrix is:

$$\boldsymbol{C} = E[\boldsymbol{w}\boldsymbol{w}^{\boldsymbol{H}}] = \begin{pmatrix} \bar{I}_1 & \rho_c \bar{I} \\ \rho_c^* \bar{I} & \bar{I}_2 \end{pmatrix} \tag{2.38}$$

ρ_c is the *complex correlation* between the two SAR images and measures the degree of backscatterer randomness:

$$\rho_c = \rho e^{j\psi_0} = \frac{E[u_1 u_2^*]}{\sqrt{E[|u_1|^2] E[|u_2|^2]}} \tag{2.39}$$

The amplitude of this coefficient ρ, named *coherence*, is a measure of the predictability of the true interferometric signal from its noisy observations, whereas ψ_0 is the expected interferometric phase. The coherence is generally used in any interferometric processing to discriminate between signal and phase noise and determines the grid of

pixels where further processing is carried out. The causes of decorrelation, that implies $\rho < 1$, will be discussed in sec. 2.4.3.

The joint *pdf* of magnitude and phase of an interferogram sample $v = u_1 u_2^*$can be shown to be:

$$\begin{aligned} pdf\left(|v|,\psi\right) &= \tfrac{2|v|}{\pi \bar{I}^2(1-\rho^2)}\cdot \\ \cdot exp\left\{\tfrac{2\rho|v|\cos(\psi-\psi_0)}{\bar{I}(1-\rho^2)}\right\} K_0\left(\tfrac{2|v|}{\bar{I}(1-\rho^2)}\right) \end{aligned} \tag{2.40}$$

where $K_0\left(\cdot\right)$ is the modified Bessel function.

The marginal *pdf* of the interferometric phase can be derived from equation (2.40):

$$\begin{aligned} pdf\left(\psi\right) &= \tfrac{1-\rho^2}{2\pi}\tfrac{1}{1-\rho^2\cos^2(\psi-\psi_0)}\cdot \\ \cdot\left(1+\tfrac{\rho\cos(\psi-\psi_0)\arccos(-\rho\cos(\psi-\psi_0))}{\sqrt{1-\rho^2\cos^2(\psi-\psi_0)}}\right) \end{aligned} \tag{2.41}$$

The phase *pdf* is fully characterized by the two parameters ψ_0 and ρ: ψ_0 is the desired noise-free phase used for topography reconstruction and ρ is a measure of phase noise. If the phase interval is restricted to a width of $\pm\pi$ and centered on ψ_0 the mean and variance of the phase are:

$$E\left[\psi\right] = \psi_0 \tag{2.42}$$

and

$$\sigma_{\psi}^{2} = E\left[(\psi - \psi_0)^2\right] = \frac{\pi^2}{3} - \pi \arcsin(\rho) + \arcsin^2(\rho) - \frac{Li_2(\rho^2)}{2} \quad (2.43)$$

where $Li_2(\cdot)$ is the Euler's dilogarithm.

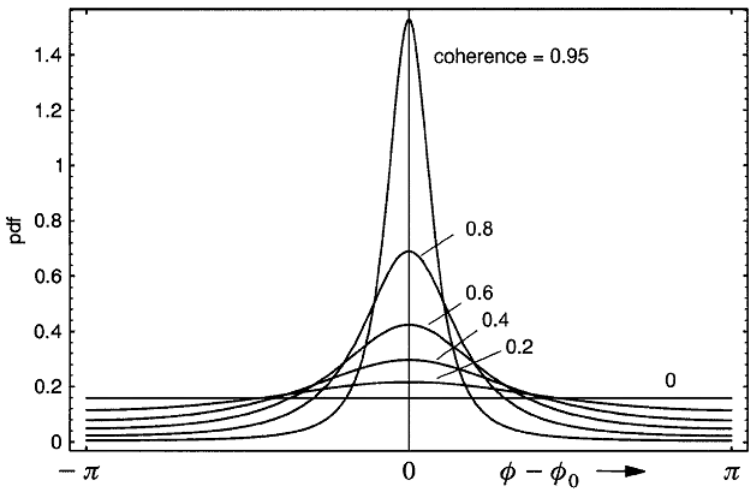

Figure 2.7: Probability density function of the interferometric phase.[3]

Fig. 2.7 shows the shape of the interferometric phase *pdf* in 2.41 for different values of coherence. It's worth underlying three different cases:

- for $\rho = 0$ the phase is uniformly distributed and, hence, carries no information;
- for $0 < \rho < 1$ when the coherence increases the phase distribution becomes more concentrated around its expectation value ψ_0, i.e. the phase noise variance decreases;

- for $\rho = 1$ the phase pdf degenerate into a $\delta - function$.

This behaviour suggest the use of the coherence as a parameter to evaluate the goodness of the phase estimation.

2.4.2 Interferometric phasor noise model

Alternatively, for the interferometric phase noise statistics, the model in the complex domain and defined in [72] can be used. The phasor $e^{j\psi}$ is described by:

$$e^{j\psi} = N_c\, e^{j\psi_0} + (\nu_c + j\nu_s) \tag{2.44}$$

or alternatively in its real and imaginary components:

$$\begin{aligned} real\left\{e^{j\psi}\right\} &= N_c\, cos\psi_0 + \nu_c \\ imag\left\{e^{j\psi}\right\} &= N_c\, sin\psi_0 + \nu_s \end{aligned} \tag{2.45}$$

where ψ_0 is the interferometric phase expected value; N_c is a term proportional to the coherence (ρ) by means of the function in eq. 2.46; ν_c and ν_s in eq. 2.47 are the expression of the noises affecting real and imaginary components respectively

$$N_c = \left|E\left\{e^{j\psi}\right\}\right| = \frac{\pi}{4}\rho\, {}_2F_1\left(\frac{1}{2}, \frac{1}{2}; 2; \rho^2\right) \tag{2.46}$$

${}_2F_1$ is the Gauss's hypergeometric function and E is the expectation

operator

$$\begin{aligned} \nu_c &= \nu'_1 \, cos\psi_0 - \nu'_2 \, sin\psi_0 \\ \nu_s &= \nu'_1 \, sin\psi_0 + \nu'_2 \, cos\psi_0 \end{aligned} \tag{2.47}$$

Both the noise contributions have a ψ_0 dependence, zero mean and variance expressed as follow:

$$\begin{aligned} \sigma^2_{\nu_c} &= \sigma^2_{\nu'_1} cos\left(\psi_0\right)^2 + \sigma^2_{\nu'_2} sin\left(\psi_0\right)^2 \\ \sigma^2_{\nu_s} &= \sigma^2_{\nu'_1} sin\left(\psi_0\right)^2 + \sigma^2_{\nu'_2} cos\left(\psi_0\right)^2 \end{aligned} \tag{2.48}$$

These two values, depending onψ_0 , vary between the extrema given by the values of $\sigma^2_{\nu_c}$ and $\sigma^2_{\nu_s}$ that depend on the coherence and described by empirical curves as in the following equations:

$$\begin{aligned} \sigma^2_{\nu'_1} &= \tfrac{1}{2}\left(1-\rho^2\right)^{0.79} \\ \sigma^2_{\nu'_2} &= \tfrac{1}{2}\left(1-\rho^2\right)^{0.58} \end{aligned} \tag{2.49}$$

2.4.3 Decorrelation causes

The first hypothesis for SAR interferometry is that the two acquisitions are related to the same scene, hence an high level of correlation between the two images is required for the interferometric processing. The causes of decorrelation between interferometric pairs are several and can be classified as:

- termal noise decorrelation: the sensor electronical components as any other electronical elements produce termal noise and that influences randomnly the phase value;
- temporal decorrelation: if the two images belonging to the interferometric pair are acquired with time diversity, the non-invariance of the imaged scene causes decorrelation. The two imaged scenes are different. This can also be owing to weather condition changes. Usually temporal decorrelation is used for object classification considering the coherence of all pixels;
- spatial decorrelation: the spatial diversity in the acquisition of the interferometric pairs causes the scene being imaged from slightly different view angles, introducing a further phase error source;
- non-ideal coregistration decorrelation: as mentioned above the coregistration step is a crucial point of the SAR processing chain, thus coregistration errors cause a lower coherence.

3 InSAR parameter estimation

3.1 Overview

In all interferometric applications, a serious limitation to the phase quality comes from the possible decorrelation phenomena due to either temporal changes and angular diversity. As seen in the previous chapter, the interferometric phase is described statistically and the phase quality is directly related to the degree of correlation between the SLCs by means of the coherence parameter. Interferometric phase and coherence estimation is a crucial step for the InSAR processing since it gives information on the reliable interferogram points and since this estimation often preempts the phase unwrapping (one of the most critical procedure in the InSAR processing chain). A proper phase filtering improves phase reliability and reduces phase unwrapping errors at the cost of an unavoidable spatial resolution loss.

Classically, for InSAR pair filtering, a simple moving average on a rectangular window is used to improve phase reliability. Under the hypothesis of Wide Sense Stationarity (WSS) of all the involved processes, Seymour and Cumming have shown in [95] that the "boxcar filter" is the Maximum Likelihood Estimator for the interferometric phase and coherence. The criticity of this filter is in the WSS hypothesis, in fact, interferometric phase is very likely to have strong variation when the topography or the deformation is strong in the ob-

served region. This effect can bring to misleading phase and coherence estimation leading to inconsistent results.

The first attempts to face the problem of signal non-stationarities in phase estimation came from Lee et al. [67] and Goldstein et al. [49] respectively in the spatial and frequency domains. Both filters make an effort in surpassing the limits of a boxcar averaging and dealing with the fringe morphology. The Lee filter adapts the shape of the estimation window to fringe direction in order to average same phase values, while the Goldstein filter is a frequency filter adapted to the local power spectrum, assuming then that only one frequency component is predominant in the estimation window, this last hypothesis is less restrictive than local stationarity. Furthermore, if we consider the modification at the Goldstein filter in [4], both filters adapt to the signal noise, preserving the signal in case of areas that show high coherence (i.e. low noise level). More recently the spin filters extended the the ML estimation on window whos direction and dimension can adapt locally to fringe density and orientation. Among those filters the most important are the Local Adaptive Filter introduced by Wu et al. [114] in 2006 and the more recent Directional Adaptive Filter introduced by Fu et al. [40] in 2013. A different approach is the one proposed in Lòpez-Martinez et al. [72] in 2002 in which the interferometric phasor noise model is presented and used for low-pass band enhancement of the signal in the wavelet domain. It can be linked to the Goldstein's approach since they both applies in a transformed domain and enhance the signal component that is considered the most significative. In [111] the authors propose to use a region growing technique to build an adapted neighborhood restricted to similar pixels only. Adjacent pixels are aggregated incrementally based on their intensity.

The nonlocal paradigm, born in the context of natural images de-

noising with the NL-means filter [7], aims at averaging only those pixels that share the same statistical properties, enforcing in this way the stationarity hypothesis on the average group. Many nonlocal denoising algorithms have been proposed in the last few years. The Block Matching 3D (BM3D) algorithm [16] deserves a special mention because it blends very effectively the non-local approach with other sophisticated tools (e.g., wavelet transforms, Wiener filtering) to achieve the best performance to date for images affected by additive white gaussian noise (AWGN). The non-local approach, however, makes no assumptions on the noise model, and hence has been readily extended to other types of images and tasks, and in particular to SAR image despeckling. An iterative block-wise version of NLM, the probability patch-based (PPB) algorithm, was first proposed in [19], followed soon by a SAR-oriented version of BM3D [84]. Of course, while the Euclidean distance makes perfect sense to measure block similarity in the additive gaussian noise case, a different measure is needed for speckled SAR images. The problem is solved in [19] where a probability-based similarity measure is developed, adopted in [84] as well. Just like in the AWGN case, non-local techniques look extremely promising for SAR amplitude despeckling, as well as for filtering interferometric, polarimetric, and POL-InSAR data [18]. For this last kind of filters the topography do not impair the estimation as long as a set of similar pixels (statistically homogeneous pixels) is found, assuring this way the validity of the WSS hypothesis among the averaged pixels and the local WSS hypothesis is not a limit anymore.

In multipass applications, given that the previous presented filtering methods can be applied to every pair, the temporal information provides a further clue for improving phase filtering. Different methods have been proposed to improve the selection of these pixels. A suitable modification of the amplitude distance proposed by Lee in [64]

is used in [11] to filter multitemporal data where the adaptive neighborhood is formed by taking into account both spatial and temporal information. Temporal statistics are used to guide the adaptive spatial filter proposed in [79] for SAR polarimetric images. In this case, the selection of the SHPs is based on a likelihood ratio test aimed at deciding whether two sample coherency matrices follow the same Wishart distribution. Only recently, these ideas have been applied to the filtering of multibaseline InSAR data. A first adaptive multilooking (AML) technique is proposed in [28] where, given a suitably long temporal series of images, empirical cumulative distribution functions (ECDFs) are computed for all pixels, and homogeneity with the target is decided based on a two-sample Kolmogorov– Smirnov (KS) test. A more extensive analysis is carried out in [83], where different hypothesis tests, all based on amplitude information, are compared for the selection of the most homogeneous pixels. Among all non-parametric tests considered in [83], Anderson–Darling turned out to be the most powerful, and in fact was soon adopted in [48], in the context of an algorithm proposed for monitoring deformations in non-urban areas. However, even the similarity test itself could be adapted to the local data statistics. Based on this observation, an adaptive procedure is proposed in [56] where data are first classified based on skewness and tail weight of their empirical distribution and then the most suitable statistical test for each class is selected through Monte Carlo simulation. A different strategy is followed in [94] to handle airborne single-pass stacks, which typically comprise a small number (three to five) of multibaseline acquisitions, a case in which statistical goodness-of-fit tests cannot work well. The selection is performed by first carrying out a temporal PCA, to improve reliability, followed by despeckling and thresholding on a sliding search window. The same authors propose a different approach in [92] for large-size stacks, relying on the

similarity of covariance matrices. All the above methods enforce a connectivity constraint, discarding all pixels that, although passing the similarity test, are not connected to the target pixel through a path comprising only SHPs. This is done to reduce the probability of using predictors as pixels not homogeneous with the target. In some cases, as in the polarimetric despeckling technique of [65], such a constraint is not explicitly enforced, but only very close pixels are used as predictors. However, just like connected pixels are not necessarily similar to one another, unconnected ones might well be statistically homogeneous. In regions rich of edges, lines, and point targets, e.g., using a connectivity constraint might reduce drastically the number of SHPs available for filtering [10]. Overcoming the connectivity constraints and, more in general, the reference to spatial closeness, is the goal of nonlocal techniques.

3.2 Maximum-Likelihood Estimation

The ML estimation is generally provided under the hypothesis of local wide sense stationarity (WSS) of the processes u_1, u_2 and $u_1 \cdot u_2^*$ and under the hypothesis of ergodicity in mean. So that the statistical mean operator in eq. 2.39 can be substituted by averages on boxcar widows centered on the current pixel [3, 95, 105, 106]. Let L be the number of independent interferogram samples and following the reasonable assumption that the WSS hypothesis holds locally, a boxcar window of dimensions $\sqrt{L} \times \sqrt{L}$ is generally chosen as average set. The Maximum Likelihood Estimators of the interferometric phase and

coherence are [95]:

$$\hat{\psi}_{ML} = \arg\left\{\sum_{n=1}^{L} u_1[n] \cdot u_2^*[n]\right\} \tag{3.1}$$

$$\hat{\rho}_{ML} = |\hat{\gamma}_{ML}| = \frac{\left|\sum_{n=1}^{L} u_1[n] \cdot u_2^*[n]\right|}{\sqrt{\sum_{n=1}^{L} |u_1[n]|^2 \cdot \sum_{n=1}^{L} |u_2[n]|^2}} \tag{3.2}$$

It has been shown in [3, 66, 95] that by averaging on L samples, the phase noise variance reduces of a factor L. As seen in the previous chapter, the magnitude of the complex coherence is a measure for local interferogram quality, thus its estimation is needed in all interferometric signal processing steps. In Fig. 3.1 the standard deviation of the phase estimate is shown as a function of coherence and the number of independent samples L. It is clear that the higher the coherence and the number of looks are, the lower the phase standard deviation is.

Fig. 3.2 shows the trend of the ML coherence estimation as a function of number of samples L and the underlying *true* coherence. Observing the trend of the coherence with the number of look it is noticed that the coherence estimate is *biased*: it tends to overestimate the low coherence values. From the graph the bias for small L is visible and this gives a further lower bound to the window size. Hence, the window size is traded between denoising power (bigger L) and the range of validity of the WSS hypothesis (smaller L).

In the context of multichannel SAR imagery the authors in [106] show how the coherence estimator, differently from incoherent estimators

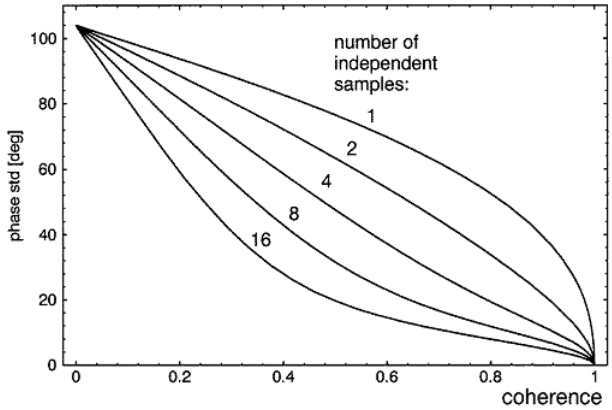

Figure 3.1: Standard deviation of the phase estimate [3].

that exploit only the detected SLC (i.e. no phase value is used), are practically unbiased if the estimation is carried on at least a number of look of 20. It is also shown that this behavior holds in the non-stationary case as long as the WSS condition holds locally: hypothesis of *stationarity for increments*.

When the topography contribution in the estimation window is relevant, the WSS assumption doesn't hold anymore and the estimator performs poorly. As a consequence the fringe pattern is corrupted as impaired is the interferogram resolution. In order to avoid this effect due to the prominent topography contribution, the topography term can be compensated [61, 110]:

$$\hat{\rho}_{ML} = |\hat{\gamma}_{ML}| = \frac{\left|\sum_{n=1}^{L} u_1[n] \cdot u_2^*[n] \cdot e^{-j\psi_{topo}}\right|}{\sqrt{\sum_{n=1}^{L} |u_1[n]|^2 \cdot \sum_{n=1}^{L} |u_2[n]|^2}} \tag{3.3}$$

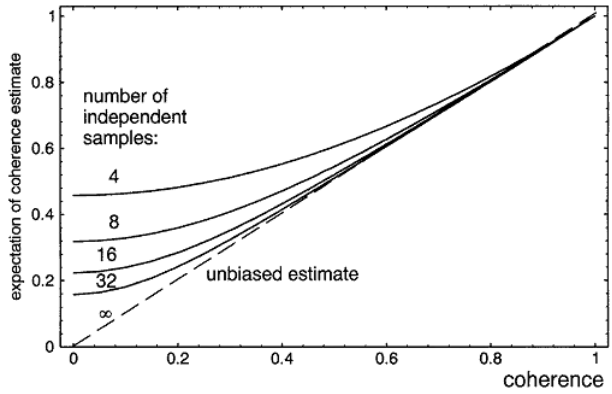

Figure 3.2: Bias of the MLE coherence estimator [3].

Where ψ_{topo} is the topographic contribution (as described in sec. 2.2) that is present in the estimation window, that can be computed from an existing DEM as proposed in [110] or by multiple SAR surveys (Multipass-Multibaseline Interferometry) as proposed in [61], in which one interferometric acquisition can be used as reference for the topography and remove the contribution in the other acquisitions. If no prior information on the topography can be assumed, the ψ_{topo} should be estimated locally with fringe frequency estimation techniques (e.g. MUSIC) [101, 107, 108].

It is worth noting that in the ML estimation of the coherence of eq. 3.3, a corrective term that compensate the estimated ML phase value is already present, so the contingent topographic contribution (non-stationary term) would corrupt the coherence estimation indirectly by means of a corrupted phase estimation. Of course this correction can introduce further noise sources: errors on the DEM or on the local frequency estimation.

3.3 Dealing with non-stationarities

Several methods have been introduced in order to deal with phase non-stationarities while keeping high filter intensity. A first discrimination can be done between methods that apply in the spatial domain and other that apply in the frequency domain.

3.3.1 Filter in the spatial domain

Lee filter

The Lee's filter is a Wiener filter in the spatial domain, in other words it aims to minimize the mean square error of the estimate. Such a kind of filter automatically adapt the intensity of the filtering to the level of noise: high noise areas should be filtered more, while low noise areas less in order to preserve details. This filter also introduced the use of directional windows, in the specific, among the 16 available windows depicted in Fig. 3.3, the one that is alligned to the fringe direction is choosen. Let us consider the statistical model of the interferometric phase in the real domain as described in sec. 2.4, the filter is formulated as:

$$\hat{\psi_x} = \bar{\psi_z} + \frac{\sigma^2_{\psi_z} - \sigma^2_{\nu}}{\sigma^2_{\psi_z}} \left(\psi_z - \bar{\psi_z}\right) \tag{3.4}$$

where the $\bar{\psi_z}$ and $\sigma^2_{\psi_z}$ indicates respectively an estimate and the variance of the noisy phase. The window on which perform the estimate is selected as the one that maximize the coherence, or alternatively that minimize the noisy signal variance.

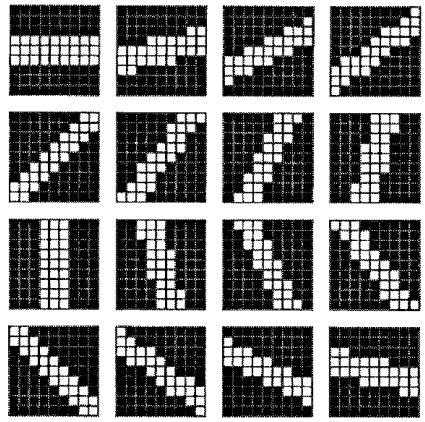

Figure 3.3: Lee's directional windows. [67]

Spin filter

More recent filters are derived from despeckling applications in the laser-optics field and comply with the notion of fringe preservation. These filters, called *spin filters* since they aim to adapt to fringe direction, applies in the spatial domain and extend the Lee's filter by using filtering windows that can vary their size and orientation with continuous values. Among those filters, the most important are named *Local Adaptive Filter* introduced in [114] and the more recent *Directional Adaptive Filter* introduced in [40].

Both filters work in a similar way, for each pixel they compute the fringe density pattern, in order to determine the filter dimension, and the fringe direction. Taking the Local Adaptive Filter as reference the local fringe frequancy is obtained by means of a Discrete Fourier Tranform, the peak of the 2-D transform determines the frequency along the azimuth f_x and range direction f_y. Finally the fringe direction α

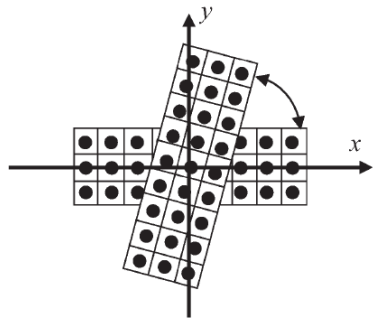

Figure 3.4: Example of Local Adaptive Filter. [114]

is obtained by the formula:

$$\alpha = atan\left(\frac{\hat{f}_y}{\hat{f}_x}\right) \tag{3.5}$$

The filter dimension instead depends on two quantities: the width of the widest fringe in the interferogram w_{max} and the fringe density d_f computed pixel by pixel. In the specific the width w and the length l of the filter is expressed as:

$$\begin{cases} w = NearOdd\,(w_{max} \cdot d_f) \\ l = NearOdd\,(k \cdot w_{max} \cdot d_f) \end{cases} \tag{3.6}$$

where k is a constant that determines the proportion between width and length of the filter and it is found experimentally. The *NearOdd* indicates the approximation to the nearest odd number.

IDAN filter

Instead of using rectangular windows, this approach uses a region growing algorithm to build an adapted neighborhood restricted to similar pixels only. The *Intensity Driven Adaptive Neighborhood* (IDAN) [111] aggregates incrementally adjacent pixels basing the decision on their intensity value. This approach is more flexible with respect to the previous ones and leads to better resolution preservation. The algorithm start from the target pixel as a seed and iteratively test neighboring pixels if they are similar and can be included in the set for the ML estimation. At the end of the process the algorithm obtain a connected set.

3.3.2 Filters in the transformed domain

Goldstein filter

The filter proposed by Goldstein et al. in 1998 [49] relies on the assumption that in a local window the signal is defined in a narrow band with respect to the noise that likely distributes over the whole spectra. This filter compute the Fourier Transform in a local window and shape the filter according to the signal power spectrum. If the estimated spectrum is indicated with $\hat{S}$, the filter is expressed as

$$Z = \hat{S}^{\alpha} \tag{3.7}$$

where α is an attenuation parameter belonging to the interval $[0, 1]$ that regulates the intensity of the filtering: the higher is α the more intense is the filtering.

In [4] Baran et al. proposed to adaptively change the α parameter depending on local noise variance by imposing the following relation:

$$\alpha = 1 - \hat{\rho} \tag{3.8}$$

where $\hat{\rho}$ is an estimation of the local coherence. By this modification the filter increase the filtering intensity in low coherence areas, while avoiding the overfiltering of coherent scatterers.

Several other modification have been proposed during last years. Among the most known there are those that propose to modify the α parameter according to more complex noise measures as in [56, 69], according to an unbiased coherence estimation [57] and according to measures based on Empirical Mode Decomposition [98]. Other methods are based on a iterate use of the Goldstein filter [120] and on the prior identification of an adaptive neighborhood to improve the signal's spectrum estimation [99].

WinP

A different approach in the transformed domain has been proposed in [72] and applies in the wavelet domain. The authors define a statistical model for the interferometric phasor in the complex domain. The filter is rather simple, after the wavelet transformation, the low-pass band is enhanced by multiplying it by a factor 2. In a way this filter can be compared with the Goldstein filter in the sense that both tries to emphisize only one band of the signal where it is supposed to be defined the signal.

3.4 The Non-Local approach

In early digital denoising techniques the estimate $\hat{\boldsymbol{x}}$ of the clean image $\boldsymbol{x}$ is obtained as the convolution ($\otimes$ operator) of the noisy image $\boldsymbol{y} = \boldsymbol{x} + \boldsymbol{n}$ and a suitable filter $\boldsymbol{w}$:

$$\hat{\boldsymbol{x}} = \boldsymbol{y} \otimes \boldsymbol{w} \tag{3.9}$$

Where an additive noise model has been considered, but concepts are readily extended to more complex models.

Introducing spatial variables (we use a single index for the sake of simplicity) the former equation can be rewritten as:

$$\hat{x}(p) = \sum_q w(p,q) y(q) \tag{3.10}$$

The signal estimate in site p is therefore obtained as a weighted sum of observed values $y(q)$ in neighboring sites. Considering that noise has typically a significant high-frequency content, while signal is more concentrated in the low frequencies, denoising filters were usually designed to enact a low-pass action. This is the case, for example, of the well-know Gaussian filter, with (space-invariant) weights:

$$w(p,q) = C \exp(-\lambda \|p-q\|^2) \tag{3.11}$$

where $\|p-q\| = d(p,q)$ is the distance between locations p and q, C is a normalizing constant and λ a decay parameter related with the pass-band. Eq. (3.11) makes clear that the weight associated with

predictor pixel $y(q)$ depends on (decreases with) its spatial distance $d(p, q)$ from the target, with the implicit assumption that pixels close to the target are more similar to it than pixels farther apart, and hence make for better predictors. In other words, the spatial distance is used as a surrogate of the desired tool, a similarity measure which indicates *which* pixels are best suited to predict the target one.

However, the basic assumption "close implies similar", holds only where the signal is indeed smooth (low-pass), and not in the presence of textures or near region boundaries (regions with high pass content) where filters like the Gaussian or even worse the boxcar produce an unacceptable loss of detail. As a matter of fact, much of the intense research activity of the last decades in the image denoising field focused on the development of adaptive *local* filters that ensure a strong noise suppression in smooth regions while preserving important image features. Recently, the attention has shifted on a new and very successful approach: the *nonlocal* filtering [18].

The major conceptual step of non-local filtering has been to recognize the need for an explicit measure of similarity among signal pixels, beyond spatial distance, which help decide which pixels could better predict the target. Although similar ideas are already present in the older *Neighborhood Filters* [116], a first step in this direction is represented by the *Bilateral Filter* [104] where the weights:

$$w(p, q) = f\left\{d(p, q) + d[x(p), x(q)]\right\} \tag{3.12}$$

depend on both the spatial distance and the so-called range distance $d[y(p), y(q)]$, which takes into account the observed values of target and predictor pixels. If the predictor is very different from the target, it is expected to come from a different region, and therefore a small

weight is associated with it. Despite its simplicity, and the fact that noise affects the range distance, the bilateral filter proved very effective, especially in preserving region boundaries, and has been applied with success to filter SAR data, both single-look amplitude [113], and polarimetric [1]. A much better performance, however, is provided by the Non-Local Means (NLM) algorithm [7], which spawned intense research on these methods. The weights of NLM have the same structure as in the Gaussian filter:

$$w(p,q) = C \exp\{-\lambda d[x(p), x(q)]\} \tag{3.13}$$

with the difference that an explicit estimate of signal dissimilarity $d[x(p), x(q)]$ takes the place of the spatial distance. Since the true signal is not available, the dissimilarity is estimated on small blocks $\boldsymbol{y}_p$ and $\boldsymbol{y}_q$ of the observed signal centered on the target and predictor pixels:

$$d[x(p), x(q)] = \|\boldsymbol{y}_p - \boldsymbol{y}_q\|^2 = \sum_{r \in B} [y(p+r) - y(q+r)]^2 \tag{3.14}$$

with B spanning the block. Using blocks rather than individual pixels helps countering the effects of noise on dissimilarity estimation. On the other hand, this amounts to selecting predictors based on their *context* (the surrounding blocks) rather than distance: pixels that have the same context are now expected to be similar. For example, a target pixel located near a region boundary will be estimated mainly from observed pixels that have the same relative position w.r.t. the boundary.

3.4.1 NL-InSAR and NLSAR

The NLInSAR [20] and its extension to polarimetric data NLSAR [21, 22] algorithms are adaptations of the NLM algorithm to cope with problems that are outside the AWGN realm. The Euclidean distance is substituted by a more general and robust similarity distance that depends on the noise distribution model. In both cases the problem is set as a Weighted Maximum Likelihood Estimation (WMLE) where the weights are derived in a data-driven way.

Let be $\Theta = (I, \psi, \rho)$ the vector of intensity, interferometric phase and coherence, $O_q = (A_{1p}, A_{2p}, \psi_p)$ the vector of observations of the two SLCs' amplitude and interferometric phase at site q. The WMLE estimation is defined as:

$$\hat{\Theta}_p^{(MLE)} = \arg\max_{\Theta} \sum_{q \in \Omega} w\,(p,q) \log\, p\,(O_q|\Theta) \tag{3.15}$$

where Ω is an arbitrary neighborhood of the target pixel p. For InSAR data, the maximum likelihood estimator of the covariance matrix is well-known to be the sample estimate of the covariance matrix. By extension of the ML estimate in [95], given the covariance matrix C as in 2.38 the estimator is:

$$\hat{C}_p = \sum_{q \in \Omega} w\,(p,q)\, C_q \tag{3.16}$$

The weights are computed as in 3.13, where the dissimilarity distance is computed through a function inversely proportional to the likelihood that the two compared blocks O_p and O_q are noisy realization of the

same noiseless block $\Theta_p = \Theta_q = \Theta$. By omitting the pedix r that span the block in 3.14, the dissimilarity distance is:

$$d = \sum_B -\log\left(p\left(O_p, O_p|\Theta_p = \Theta_q = \Theta\right)\right) \tag{3.17}$$

where:

$$p\left(O_p, O_p|\Theta_p = \Theta_q\right) = \sqrt{\frac{\mathcal{C}}{\mathcal{B}}}^3 \left(\frac{\mathcal{A}+\mathcal{B}}{\mathcal{A}}\sqrt{\frac{\mathcal{B}}{\mathcal{A}-\mathcal{B}}} - \arcsin\sqrt{\frac{\mathcal{B}}{\mathcal{A}}}\right) \tag{3.18}$$

with

$\mathcal{A} = \left(A_{1p}^2 + A_{2p}^2 + A_{1q}^2 + A_{2q}^2\right)^2$

$\mathcal{B} = 4\left(A_{1p}^2 A_{2p}^2 + A_{1q}^2 A_{2q}^2 + 2A_{1p}A_{2p}A_{1q}A_{2q}\cos\left(\psi_p - \psi_q\right)\right)$

$\mathcal{C} = A_{1p}A_{2p}A_{1q}A_{2q}$

At the iteration i, an estimation of the signal $\hat{\Theta}^{i-1} = \left(\hat{I}, \hat{\psi}, \hat{\rho}\right)$ is available and hence it is used to refine the similarity measure, and the distance become $d = \sum_B -\log\left(p\left(O_p, O_p|\Theta_p = \Theta_q, \hat{\Theta}\right)\right)$, with:

$$p\left(O_p, O_p|\Theta_p = \Theta_q, \hat{\Theta}\right) = p\left(O_p, O_p|\Theta_p = \Theta_q\right) \cdot p\left(\Theta_p = \Theta_q, \hat{\Theta}\right) \tag{3.19}$$

$$\begin{aligned} p\left(\Theta_p = \Theta_q, \hat{\Theta}\right) = \exp\Bigg\{-\frac{1}{T}\frac{4}{\pi}\Bigg[\frac{\hat{I}_p}{\hat{I}_q}\left(\frac{1-\hat{\rho}_p\hat{\rho}_q\cos(\psi_p-\psi_q)}{1-\hat{\rho}_q^2}\right) + \\ + \frac{\hat{I}_q}{\hat{I}_p}\left(\frac{1-\hat{\rho}_p\hat{\rho}_q\cos(\psi_p-\psi_q)}{1-\hat{\rho}_p^2}\right) - 2\Bigg]\Bigg\} \end{aligned} \tag{3.20}$$

where T is a parameter that trades between noise reduction and fidelity of the estimate.

The first term in eq. 3.19 is the likelihood and it corresponds to the data fidelity, while the second term measures the validity of $\Theta_p = \Theta_q$ given the estimate $\hat{\Theta}^{i-1}$. It's worth noting the influence of the previous estimate, in fact $\Theta_p = \Theta_q$ is more likely to hold as the data distributions with parameters $\hat{\Theta}_p^{i-1}$ and $\hat{\Theta}_q^{i-1}$ get closer.

For the NLSAR algorithm, instead, the dissimilarity distance is defined as a function of the Generalized Likelihood ratio $L_G\left(C_p, C_q\right)$ defined as the ratio between the determinants of covariance matrixes:

$$L_G\left(C_p, C_q\right) = \frac{|C_p| \cdot |C_q|}{\left|\frac{1}{2}\left(C_p + C_p\right)\right|^2} \tag{3.21}$$

and as for NLInSAR the dissimilarity distance is:

$$d = \sum_B -\log\left(L_G\left(C_p, C_q\right)\right) \tag{3.22}$$

In order to avoid underfiltering due to rare blocks, both algorithms implement a mechanism to guarantee a minimum number of looks.

4 Non-Local Estimation in Multipass InSAR techniques

4.1 Overview

Advanced DInSAR (A-DInSAR) techniques, by exploiting archives of multipass data spanning long time intervals, are today routinely used to provide topography estimation and monitoring of long-term deformation phenomena affecting the Earth surface. The wide coverage, reliability, and accuracy of those estimations, which particularly reaches the order of the fraction of centimetres/year for deformation measurements, make multipass A-DInSAR a major tool for the monitoring of environmental risk situations, as those associated with natural hazards (f.i., earthquakes, volcanic activities, landslides), as well as human activities (f.i., underground excavations, water, and oil/gas withdrawal). A-DInSAR techniques specialize mainly in two categories based on the assumption about the scattering occurred on the ground. The first one encompasses the class of the persistent scatterers (PS) techniques which assume the scattering to be spatially concentrated and time-invariant over the whole observation period [30]; therefore, not affected neither by spatial nor by temporal decorrelation effects, which are associated with scattering changes in the signal backscattered at the different antennas and at the different acquisition instants, respectively. PS are mainly associated with anthropic or natural corner

reflectors whose dimensions are of the order of the spatial resolution. Therefore, processing is carried out pixel-wise, at the full available spatial resolution. The second category comprises the so-called A-DInSAR stacking techniques, which extend the original, single pair, interferometry toward the joint processing of multiple interferograms. Decorrelation effects are mitigated by generating only a subset of interferograms characterized by small temporal and spatial separations (baselines), as for the Small BAseline Subset approach (SBAS) [5]. To increase signal reliability and reduce the impact of decorrelation effects, these techniques resort to some simple form of spatial filtering, typically plain multilooking. By so doing, they improve the separation of the different components that contribute to the formation of the measured interferometric phase, mainly the deformation and the height of the scatterers imaged in the selected pixel, and the phase delay due to the propagation in atmosphere. Indeed, in the presence of fully developed speckle, the phase difference between homologous pixels of different images, even images with low temporal and spatial baseline, can present significant deviations from the expected value, with detrimental effects on all subsequent processing steps. Needless to say, multilooking reduces the effective resolution of the dataset, but this can be an acceptable loss for many interferometric applications where only low spatial frequencies are of interest, as for distributed deformation and atmospheric phase contribution estimations, and even a significant advantage in terms of computational complexity when wide areas must be processed. However, it also reduces the quality of the extracted information when statistically inhomogeneous pixels are averaged together: this occurs, for instance, at the boundaries of different regions (forests, fields, arid surfaces, anthropic areas, sea, land, and piers). The multilook operation is also relevant for approaches based on pixel-level statistical characterization of the measured sig-

nal. This is the case of SqueeSAR [28], extending the single-look PS interferometry toward the ADInSAR stacking framework, where it is used to handle the impact of target decorrelation in rural areas, or of the recent CAESAR approach [35, 37], where, besides mitigating decorrelation, it helps separating multiple components such as those associated with the layover, already at the interferogram generation stage. All these methods need to estimate the covariance matrix from the data. Therefore, filtering should be carried out without mixing contributes from areas characterized by different backscattering, so as to ensure ergodicity for pixels involved in the estimation.

In the following, the potential of nonlocal filtering for SAR interferometric stacks are shown, in the framework of SBAS processing. The conventional multilooking step, used normally to improve the coherence estimation, is removed in favour of an Adaptive Multi-Looking algorithm (AML), based on the nonlocal approach. Several pixel homogeneity measures are considered, all of them based on amplitude data, both with and without data prefiltering. Although the phase is neglected, primarily for computational complexity reasons, the amplitude information has been shown [6] to allow by itself a reliable classification of different areas within a SAR image, and to be a good indicator of different scattering phenomena [83]. The resulting techniques are tested first on synthetic data, and then on both low-resolution (ENVISAT) and high-resolution (COSMO-SkyMed) real data, in order to assess their performance comparatively, and to demonstrate their capability to improve the quality of InSAR measurements w.r.t. the reference scheme.

4.2 AML in Multipass InSAR

Let be $\boldsymbol{U}$ a stack of N SAR images of the same scene, defined on a rectangular spatial grid $\Gamma \subset Z^2$, and perfectly coregistered. Therefore, the stack can be alternatively regarded as a collection of N images $\boldsymbol{U} = \boldsymbol{u}_1, ..., \boldsymbol{u}_N$ defined on Γ, or a collection of $|\Gamma|$ vectors $\boldsymbol{u} = \boldsymbol{u}(p)$, $p\epsilon\Gamma$, each of length N, with the elementary complex observable denoted by $u_i(p)$. By removing all indexes and subscripts when non-ambiguous, the generic observed value u is related to the underlying true signal $\tilde{u}$ by the relation:

$$u = \tilde{u}\, n \tag{4.1}$$

with n the speckle, assumed here to be fully developed, hence circular Gaussian with zero mean and unit variance, and spatially white. In general, the true value corresponding to the observed quantity x is indicated with $\tilde{x}$ and its estimate with $\hat{x}$, so, e.g., expressing the former quantities in terms of amplitude a and phase θ, it results:

$$u = ae^{j\theta} \quad and \quad \tilde{u} = \tilde{a}e^{j\tilde{\theta}} \tag{4.2}$$

Then, by definition, the interferogram obtained from the ith and jth images of the stack is:

$$\boldsymbol{\Gamma}_{ij} = \boldsymbol{u}_i \odot \boldsymbol{u}_j^* \tag{4.3}$$

where $\odot$ indicates pixel-wise product and $*$ conjugation. For $i = j$,

this gives the reflectivity of the generic image $\boldsymbol{R}_i = \boldsymbol{u}_i \odot \boldsymbol{u}_i^*$, while the nonredundant cross-products give rise to $N(N-1)/2$ interferograms. As seen in sec. 2.4, the complex correlation coefficient between two SAR images expresses their degree of similarity and hence measures the backscatterer randomness. Adapting the notation in 2.39 at the multipass model, for a generic pixel and a generic pair (i, j) the complex correlation is given by:

$$\rho_{c_{i,j}} = \frac{E[u_i u_j^*]}{\sqrt{E[|u_i|^2]E[|u_j|^2]}} \tag{4.4}$$

where $E[\cdot]$ is the statistical expectation operator. The coherence is high when the scattering phase centers are similar in the two acquisitions; therefore, it is sensitive to scene changes, caused either by the imaging angular diversity or by temporal variations of the signal as those typically observed in the vegetated areas.

In the following, it is assumed to organize all the interferograms, or a subset of them, in a single stack of length $M \leq N(N-1)/2$, and the double subscript that refers to the interferometric pair is substituted by the number that express the position of the interferogram in the stack: $\boldsymbol{\Gamma}_m$, $m\epsilon\,[0, M-1]$. The goal is to obtain a good estimate of the complete interferometric stack based on the observable data:

$$\hat{\boldsymbol{\Gamma}} = g(\boldsymbol{U}) \tag{4.5}$$

By this very general statement, it is meant that, in principle, the estimate of a generic interferometric datum $\boldsymbol{\Gamma}_m(p)$ depends on the whole stack of observables u, because of the complex dependencies existing

among the component images and among the vectors associated with different spatial locations. Taking into account and properly modeling all such dependencies, however, is out of the question, and even if possible, the computational complexity associated with the resulting algorithm would be unbearable. Therefore, with reference to the SBAS framework, the processing will resort to the much simplified scheme outlined in the block diagram of Fig. 4.1.

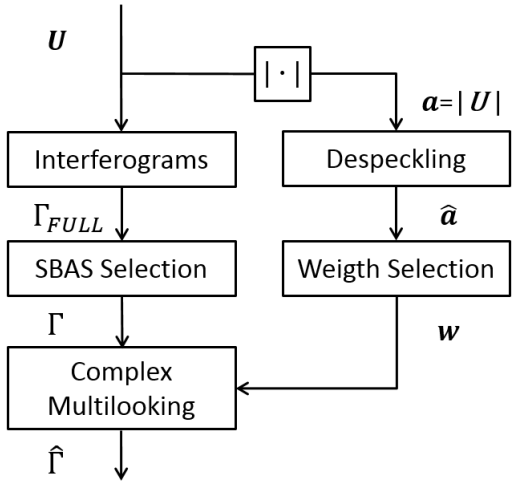

Figure 4.1: General block diagram for nonlocal filtering of interferometric stacks.

Among the full set of $N(N-1)/2$ interferograms $\mathbf{\Gamma}_{FULL}$, the stack $\mathbf{\Gamma}$ composed by the interferometric pairsets characterized by small (spatial and temporal) baselines is selected. This practice, in line with the SBAS processing philosophy, is driven by the need to limit both the decorrelation and the residual topography contributions over large spatial baselines, which could impair the performance of subsequent processing steps, especially phase unwrapping. Then, for each pixel p, the vector $\mathbf{\Gamma}(p)$ is estimated by means of a weighted average of

vectors belonging to its neighborhood $\Omega(p)$:

$$\hat{\mathbf{\Gamma}}(p) = \hat{\boldsymbol{I}}(p) \odot \hat{\mathbf{\Gamma}}_{\psi}(p) = \sum_{q \epsilon \Omega(p)} w(p,q)\, \mathbf{\Gamma}(q) \tag{4.6}$$

where $\hat{\boldsymbol{I}}(p)$ denotes the vector of amplitudes and $\hat{\mathbf{\Gamma}}_{\psi}(p) = e^{j\psi(p)}$ is associated with the interferometric phases $\psi(p)$. In principle, $\Omega(p)$ should span the whole image; however, to limit complexity, we will use relatively small neighborhoods of each point, with the tradeoff between complexity and performance established experimentally. Of course, the core of the proposed approach resides in the computation of the adaptive weights $w(p,q)$ which, following the nonlocal approach, depend on the similarity of the signal observed in points p and q. In nonlocal SAR despeckling, similarity is computed on small blocks surrounding the pixels of interest, exploiting the spatial context to improve reliability. With interferometric stacks, however, using spatial blocks would much increase complexity. Therefore, considering also the large amount of temporal information available to base decisions upon, we compute filtering weights based only on the vectors $a(p)$ and $a(q)$. Nonetheless, we take advantage of the spatial dependencies by means of a preliminary despeckling step carried out independently on each observation $\boldsymbol{u}_i$. Despeckling increases the reliability of similarity estimation although, possibly, at the cost of some loss in spatial resolution. Of course, working separately in the spatial and temporal domains is suboptimal but necessary to cope with complexity constraints. A final simplification consists in basing our weight computation exclusively on amplitude (or intensity) information, thus neglecting the phase. Again, this is a suboptimal choice, dictated by simplicity reasons, but phase information is really signifi-

cant only in high-coherence regions, which need no enhancement (f.i., permanent scatterers). Moreover, even in this case, the phase signal could be characterized by a high variability (in the spatial/temporal baseline domain) from one acquisition to the other. Instead, we focus on low-coherence regions, where an intensity-driven approach is certainly reasonable, and frequently adopted, e.g., [111] and [28], with good results.

This general scheme can be specialized in a number of different algorithms by specifying the major processing steps and free parameters, in particular, the despeckling technique, the filtering procedure, and the weight computation, the latter involving the definition of a suitable similarity measure.

4.2.1 Prior despeckling

The despeckling is used in this work as a black box tool, with no effort to tailor the selected techniques to specific requirements of subsequent steps. The few alternatives considered are listed and commented below. For the sake of simplicity, in the following, the amplitudes $a(\cdot)$ are indicated with the same symbol whether they have undergone a preliminary despeckling process or not.

1. No filtering: necessary as a reference to evaluate the benefits, if any, provided by spatial despeckling.
2. Boxcar multilooking (BML): the simplest form of speckle suppression, still widespread among practitioners, causes a fully predictable loss of spatial resolution.
3. SAR-BM3D: a nonlocal despeckling filter [84] freely available on the web. A deeper analysis of these and other filters is out of the scope of this work; the reader is referred to [18] for a review of

techniques. The effectiveness of the considered filters is evaluated indirectly, through their effects on the final interferometric products obtained at the end of the processing chain.

4.2.2 Interferogram Filtering

Boxcar Multilooking

BML is used originally in SBAS [5], and hence is a necessary reference and the starting point of the experimetal path. BML uses only the limited number of predictors that fall in a small rectangular box surrounding the target p, and all predictors are assigned equal weight $w(p,q) = 1/S$, with S the box size. It is justified by assuming that the pixels closest to the target (according to a weighted L^∞ norm) are those more likely to have the same underlying signal, and hence its best estimators. This is certainly false in heterogeneous areas, like at regions boundaries, and hence this local filter is bound to cause a severe loss of detail.

Adaptive Multilooking

AML works just like BML, but chooses the predictor pixels as those most similar to the target pixel according to some suitable similarity measures, discussed in the next section. In homogeneous areas of the image, the selected predictors might well happen to be the spatially closest pixels, falling back to BML, while in the presence of region boundaries it is expected that the selected predictors belong to the same region of the target, irrespective of their spatial distance, thus ensuring the preservation of image structures. It is worth underlining that AML, though following the nonlocal principle, keeps the major structural constraints of BML, i.e., a fixed number S of predictors

with equal weights. This allows us to compare BML and AML on equal basis, and to assess the improvements granted by the nonlocal approach and by the various similarity measures. On the other hand, this is an explicit requirement of the SBAS processing chain which, to limit complexity in the analysis of large areas, works on a subsampled grid of points, assumed to be all equally reliable.

Nonlocal Means

In NLM [7], all pixels in the analysis window Ω are used as predictors, with weights that depend on the distance between the signal observed in the target site $\boldsymbol{a}(p)$ and predictor sites $\boldsymbol{a}(q)$, according to:

$$w\left(p,q\right) = C\, e^{-\lambda d[\boldsymbol{a}(p),\boldsymbol{a}(q)]} \tag{4.7}$$

with λ a decay parameter which trades off smoothing for detail preservation. With NLM, however, depending on local signal statistics, it can happen that only a few weights are significantly different from 0. In such cases, the estimate of the coherence would be dramatically up-biased, which is not acceptable for the use in the subsequent processing. Therefore, this solution is not considered in our SBAS-oriented experimental analysis.

4.2.3 Distance Measures

Adaptive Multilook methods rely on some suitable estimate of dissimilarity between target and predictor pixels, based on the vectors of observed amplitudes $\boldsymbol{a}(p)$ and $\boldsymbol{a}(q)$, and possibly on the pixel locations p and q.

Spatial Distance

First of all, for generality the spatial distance between the pixels is included; in particular, a weighted L^K-norm is considered:

$$d_{LK}(p,q) = \left[\left| \frac{p_{rg} - q_{rg}}{w_{rg}} \right|^K + \left| \frac{p_{az} - q_{az}}{w_{az}} \right|^K \right]^{1/K} \tag{4.8}$$

where couples (p_{rg}, p_{az}) and (q_{rg}, q_{az}) are range and azimuth coordinates, while w_{rg} and w_{az} are weights set to account for the different resolutions in range and azimuth. Needless to say, using a spatial distance to select predictors amounts to resorting to ordinary local filtering. In particular, using an L^∞ norm and proper weights, we can include in this analysis the BML originally used in SBAS.

KS Distance

Let X be a random variable, and x a vector of N-independent observations of X. By sorting x in ascending order, it is obtained a new vector $x' : x'_1 \leq x'_2 \leq \cdots \leq x'_N$, which allows to compute the ECDF:

$$\hat{F}_{\boldsymbol{x}}(x) = \begin{cases} 0 & x < x'_1 \\ n/N & x'_n \leq x \leq x'_{n+1} \\ 1 & x \geq x'_N \end{cases}, \quad 0 < n < N \tag{4.9}$$

which is an unbiased estimate of the true CDF $F_X(x) = Pr(X \leq x)$. The distance between the ECDFs associated with two samples x and y is used as reasonable measure of their statistical homogeneity. This is done with the KS distance, defined as:

$$d_{KS}(\boldsymbol{x}, \boldsymbol{y}) = \max_x \left| \hat{F}_{\boldsymbol{x}}(x) - \hat{F}_{\boldsymbol{y}}(x) \right| \tag{4.10}$$

which, in fact, is used in the two-sample KS test to decide, with a given level of significance, whether two samples follow the same probability distribution [100]. The KS distance was already used in [28] (together with other criteria) to decide about the statistical homogeneity of pixels involved in coherence matrix estimation. The KS distance is sensitive to differences in both the mean and variance of the observed vectors and, given relatively large samples, provides a reliable indicator of inhomogeneity. However, it relies on the hypothesis that each sample is drawn from a single random variable, i.e., with reference to DInSAR stacks, the true amplitude of a pixel does not change in time. This might be a too strict requirement, especially in low coherence (e.g., vegetated) areas, considering seasonal changes and the temporal lags typical of DInSAR stacks.

PB Distance

Measures of patch similarity, which are the core of nonlocal methods, have been studied in rigorous probabilistic terms in several recent papers, [17, 19, 75, 103]. Let us assume that the observed data vector x is related to the unknown clean signal $\tilde{\boldsymbol{x}}$ and noise n through some known function $x = f(x, n)$ which can be specialized to the case of additive noise, multiplicative noise, or others. Then, in [19], a PB distance is defined between two observed vectors $x = f(x, n)$ and $y = f(y, n)$ as:

$$d_{PB}\left(\boldsymbol{x}, \boldsymbol{y}\right) = -p\left(\boldsymbol{x}, \boldsymbol{y} | \tilde{\boldsymbol{x}} = \tilde{\boldsymbol{y}}\right) \tag{4.11}$$

(p is used for probability density function, here) which implies that $\boldsymbol{x}$ and $\boldsymbol{y}$ are considered to be "close" if they are highly likely to be observed when the underlying signals $\tilde{\boldsymbol{x}}$ and $\tilde{\boldsymbol{y}}$ are equal. Then, given the model that relates observed and clean data, and the statistics of sig-

nal and noise, one can obtain an explicit form for the above distance. In particular, this distance has been used for SAR despeckling in [19] and [84] with fully satisfactory results. In such papers, the observed data were the amplitudes of N-pixel image patches, a multiplicative noise model was considered, with fully developed L-look white speckle noise, and a uniform prior was chosen for the clean signal. Under these assumptions, the distance takes the explicit form:

$$d_{PSM}\left(\boldsymbol{x},\boldsymbol{y}\right)=\sum_{i=1}^{N}\log\left[\frac{x_i}{y_i}+\frac{y_i}{x_i}\right] \tag{4.12}$$

Here, the same path is followed, and obtain the same formula, except for the fact that all data vectors are associated with single-pixel multitemporal vectors (N images), i.e., with reference to a couple of pixels p and q, $x=a(p)$ and $y=a(q)$. Note that, unlike for the KS distance, this measure compares values observed in the same time instant (same image); hence, it is able to take into account time changes.

4.3 Experiments on simulated data

Preliminary experiments on simulated interferometric stacks are carried out in order to study, in a controlled situation, the performance of the alternative filtering work-flows in various situations of interest. To this end, a small (for computational efficiency) data stack comprising of $N=16$ images of size 128×128 pixel is simulated. Of course, in the interior of homogeneous regions, filtering is not really a problem, and the plain multilooking used originally in SBAS is fully satisfactory. Problems arise, instead, in the presence of region boundaries and thin structures. Therefore, in the experiment, the simplest possible geometry of interest is considered: a thin (five pixels in the

experiments) homogeneous F region over a homogeneous background B, as depicted in Fig. 4.2.

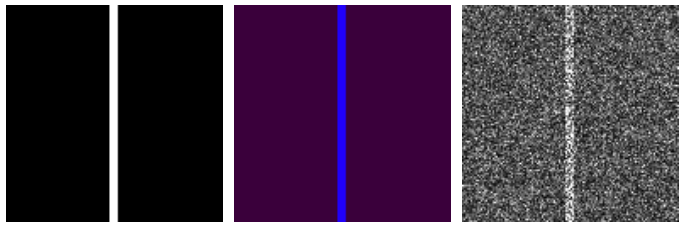

Figure 4.2: Geometry of the simulated scene, 128 × 128 pixels, true coherence map (same colorbar as Fig. 4.4), and sample amplitude image, with AF /AB=2.

With the same rationale, both regions are assumed to have low coherence, $\rho_B = 0.05$ for the background, and $\rho_F = 0.20$ for the foreground, since high-coherence data need no improvement. As for the amplitude, we assume it to be constant, both in space and time, in the background, $a_n(p) = A_B \ \forall p \in B$, $n = 1, ..., N$. For the thin foreground region, instead, the space invariance is still valid, but two cases are distinguished, i.e., $\forall p \in F$, $n = 1, ..., N$

1. $a_{F,n}(p) = A_F$, constant in space and time;
2. $a_{F,n}(p) = A_B[1+\Delta_F cos(2\pi n/N)]$, constant in space but variable over the time.

The second case accounts for situations in which the two regions have different amplitude history in time, due, e.g., to seasonal changes, and we consider the most challenging situation in which the average amplitude is the same. For each pixel, data have been modeled as complex circular Gaussian random variables with correlation matrix dictated by the coherence ρ_B and ρ_F. In these experiments, deterministic information associated with DEM and deformation, which contribute to the interferometric phase, have not been considered since distance

measures of interest works only on amplitude data. System parameters (wavelength $5.6cm$, look angle 23°, range distance $860\,km$) have been set according to the real dataset of ENVISAT images used in the next section. The pixels are assumed to be squared; therefore, BML operates with a square window, chosen of size 9×9 to remain close to the size that will be used in experiments on real SAR stacks. The search window for AML, centered in the current pixel, is set to be twice as large as the boxcar window, which guarantees the availability of a sufficient number of similar pixels with a limited computational load. For all pixels of the search window, the similarity with the current target is estimated, based on one of the distance measures in sec. 4.2.3, and the S pixels with the lower distance are selected for averaging. Therefore, for the simulated experiments, the dimension of the search area is set to 19×19 pixels and 81 pixels, out of the 361 available, are selected for filtering. The foreground region is five-pixel wide, large enough to guarantee that in the search area there are more than 81 pixels of the same type as the target (background or foreground) to select homogeneous predictors.

Six AML variants are compared, combining KS and PB distance measures with three choices for prefiltering, i.e., 3×3 boxcar, SAR-BM3D, and no prefiltering at all. In Tab. 4.1, with reference to the first case (no amplitude history), we show results on the accuracy of predictor selection as a function of the amplitude contrast A_F/A_B. More precisely, for each foreground pixel (upper part of the table), the fraction of wrong predictors si computed (hence, drawn from the background); then, it is averaged over all foreground pixels and over ten repetitions of the experiments to obtain the overall probability of error $P_E(F)$. In the best case, corresponding to perfect selection, $P_E(F)$ is obviously 0, while in the worst case, corresponding to a random selection of predictors in the search area,$P_E(F) \simeq 0.74$. This is done in a sim-

		no filtering		3×3 boxcar		SAR-BM3D	
F/B	A_F/A_B	KS	PB	KS	PB	KS	PB
F	4	0 (0)	0 (0)	40 (4)	17 (2)	0 (0)	0 (0)
	2	19 (3)	201 (13)	62 (3)	58 (4)	0 (0)	0 (0)
	$\sqrt{2}$	237 (9)	579 (14)	96 (7)	137 (11)	24 (4)	77 (9)
B	4	0 (0)	0 (0)	95 (1)	97 (1)	0 (0)	0 (0)
	2	1 (0)	5 (1)	52 (1)	49 (1)	0 (0)	0 (0)
	$\sqrt{2}$	47 (4)	111 (6)	38 (2)	36 (2)	22 (2)	1 (1)

Table 4.1: Probability of selection error (×1000) in the absence of amplitude history. In parentheses, the st.dev. (×1000).

ilar way for the background (lower part of the table), with the only difference that to compute $P_E(B)$ only data on a strip surrounding the foreground are averaged: five pixels on each side, where errors can actually occur. In all cases, the standard deviation observed over the ten repetitions of the experiment, reported in parentheses in the table, is very low, suggesting a good reliability of the estimates.

When the contrast is relatively large, $A_F = 4A_B$, the probability of error is close to 0, as expected, except for the case of boxcar prefiltering. In this case, in fact, boundary pixels after filtering have mixed statistics, and wrong selections become very easy. Note that this problem is not observed with SAR-BM3D prefiltering, since it avoids smoothing region boundaries, nor in the absence of filtering, of course. Performance impairs gradually for all tested combinations when contrast decreases, with P_E approaching the worst-case value when $A_F = \sqrt{2}A_B$ and no prefiltering is used. At low contrasts, some prefiltering is

clearly beneficial, with the more sophisticated SAR-BM3D keeping a lead over boxcar filtering. As for the similarity measures, KS works consistently better than PB. This can be easily explained by considering that, by sorting the values collected in all bands, it ends up using ordered statistics, with a further filtering effects which generalizes the operation of median filtering. To appreciate visually the effectiveness of KS-based and PB-based predictor selections, as well as the impact of prefiltering.

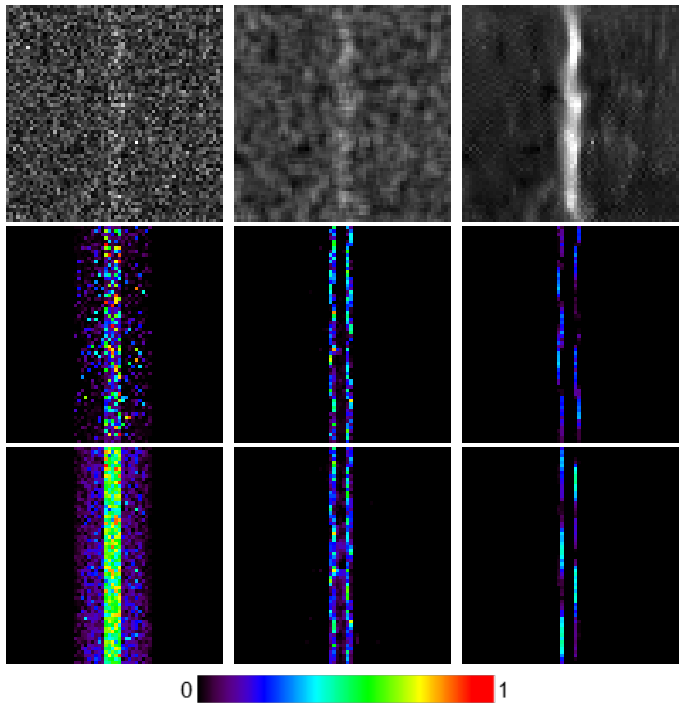

Figure 4.3: Error maps for a 64×64-pixel close-up of the simulated scene with low contrast: $A_F/A_B = \sqrt{2}$. From left to right: no prefiltering, 3×3 multilooking, and SAR-BM3D. From top to bottom: single-band amplitude images, error maps with KS measure, error maps with PB measure. Error maps are color-coded according to the bottom colorbar.

Fig. 4.3 shows, for this low-contrast case, some filtered amplitude images and the corresponding error maps. On the left, there is the case of no prefiltering. Indeed, it seems very difficult to tell apart foreground from background based on these data (remember, though, that several bands are available) and in fact the error maps are rather bright both for KS and PB, with different patterns. A 3×3 multilooking, center column, does not seem to improve data quality very much, besides loosing resolution. Nonetheless, in the interior of both regions, the probability of error reduces significantly, remaining large only near the smoothed boundaries (again, KS works somewhat better than PB). This behavior becomes more evident when the amplitude contrast increases, in which case, the error maps (not shown) are completely black except for two parallel green lines on the outer foreground boundary. Using SAR-BM3D, right column, a stronger speckle reduction is observed and, what is more important, the foreground/ background edges are well preserved, with no evident smearing. In this low-contrast case, some sparse errors are still visible, which disappear at higher contrasts.

Tab. 4.2 shows results for the case in which the foreground region has an amplitude history. In this case, the relative performance of the two similarity measures is reversed, with PB generally outperforming KS. This gap is again easily explained, considering that the PB measure compares same-band samples, and hence takes advantage of the amplitude history, while the sorting step of the KS measure erases such history. Except for this major difference, the general behavior is the same as that of Tab. 4.1, with the SAR-BM3D prefiltering improving significantly the selection accuracy. In all cases, errors tend to cluster preferably on region boundaries, even when the resolution-preserving SAR-BM3D is used. Again, the standard deviation is very low for all estimates. Finally, to provide insight into the effects of the various

		no filtering		3×3 boxcar		SAR-BM3D	
F/B	Δ_F	KS	PB	KS	PB	KS	PB
F	0.8	266 (9)	105 (9)	71 (4)	164 (6)	0 (0)	0 (0)
	0.4	678 (9)	593 (9)	271 (11)	173 (7)	88 (13)	22 (5)
	0.2	721 (6)	696 (10)	621 (13)	439 (18)	238 (17)	243 (27)
B	0.8	63 (3)	6 (1)	16 (3)	15 (2)	5 (2)	0 (0)
	0.4	235 (3)	159 (6)	70 (5)	35 (3)	31 (5)	1 (1)
	0.2	249 (4)	236 (11)	212 (9)	110 (8)	101 (11)	60 (12)

Table 4.2: Probability of selection error (×1000) in the presence of amplitude history. In parentheses, the st.dev. (×1000).

forms of filtering on the quality of actual products of the processing chain, some average coherence maps obtained in the most challenging situations are shown.

Fig. 4.4 shows maps relevant to the low-contrast, $A_F/A_B = \sqrt{2}$, fixed amplitude case. BML causes the expected blurring of boundaries, enlarging the central strip where a higher coherence is estimated. AML with KS measure, instead, preserves the geometrical structures; the higher coherence strip emerges quite clearly, although with some localized errors, even in the absence of prefiltering, and is recovered almost perfectly with SAR-BM3D prefiltering.

In Fig. 4.5, we consider the variable amplitude case, taking again the worst case of $\Delta_F = 0.2$. Here, the situation is even worse than in the preceding case, because the amplitudes of foreground and background are barely different, and only in some of the bands. In fact, when no prefiltering is used, predictor selection is almost random, and AML

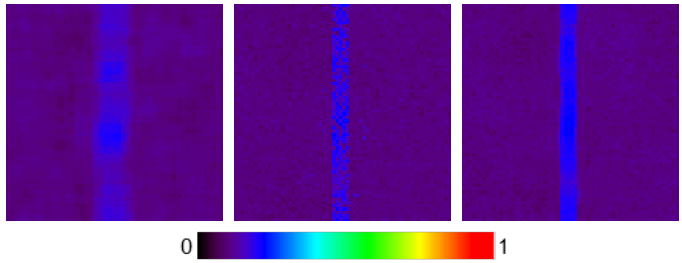

Figure 4.4: Average coherence maps for a 64×64-pixel close-up of the simulated scene with low contrast: $A_F/A_B = \sqrt{2}$. From left to right: boxcar multilooking; adaptive multilooking with KS measure and no prefiltering; adaptive multilooking with KS measure and SAR-BM3D prefiltering.

is even worse than BML because of its larger analysis window. However, when data quality improves somewhat thanks to SAR-BM3D prefiltering, AML with PB measure recovers reasonably well the correct coherence map even in these adverse conditions.

4.4 Experiments on real data

In the following the results of experiments carried out on real-world data are shown, considering two interferometric stacks, acquired by the ENVISAT and COSMO-SkyMed sensors, respectively, in order to test performance on both low and high spatial resolution data.

Quality Indexes

The effectiveness of the various work-flows has been evaluated by means of three different quality indexes, derived from the interferometric processing framework, and relevant to different levels of the processing. The first index takes into account the interferometric

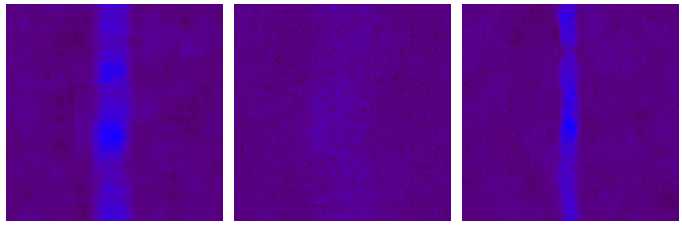

Figure 4.5: Average coherence maps (same colorbar as Fig.Fig. 4.4) for a 64×64-pixel close-up of the simulated scene with low-contrast variable amplitude: $\Delta_F = 0.2$. From left to right: boxcar multilooking; adaptive multilooking with PB measure and no prefiltering; adaptive multilooking with PB measure and SAR-BM3D prefiltering.

coherence in 4.4 evaluated pixel-wise, for each interferometric pair. Specifically, the sample estimate of the complex correlation associated with the interferogram produced by the ith and jth images, for pixel p, is given by:

$$\hat{\rho}_{c_{i,j}}(p) = \frac{\sum_{q\in\Omega_S(p)} u_i(q)\, u_j^*(q)}{\sqrt{\sum_{q\in\Omega_S(p)} |u_i(q)|^2 \sum_{q\in\Omega_S(p)} |u_j(q)|^2}} \tag{4.13}$$

where $\Omega_S(p) \subset \Omega(p)$ singles out the S predictor pixels, belonging to the rectangular box for BML or selected according to similarity measures for AML. The phase of the correlation represents the estimated multilook interferometric phase, whereas its amplitude, with values in the $(0, 1)$ interval, is the coherence, which depends on the phase stability over the interferometric pair, and therefore provides information on the reliability of the phase estimate. Notice that the expression in eq. 4.13 is the amplitude normalized version of eq. 4.6 for the case in which weights are set to $1/S$ for the predictor pixels and 0 elsewhere. From the estimates of the coherence, the first quality index

as the mean coherence is derived by averaging over the M, out of the available $N(N-1)/2$, small-baseline interferograms:

$$\bar{\rho}\,(p) = \frac{1}{M}\sum_{m=0}^{M-1}\left|\hat{\rho}_{c_{i,j}}\,(p)\right| \tag{4.14}$$

The mean coherence measures the average quality of the produced subset of interferograms, and therefore allows one to tell apart areas where the interferometric phases provide reliable information from those heavily corrupted by decorrelation phenomena and basically useless. It is worth noting this selection is performed directly at the interferogram generation stage, at the beginning of the processing. The accurate selection of expected reliable pixels improves the performance of the interferometric processing aimed at extracting the physical information of interest related to topography and displacement of the observed surface. The second quality index is found on the measurement of the correlation between the interferogram stack and the multipass interferometric model $\boldsymbol{s}$ in 2.33 and 2.32, describing the signal associated with a target located at height z and moving with a temporal average velocity v along the radar line-of-sight (LOS):

$$\boldsymbol{s}(h,v) = \exp\left[-j\frac{4\pi}{\lambda}\left(\frac{\boldsymbol{\Delta b}}{r_0 sin(\vartheta)}z + \boldsymbol{\Delta t} * v\right)\right] \tag{4.15}$$

In eq. 4.15 $\boldsymbol{\Delta b} = [\Delta b_0, ..., \Delta b_{M-1}]^T$ and $\boldsymbol{\Delta t} = [\Delta t_0, ..., \Delta t_{M-1}]^T$ are the M-dimensional vectors collecting the interferometric spatial and temporal baselines associated with the interferogram stack, while λ, r_0 and ϑ are, respectively, the radar system working wavelength, the distance of the sensor from the target and the incidence angle in the

reference geometry of acquisitions [31].

The correlation of the data with the model in eq. 4.15 is usually exploited in PS techniques on a pixel-by-pixel basis after the calibration of the phase signal associated with atmospheric disturbances, to detect the presence of persistent scatterers [30, 33]. Aiming at the comparison of the different filtering solutions, however, we do not perform any atmospheric compensation and, therefore, use 4.15 over spatial arcs connecting adjacent pixels, as done in [32]. More specifically, for each pixel p, the phase variation over the arc is computed as $\Delta\hat{\boldsymbol{\Gamma}}_\psi(p) = \hat{\boldsymbol{\Gamma}}_\psi(p) \odot \hat{\boldsymbol{\Gamma}}^*_\psi(p+1)$, where $(p+1)$ denotes the adjacent pixel in horizontal, vertical or diagonal directions. The model in eq. 4.15 is also particularized by introducing the height and velocity differences, denoted by $(\Delta z, \Delta v)$, in place of the single-pixel parameters pair (z, v). Finally, the multipass correlation index $C(p)$ along any spatial arc starting from pixel p is computed through the maximization of the (normalized) scalar product between the multibaseline model $s(\Delta z, \Delta v)$ and the phase-difference vector $\Delta\hat{\boldsymbol{\Gamma}}_\psi(p)$ as:

$$C(p) = \max_{(\Delta h, \Delta v)} \frac{\boldsymbol{s}(\Delta z, \Delta v)^H \Delta\hat{\boldsymbol{\Gamma}}_\psi(p)}{M} \tag{4.16}$$

The last quality index measures the consistency of phases derived from the crucial step of phase unwrapping. It involves the linear system relating the interferometric (differential) unwrapped measurements $\boldsymbol{\psi}_{unw}(p)$ to the (unwrapped) phases at the level of acquisitions collected in the vector $\boldsymbol{\theta}(p)$

$$\boldsymbol{\psi}_{unw}(p) = \boldsymbol{A}\boldsymbol{\theta}(p) \tag{4.17}$$

where $\boldsymbol{A}$ is the $M \times N$ incidence matrix defining, on each row, the acquisitions pair involved in the interferometric beating. Said $\boldsymbol{\theta}_{LS}(p)$

the solution of the linear system in 4.17 in the Least Square (LS) sense, the consistency index $Q(p)$ measures the residual error between the original unwrapped interferograms and the interferograms corresponding to $\boldsymbol{\theta}_{LS}(p)$ [34, 85]:

$$Q(p) = \left| \frac{\left(e^{j\boldsymbol{\psi}_{unw}(p)}\right)^{H} e^{j\boldsymbol{A}\boldsymbol{\theta}_{LS}(p)}}{M} \right| \tag{4.18}$$

where, in particular, the quantity $\boldsymbol{\psi}_{unw}(p) - \boldsymbol{A}\boldsymbol{\theta}_{LS}(p)$ measures the amount of signal in the null space of $\boldsymbol{A}$ due to unwrapping errors. The consistency index $Q(p)$ takes values in the $(0, 1)$ interval: values close to 1 indicate that the spatial unwrapping procedure has generated low residual errors in the LS inversion, *i.e.* the independent spatial unwrapping of each interferogram has generated a set of unwrapped interferograms which are "consistent" in the baseline domain.

4.4.1 Results on low-resolution data

We consider a low-resolution interferometric stack comprising 31 images acquired in stripmap mode during ascending passes of the ENVISAT satellite spanning a time interval of about 5 years from June, 2003 to April, 2008. The processing has been limited to a 1000×1000 pixels patch of the full available frame, relevant to the area surrounding the airport of Bari, in southern Italy. The temporal multilook amplitude image of the area under investigation is shown in Fig. 4.6. According to the SBAS approach, a total of 66 small-baseline interferograms have been generated. They are represented as arcs connecting the different acquisitions, depicted as diamonds, in the temporal/spatial baseline grid in Fig. 4.7.

Figure 4.6: Amplitude image of the area under investigation. Horizontal and vertical directions correspond to azimuth and range, respectively.

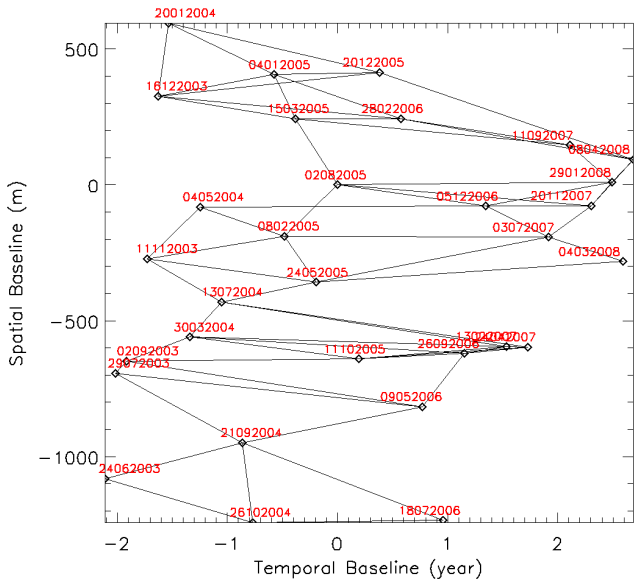

Figure 4.7: Distribution of ENVISAT acquisitions (diamonds) in the temporal/spatial baseline grid. Labels indicate the date of acquisition.

The reference interferograms have been generated through classical boxcar multilooking (BML), using a window of 20×4 pixels in azimuth and range, respectively, so as to obtain multilooked pixels that are approximately square, with 80m sides. Originally, this filtering step aimed also at reducing data volume and CPU-time in SBAS processing, through a suitable subsampling [5, 32]. Currently, however, these practical problems are less compelling, and the main goal of filtering is improving the reliability of estimates and therefore, in our experiments, subsampling is ignored. The average coherence map provided by BML is shown in Fig. 4.8. It allows one to recognize clearly the presence of coherent areas, corresponding to urban settlements and airport runaways. However, the loss of resolution induced by the

boxcar filtering is also well visible. In the presence of stable scatterers, coherence is retained over the whole filtering window. This effect is especially evident in the lower-right part of the map where concentrated scatterers located in low backscattering areas produce rectangular high-coherence boxes. In addition, the shape of ground structures, roads, and in general the boundaries between areas with different coherence properties, lose detail and often can be hardly distinguished.

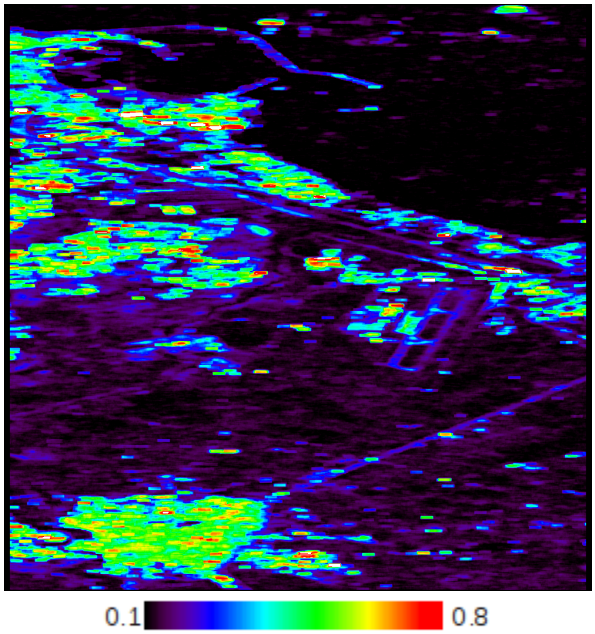

Figure 4.8: Mean coherence map provided by BML for the Bari image.

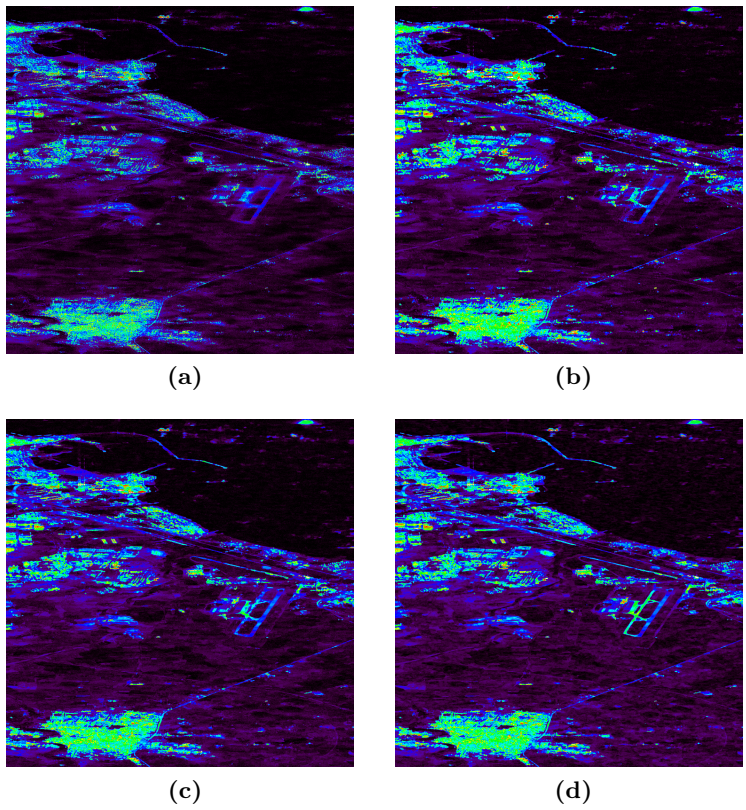

(a) **(b)**

(c) **(d)**

Figure 4.9: Mean coherence maps (same colorbar as Fig.Fig. 4.8) provided by AML for the Bari image. (a) KS distance measure with no prefiltering, (b) KS with 3×3 boxcar filtering, (c) KS with SAR-BM3D filtering, (d) PB with SAR-BM3D filtering.

Adaptive multilooking techniques aim at solving these problems and improving the overall performance. In Fig. 4.9(a) we can appreciate the effect of using AML, with KS distance and no prefiltering, on the same original data. With respect to the case of BML, the coherence map shows a much better spatial resolution, and coherence spreading is avoided. Moreover, narrow coherent shapes are preserved, like the

roads and the wharf in the upper left part of the image. It is worth reminding that the same number of looks, $S = 80$, is used in all cases, and only the selection of predictors has changed, based on a measure of similarity in AML, allowing one to perform multilooking only on pixels that are likely homogeneous. The use of a prior despeckling step on the original data aims therefore at improving the reliability of the similarity measure. In Fig. 4.9(b) we show the coherence map provided by AML with KS distance and 3×3 boxcar prefiltering of the amplitudes. This simple additional step guarantees higher coherence values, in general, at the price of a little resolution loss caused by the despeckling. Airport runways, for example, are much better defined, and the coherence in generally higher in all urban areas, thus increasing the contrast of the image. Replacing boxcar prefiltering with the more sophisticated SAR-BM3D, we avoid also the resolution loss problem, as shown in Fig. 4.9(c), and in general guarantee a better speckle rejection on the original amplitude data, at the price of a limited increase of complexity. As the last step of this path, Fig. 4.9(d) shows the coherence map provided by AML with the PB similarity measure, always with SAR-BM3D prefiltering. Although the quality of the map is quite similar to the previous case, there are significant improvements in some selected areas, notably on the left runway of the airport as well as on some service roads near it which exhibit a higher coherence.

To better appreciate visually the phenomena described above, Fig. 4.10 shows a close-up on the airport area of the coherence maps provided by the four more relevant AML workflows reported in Fig. 4.9.

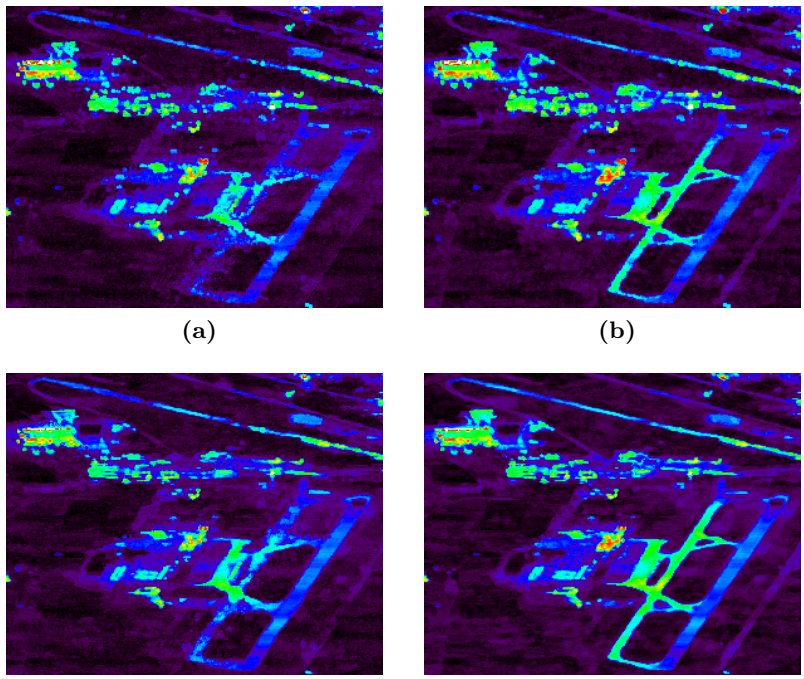

(a) **(b)**

(c) **(d)**

Figure 4.10: Close-up on the airport area of the mean coherence maps (same colorbar as Fig.Fig. 4.8) provided by (a) KS + 3×3 boxcar, (b) KS + SAR-BM3D, (c) PB + 3×3 boxcar, (d) PB + SAR-BM3D.

This improvement can be very likely attributed to the higher robustness of PB w.r.t. time changes in data amplitude. To support this claim, Fig. 4.11 shows the acquisitions taken at different times over an area including the airport. In the first image, acquired in July 2003, the airport runaways can be hardly distinguished from the surrounding areas, while they are easily recognized in the successive acquisition, just 35 days later. The same behaviour is observed in the last two images, acquired in July and September 2006, suggesting a seasonal

phenomenon, probably depending on grass growth. The PB measure compares time vectors as they are, preserving temporal changes, while KS sorts them, allowing the observed errors.

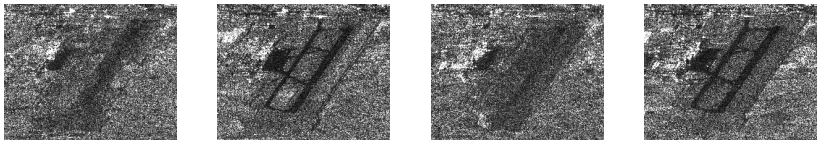

(a) **(b)** **(c)** **(d)**

Figure 4.11: Zoom of the amplitude images over the area of the airport at different acquisition epochs, (a) 29/07/2003, (b) 02/09/2003, (c) 18/07/2006, (d) 26/09/2006.

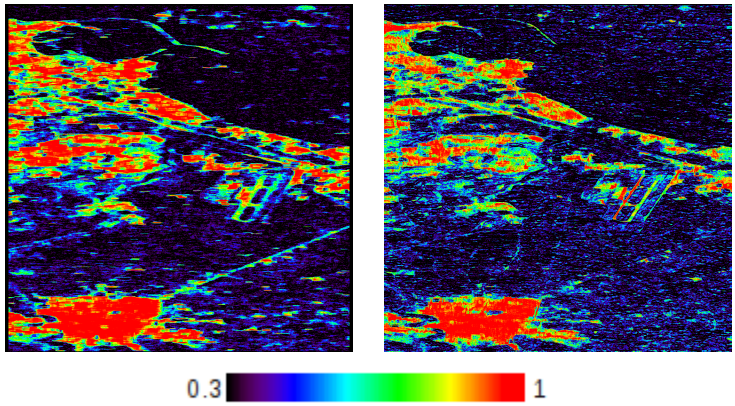

Figure 4.12: Maps of the correlation index in (4.16) over vertical arcs provided by BML and by AML with PB measure and SAR-BM3D prefiltering

Let us now consider the other quality indexes. In Fig. 4.12 we compare the map of the index defined in eq. 4.16 (the correlation between measured interferometric spatial arcs and multipass model) provided by the BML originally used in SBAS processing, and by the most

sophisticated AML proposed here, with PB similarity measure and SAR-BM3D prefiltering. The improvement already observed on average coherence is obvious in these maps as well, as adaptive multilooking preserves spatial resolution avoiding the correlation spreading induced by boxcar filtering.

Fig. 4.13 shows a close-up, near the airport, of the maps provided by the various versions of AML. They confirm the better ability of SAR-BM3D to preserve resolution and the superior performance of the PB measure in areas affected by temporal variability.

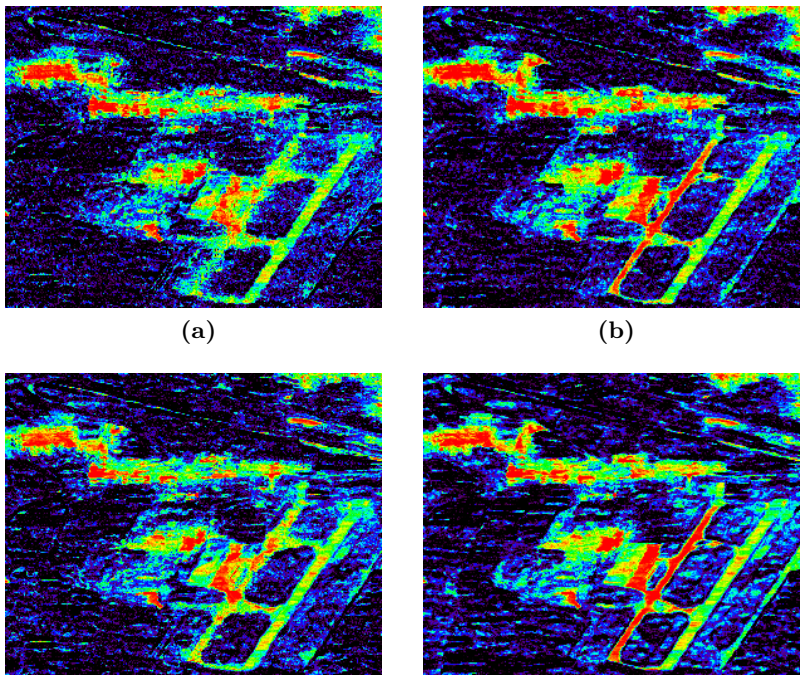

Figure 4.13: Close-up on the airport area of the Correlation Index maps (same colorbar as Fig.Fig. 4.12) provided by (a) KS + 3×3 boxcar, (b) KS + SAR-BM3D, (c) PB + 3×3 boxcar, (d) PB + SAR-BM3D.

Finally, in Fig. 4.14 and Fig. 4.15 we show results for the last quality index, which measures the phase consistency after phase unwrapping. This index is of paramount importance as it defines the output grid of sparse pixels for measurement of deformation time series and topography information derived by interferometric processing. Adaptive multilooking outperforms significantly the basic version, which is characterized by large unwrapping errors in the urban areas in the lower part of the image. Turning to the comparison among the various ver-

sions of AML, however, we observe results that seem to contradict previous findings. In particular, while KS similarity measure takes advantage, in terms of phase unwrapping consistency, of SAR-BM3D prefiltering w.r.t. plain 3×3 boxcar, the same does not reflect in case of PB similarity measure. In that case, contrary to what happens for other indexes, SAR-BM3D reduces phase consistency in several areas of the image. At a deeper analysis, though, this phenomenon can be satisfactorily explained: as proven by the former quality indexes, the PB selection with prior SAR-BM3D prefiltering provides the best performance in terms of amplitude of mean coherence and, above all, correlation with the multipass model. At the same time, it provides the best performance in terms of boundary preservation which, in the presence of structures and facilities, is strictly related to the preservation of height, and therefore interferometric phase, discontinuities. Such large height variations, which are consistent with the expected interferometric phase signature, as shown in Fig. 4.12 and Fig. 4.13(d), are detrimental to the correct execution of phase unwrapping, which in our experiments is performed independently on all the original multilook interferograms. In real application scenarios, however, phase unwrapping is typically model-based driven, operating a prior estimation and compensation of contributions associated with large phase discontinuities to limit the occurrence of unwrapping errors. These advanced solutions would take full advantage of the superior quality provided by adaptive multilooking.

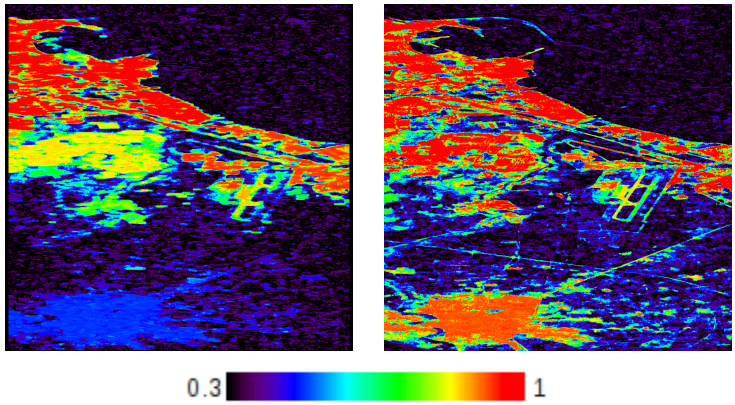

Figure 4.14: Maps of the consistency index in (4.18) provided by BML and by AML with PB measure and SAR-BM3D prefiltering.

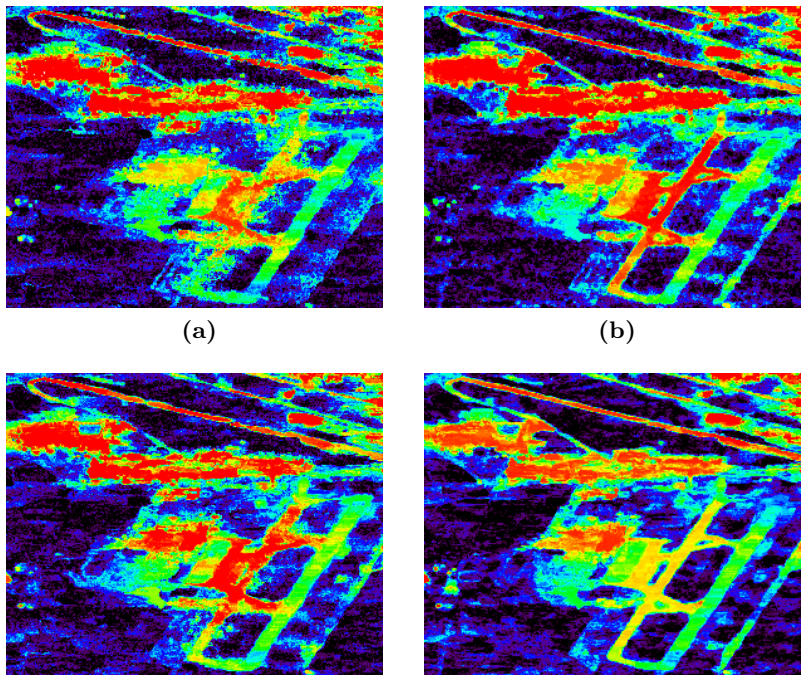

Figure 4.15: Close-up on the airport area of the Consistency Index maps (same colorbar as Fig.Fig. 4.14) provided by (a) KS + 3×3 boxcar, (b) KS + SAR-BM3D, (c) PB + 3×3 boxcar, (d) PB + SAR-BM3D.

4.4.2 Results on high-resolution data

Sensors of the last generation provide data with higher and higher spatial resolution, which are extremely valuable for a number of advanced applications. A major concern when using such data, however, is that the hypothesis of fully developed speckle does not hold anymore, casting doubts on the validity of the processing tools developed under such a simplifying assumption. Therefore, we carried out experiments on

a high-resolution COSMO-SkyMed dataset in order to confirm the effectiveness of the proposed filtering also in this condition.

The test site is relevant to a rural area near Naples, Italy. The dataset is composed by 28 H-Image mode (3m spatial resolution) images spanning a temporal interval of one year, from February 2010 to February 2011, acquired during descending passes of the sensor. The temporal multilook amplitude image of the area under investigation, reported in Fig. 4.16, shows mostly farmlands and isolated roads, with a well recognizable industrial settlement. A total of 79 small-baseline interferograms have been computed. Acquisitions and interferograms are depicted as diamonds and arcs, respectively, in Fig. 4.17

Figure 4.16: Amplitude image of the area under investigation. Horizontal and vertical directions correspond to range and azimuth , respectively.

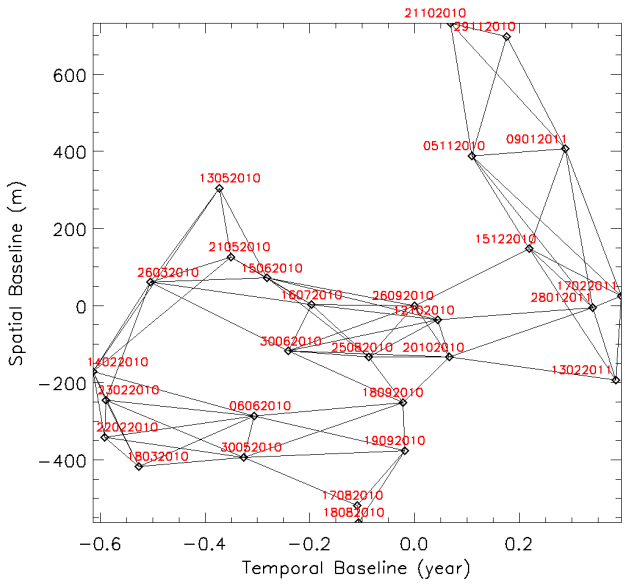

Figure 4.17: Distribution of COSMO-SkyMed acquisitions (diamonds) in the temporal/spatial baseline grid. Labels indicate the date of acquisition.

We repeated all experiments as for the previous dataset, using, however, a window of 16×16 pixels for basic multilooking, and selecting, correspondingly, $S = 256$ predictor pixels for adaptive multilooking, more than three times those used for ENVISAT. Despite all differences, results exhibit the same behavior already observed in the low-resolution case. Therefore, in the following, we show and comment only a few sample cases of interest.

Fig. 4.18 shows the mean coherence maps provided by BML and by the best AML technique, using PB selection and SAR-BM3D prefiltering. AML guarantees a dramatic improvement on boundaries, preserving the shapes of buildings, defining more clearly the road in the bottom part of the image and keeping the original spatial resolution even in

the cultivated fields.

Similar improvements emerge when considering the second quality index, associated with the correlation between the interferometric spatial arcs and the multipass model. Besides the better resolution, especially evident on buildings and roads, a much higher correlation with the multipass model is observed in the region of the cultivated fields. We note explicitly that the other AML combinations, not shown here for brevity, provide quite similar results, although PB is slightly preferable to KS, especially if associated with SAR-BM3D prefiltering.

Finally, Fig. 4.20 shows results concerning the last quality index, measuring consistency of phases after unwrapping and defining, therefore, the grid of output measurement points. Classical boxcar averaging (top) allows to correctly unwrap only the region corresponding to the large industrial settlement, whereas the rest of the image is characterized by large unwrapping errors. On the contrary, AML returns a higher and better defined consistency index improving significantly the performance of phase unwrapping, and allowing the correct unwrapping of other relevant features, such as the roads and the urban settlement in the lower-left part of the image. For this last index, we show also the AML map obtained with KS selection and 3×3 prefiltering, since, on the ENVISAT dataset, this combination provided results significantly different from those of the PB/SAR-BM3D combination. This is not the case anymore with COSMO-SkyMed data. The phase inconsistencies observed formerly with PB/SAR-BM3D disappear altogether, likely because the higher spatial sampling helps the unwrapping in following the large height variations well preserved by the BM3D pre-filtering.

It is also to be noted that, whatever the quality index, given the shorter time span of the acquisitions (about one year as opposed to

the five years of the ENVISAT dataset) the KS-based AML suffers less the selection problems due to significant temporal variations of amplitude, as observed in the ENVISAT case.

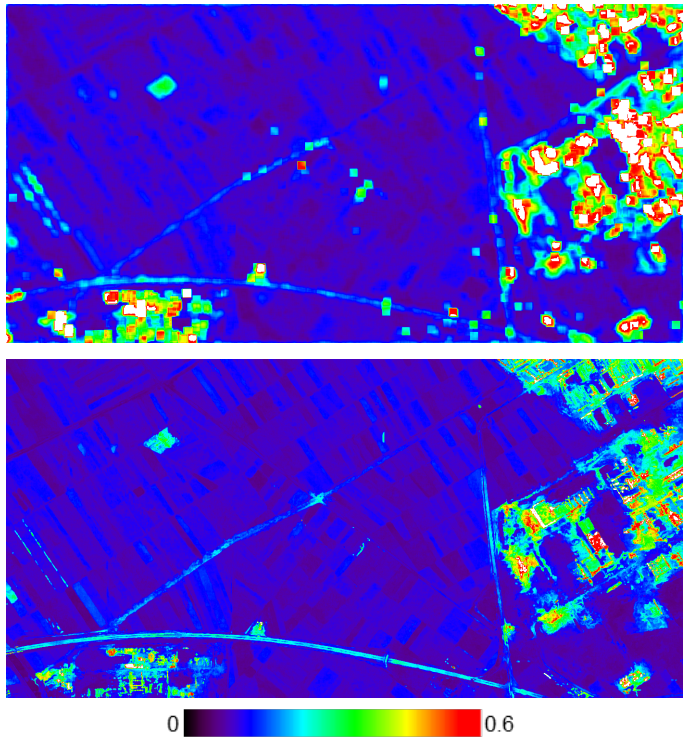

Figure 4.18: Mean coherence maps provided by BML (top), and AML with PB and SAR-BM3D filtering (bottom) for the COSMO-SkyMed Image.

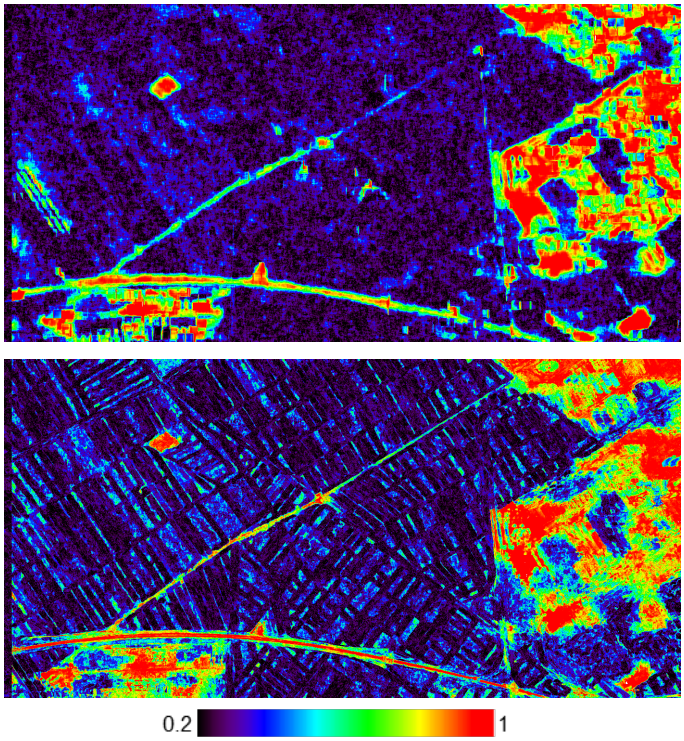

Figure 4.19: Correlation Index maps provided by BML (top), and AML with PB and SAR-BM3D filtering (bottom) for the COSMO-SkyMed Image.

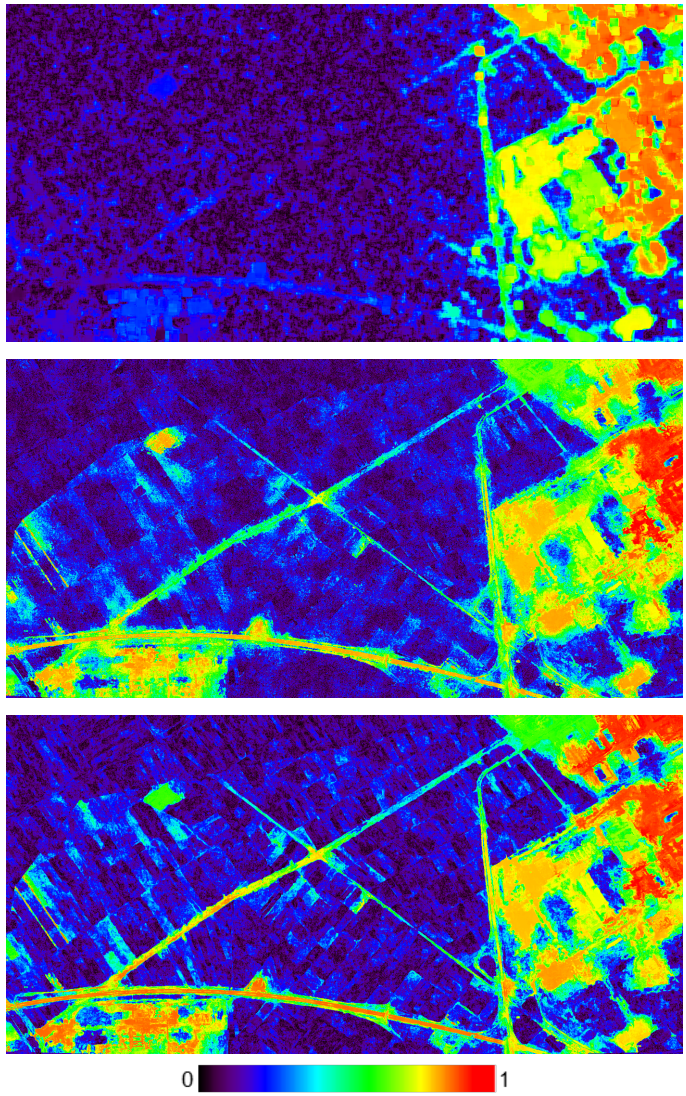

Figure 4.20: Consistency index maps provided by BML (top), AML with KS and 3×3 boxcar filtering (center), AML with PB and SAR-BM3D filtering (bottom) for the COSMO-SkyMed Image.

5 Non-Local LLMMSE estimation for single-pair InSAR

5.1 Overview

Across-Track Interferometry was conceived with the aim of acquiring the height information in addition to the bidimensional range-azimuth SAR representation. Latest high-resolution InSAR systems, such as the German Tandem-X or the Italian COSMO-SkyMED, have the aim of providing high-resolution SAR data and allow the generation of high-resolution DEM. In order to preserve the resolution of the original data and, at the same time, improve the reliability of the phase measurement, appropriate filtering methods are necessary. In this field the nonlocal approach has provided excellent solutions with NLInSAR [20] and NLSAR [22], based directly on the Non-Local-Means [7] algorithm.

Non-Local-Means itself, however, has been surpassed by more recent denoising techniques based on a nonlocal multipoint approach, like the BM3D [15, 16]. This algorithm is based on an hybrid approach that exploits both the spatial and transformed domain. It uses the nonlocal approach to find similar *blocks* according to an Euclidean metric, but, unlike the Non-Local-Means, the blocks are stacked together in a 3D structure, named *group*, to which a decorrelating transform is applied so as to exploit both spatial and contextual dependencies.

This functioning of the BM3D algorithm is explained in detail in the following.

A similar approach can fit well the case of InSAR phase estimation, given the high redundancy of the InSAR signal. On the track of the BM3D approach, an algorithm for interferometric phase estimation, the InSAR-BM3D, is proposed in the following.

5.2 BM3D

The Block Matching 3D denoising method for AWGN images extends the Non-Local-Means by combining it with other approaches and can be considered the state-of-the-art for AWGN denoising [16]. BM3D takes advantages of three winning ideas to image denoising: the non local approach, the wavelet domain shrinkage and Wiener filtering. BM3D is based on two steps, each consisting of three phases:

(a) Grouping

(b) Collaborative filtering

(c) Aggregation

The *grouping* step consists in collecting similar d-dimensional fragments of a given signal into a $d+1$-dimensional data structure named *group*. In the case of a bidimensional signal, an image for example, the signal fragments are small 2D *blocks* of pixels, and a group is a 3D array formed by stacking together similar image blocks. This exploits the neighborhood definition introduced by Non-Local-Means. The importance of grouping is to enable an higher-dimensional filtering of each group, which exploits the potential similarity between grouped fragments.

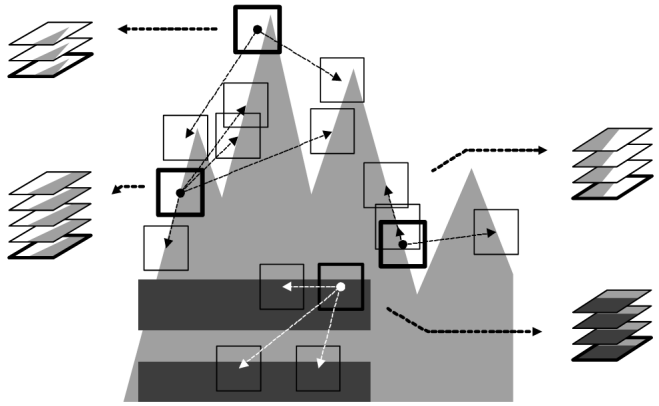

Figure 5.1: A simple example of grouping in an artificial image [16].

A simple and effective grouping is realized in BM3D by *block matching*. It is used to find signal fragments similar to a given reference, and the formed groups aren't necessarily disjoint. The similarity plays the role of a membership function. Any signal fragment can be used as a reference and thus a group can be constructed for it. A simplified example of block matching is shown in Fig. 5.1.

The *collaborative filtering* is the actual estimation step. The term collaborative indicates the fact that each of the blocks belonging to a group collaborates to the filtering of all the others. BM3D performs a collaborative filtering based on the shrinkage in a specific transform domain. Assuming d+1-dimensional groups of similar signal fragments are already formed, the collaborative shrinkage comprises the following steps:

- apply a d+1-dimensional linear transform to the group;
- shrink the transform coefficients to attenuate the noise;
- invert the linear transform to produce estimates of all grouped

fragments.

It is worth noting that collaborative transform-domain shrinkage is particularly effective in the case of natural image fragments, in fact these exhibit both intra-fragment correlation, that is a peculiarity of natural images, and inter-fragment correlation due to the preliminary grouping procedure. When the estimates are computed, the signal fragments are relocated in their original position. Since the groups are not disjoint, and blocks can overlap, for each signal sample many estimates are available. The *aggregation* procedure consists in computing the final estimate by averaging, for each signal sample, all the available estimates, each one with a proper weight.

In the BM3D algorithm, the above mentioned procedures are implemented in two different *steps*. The first step provides a denoised version of the image, called *basic estimate*, that is exploited in the second step to perform a more accurate *final estimate*. The algorithm is described more formally in Algorithm 5.1 and its related flow chart depicted in Fig. 5.2. At step 2 the grouping is performed on the basic estimate image, thus improving its reliability. The collaborative filtering, at step 1 is performed with an hard-thresholding, while at the second step the basic estimate is used as the pilot signal for the empirical Wiener filtering, thus improving the effectiveness and the accuracy of the filtering w.r.t. the basic estimate.

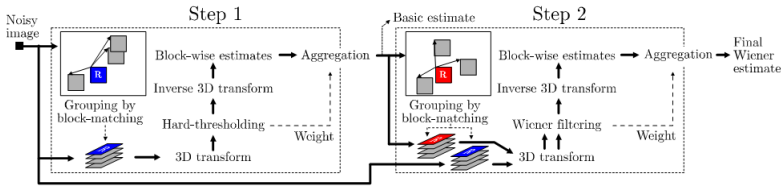

Figure 5.2: BM3D algorithm flow chart [16].

Algorithm 5.1 BM3D algorithm [16].

Step 1. Basic estimate:

- i) Grouping: find blocks that are similar to the target block and stack them in a 3D array (*group*).
- ii) Collaborative Wiener filtering: apply a 3D WT transform to the group, attenuate the noise by hard-thresholding of the transform coefficients, invert the WT transform to produce estimates of the grouped blocks, and return the estimates of the blocks to their original positions.
- iii) Aggregation: compute the basic estimate of the true image by weighted averaging all of the obtained block-wise estimates that are overlapping.

Step 2. Final estimate

- i) Grouping: use BM within the basic estimate to find the locations of the blocks similar to the target block. Form two groups, one from the noisy image and one from the basic estimate.
- ii) Collaborative Wiener filtering: apply a 3D WT transform on both groups. Perform Wiener filtering on the noisy one using the energy spectrum of the basic estimate as the true (pilot) energy spectrum. Produce estimates of all grouped blocks by applying the inverse WT transform on the filtered coefficients and return the estimates of the blocks to their original positions.
- iii) Aggregation: compute a final estimate of the true image by aggregating all of the obtained local estimates using a weighted average.

5.3 InSAR-BM3D

In the following combinations of grouping and collaborative filtering are investigated in order to find which one suits best the InSAR signal peculiarities. The complex interferogram is filtered separately in its real and imaginary part, an appropriate noise decorrelation step is then performed before the filtering. The previous works on similarity computation for InSAR statistics [20, 22] are used to define a grouping strategy at the two steps. Two different strategies for the basic estimate are investigated: the shrinkage problem is addressed in the framework of statistical estimation, using the signal-dependent additive noise model in sec. 5.3.1.

5.3.1 Signal model

In addition to the statistical description in [65, 66, 72] reported in sec. 2.4, the complex interferogram can be statistically described as follows. Let (A, ψ, ρ) be the true amplitude, interferometric phase and coherence, respectively. The InSAR pair $(u_1, u_2)^T$ is expressed as a function of two standard circular gaussian random variables $(x_1, x_2)^T$

$$\begin{pmatrix} u_1 \\ u_2 \end{pmatrix} = L \begin{pmatrix} x_1 \\ x_2 \end{pmatrix} \tag{5.1}$$

where the matrix L is

$$L = \begin{pmatrix} A_1 & 0 \\ A_2 \rho e^{-j\psi} & A_2\sqrt{1-\rho^2} \end{pmatrix} \tag{5.2}$$

Starting from equation 5.1, the expression for the complex interferogram Γ can be obtained

$$\mathit{\Gamma} = u_1 u_2^* = A_1 A_2 \rho e^{j\psi} + n = \mathit{\Gamma}_0 + n \tag{5.3}$$

where for the noise n holds

$$n = A_1 A_2 \rho e^{j\psi} \left(|x|^2 - 1 \right) + A_1 A_2 \sqrt{1-\rho^2} x_1 x_2^* \tag{5.4}$$

Therefore, the complex interferogram is expressed as the sum of its true value $\mathit{\Gamma}_0$ and a signal-dependent noise contribution, whose correlation matrix C_n can be shown to be:

$$C_n = \frac{1}{2} A_1^2 A_2^2 \begin{pmatrix} 1 + \rho^2 \cos(2\psi) & \rho^2 \sin(2\psi) \\ \rho^2 \sin(2\psi) & 1 - \rho^2 \cos(2\psi) \end{pmatrix} \tag{5.5}$$

The terms on the diagonal are the variances of the real and imaginary part of the noise n, respectively, while the off-diagonal terms are their mutual correlations.

5.3.2 Noise decorrelation

Since real and the imaginary part are filtered separately, it is desirable that the associated noise components be uncorrelated. From eq. 5.5 it appears that the correlation between the real and imaginary noise components depend mainly on the interferometric phase value ψ. Note

also that, depending on the values of the SLCs' values A_1 and A_2 this correlation may happpen to be very large.

The noise decorrelation step applies to every formed group. Since the block size is generally small, the hypothesis of stationary phase over the block can be reasonably made allowing one to apply the phase Maximum Likelihood Estimator over the pixels of the group. By subtracting the estimated phase value from each block of the group, eq. 5.5 reads eventually as follows:

$$C_n = \frac{1}{2} A_1^2 A_2^2 \begin{pmatrix} 1+\rho^2 & 0 \\ 0 & 1-\rho^2 \end{pmatrix} \tag{5.6}$$

5.3.3 Grouping

In order to form a group of similar blocks one can rely on the phase information only, or else on the triple formed by phase, amplitude and coherence, as shown in [20, 22]. As far as phase estimation is concerned, both approaches, depending on the kind of data, provide satisfactory results. In general, it is convenient to use all the available information, especially when the degree of correlation between amplitude and phase is large. Nonetheless, there are cases in which a constant amplitude may correspond to a highly variable interferometric fringe patterns, and the use of the phase information only is more advisable. In previous works on interferometric blocks similarity computation [10, 20–22] it has been shown that phase similarity results always in a cosine distance between phase values as we define in the following. Let ψ_p and ψ_q be the interferometric phase blocks centered on the target pixel p and the comparison pixel q, respectively, and let N be the number of pixels in the block. Then the cosine distance D

between the two blocks

$$D = D_1 = 1 - \frac{1}{N}\sum_{i=1}^{N}\cos\left(\psi_{p_i} - \psi_{q_i}\right) \tag{5.7}$$

expresses their degree of dissimilarity, where the subscript 1 indicates that the distance is related to the first filtering step. This quantity varies between 0 and 2, with small values indicating similar blocks. At the second filtering step an estimation of the interferometric phase is already available, hence it can be used in formula 5.7 in place of the noisy blocks. In general, this leads to a more accurate similarity computation but, at the same time, possible errors and artifacts introduced in the first filtering step can bring to a erroneous grouping. Hence, a good practice is not to fully rely on the first step estimate and consider also with suitable weight the noisy interferogram. By taking this idea into account, the second-sted distance reads as

$$\begin{aligned} D_2 &= \gamma D\left(\hat{\psi}\right) + (1-\gamma)\, D\left(\psi\right) = \\ &= \tfrac{\gamma}{N}\sum_{i=1}^{N}\cos\left(\hat{\psi}_{p_i} - \hat{\psi}_{q_i}\right) + \tfrac{1-\gamma}{N}\sum_{i=1}^{N}\cos\left(\psi_{p_i} - \psi_{q_i}\right) \end{aligned} \tag{5.8}$$

where $\hat{\psi}$ indicates the pre-estimated phase, and the quantity γ, which lies in the interval $[0, 1]$, establishes the relative weights between the pre-estimated quantity and the new estimate based on the original data. The most suitable γ should be found experimentally, but a good result is generally given by $\gamma = 0.5$. Alternatively, if an estimation of the coherence is available, this weight can be substituted by the product of the coherence of reference and comparison blocks: $\gamma =$

$\rho_p \rho_q$. This choice relies on the fact that the coherence is an indicator of the quality of the estimation. With this position, formula (5.8) becomes

$$D_2 = \frac{\rho_p \rho_q}{N} \sum_{i=1}^{N} \cos\left(\hat{\psi}_{p_i} - \hat{\psi}_{q_i}\right) + \frac{1 - \rho_p \rho_q}{N} \sum_{i=1}^{N} \cos\left(\psi_{p_i} - \psi_{q_i}\right) \quad (5.9)$$

Alternatively it is possible to use phase, amplitude and coherence as shown in 3.18.

5.3.4 Collaborative filtering

Following the statistical description of the complex interferogram shown in sec. 5.3.1, the InSAR-BM3D collaborative filtering aims to filter separately the real and the imaginary parts of the interferogram. The filtering strategy comprises two steps: basic and final estimates. In the following, two approaches for the basic estimate are investigated: the *Hard Thresholding* as in BM3D [15, 16], and the *Self-Wiener* used in SAR-BM3D [84].

In sec. 5.3.1 the interferogram has been expressed as the sum of its true value Γ_0 and a signal-dependent noise component, further exploded below in real and imaginary parts:

$$\Gamma = \Gamma_0 + n = \Gamma_{0\mathcal{R}} + n_{\mathcal{R}} + j\left(\Gamma_{0\mathcal{I}} + n_I\right) \quad (5.10)$$

The filter applies in the transformed domain, hence the quantities

after the transform are considered:

$$\begin{aligned} T_{\mathcal{R}} &= T_{0\mathcal{R}} + T_{n\mathcal{R}} \\ T_I &= T_{0I} + T_{nI} \end{aligned} \tag{5.11}$$

Our aim is to estimate the true signal: $\hat{T}_{0\mathcal{R}}$ and $\hat{T}_{0\mathcal{I}}$.

5.3.4.1 Basic estimate

Hard thresholding This approach aims to preserve only the most significant contributions in the transform domain, hence a thresholding operator Υ at level $\lambda_{th} \cdot \sigma_n$ is applied, where λ_{th} is set from the user, and σ_n is the noise standard deviation.

$$\hat{T_0} = \Upsilon\left[T_0\right] \tag{5.12}$$

The filter in eq. 5.12 applies separately on the real and imaginary parts. The used transform are the *Biorthogonal wavelet* and the *Haar wavelet*, respectively, for the 2D and 1D directions.

Self-Wiener This approach looks for the optimum linear estimator in the MMSE sense. A preliminary estimate of the true signal, necessary for empirical Wiener filtering, is obtained from the noisy data by locally averaging over the samples of the wavelet sub-bands. In order to have a sufficient number of samples for computing the estimate the undecimated wavelet tranform (UDWT) is used in place of the usual decimated wavelet (DWT). The Self-Wiener filter is then defined as

follows:

$$\hat{T_0} = \max\left(0, \frac{E\left[T^2\right] - \sigma_n^2}{E\left[T^2\right]}\right) \cdot T \tag{5.13}$$

where the statistical mean $E[\cdot]$ is replaced by the average over each of the subbands of the transformed signal, with σ_n^2 denoting the noise variance. The Daubechies-4 wavelet is used for both the 2D and 1D transform.

5.3.4.2 Final estimate

The second step is a *Wiener filter* in the wavelet domain, where the basic estimate $\hat{T_0}$ is used in place of the true signal.

$$\hat{T_0} = \max\left(0, \frac{\hat{T_0^2} - \sigma_n^2}{\hat{T_0^2}}\right) \cdot T \tag{5.14}$$

Here, σ_n^2 is the variance of the noise affecting the filtered component. The *Discrete Cosine Transform* (DCT) and the *Haar wavelet transform* are used for 2D and 1D transforms, respectively.

5.3.5 Noise variance estimation

Even though the algorithm can be used with a fixed noise variance, chosen by the user, it can also adapt to the local noise variance by estimating it locally. By using the model in 5.55.6, after noise decor-

relation, the noise variances on real and imaginary part are equal to:

$$\begin{cases} \sigma^2_{n\mathcal{R}} = \frac{1}{2}A_1^2 A_2^2 \left(1+\rho^2\right) \\ \sigma^2_{n\mathcal{I}} = \frac{1}{2}A_1^2 A_2^2 \left(1-\rho^2\right) \end{cases} \tag{5.15}$$

For each group G of similar blocks, the true amplitude and coherence values are substituted by their Maximum Likelihood estimates. For the coherence, as already shown in section sec. 3.2 in equation 3.2, the ML estimate is equal to:

$$\hat{\rho}_{ML} = |\hat{\gamma}_{ML}| = \frac{\left|\sum_{m=1}^{L} u_1[m] \cdot u_2^*[m]\right|}{\sqrt{\sum_{m=1}^{L} |u_1[m]|^2 \cdot \sum_{m=1}^{L} |u_2[m]|^2}} \tag{5.16}$$

For the amplitude instead, assuming it to be Rayleigh distributed, the ML estimation is:

$$\hat{A}_{ML} = \frac{\sqrt{\pi}}{2}\sqrt{\frac{1}{L}\sum_{m=1}^{L} |u[m]|^2} \tag{5.17}$$

where the subscript m spans the group of cardinality L.

At the second step, for the Wiener filtering, an estimate of the true signal is already available, hence, it is used to estimate the noise variance based on the difference between the noisy quantity and its basic estimate.

5.4 Topography-based similarity measure and filtering

This section introduce a novel criterion for similarity computation and estimation of InSAR parameters. As seen in chapter 3, local stationarity of the interferometric phase is often required in the estimation, and many algorithms have been proposed in order to deal with the phase non-stationarity. When the topography contribution is significant, i.e. the topography has strong spatial variations, it can be compensated, as proposed in [61, 110] to improve coherence estimation, but this needs a previous local estimation of the slope (i.e. fringe frequency) which can introduce further errors and artifacts. The non-local algorithms, have shown to surpass the limit of the local WSS hypothesis, since, by looking for statistically homogeneous pixels in a larger window, they automatically enforce the stationarity hypothesis on the estimation group. An example of this application to the InSAR field has been shown in [20, 22]. Given a similarity measure as the one defined in 5.7, Fig. 5.3 shows a possible selection of blocks (blue squares) that are similar to a target block (red square) for a phase ramp.

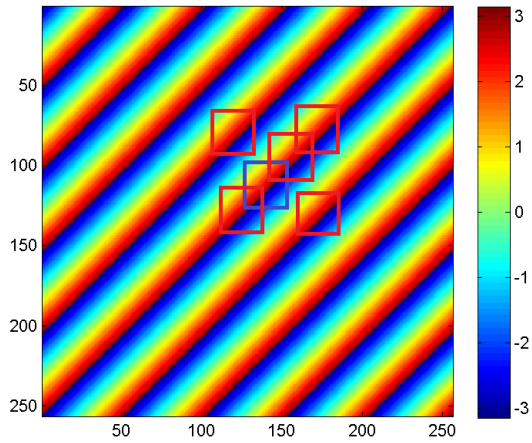

Figure 5.3: Example of nonlocal block selection.

It is worth underlining that the nonlocal algorithm, looking for blocks that are similar to the target, tends to select blocks lying on the very same fringe as the pattern, and may even jump a fringe to find other similar blocks which guarantee the stationarity among the estimation group. As a consequence, since most neighboring blocks lie instead on different fringes, there is a scarcity of good candidates which might eventually impair the estimation quality.

In sec. 2.2.1, it has been already shown that the interferometric phase is always meant as a differential measurement which links a spatial topographic variation to the interferometric phase variation as expressed by formula 2.16. This means that the same information on the topography can be coded by different absolute phase values, provided their spatial variation is the same. For example, for a phase ramp, the constant topography variation is coded with a fringe pattern at constant frequency.

These considerations are at the basis of a modified grouping approach

for nonlocal filtering. In fact, for our phase ramp running example, all blocks surrounding the target would be actually good candidates if one could compensate the absolute phase difference. That is, all such blocks are characterized by the same signal, except for a constant bias, changing from block to block. Once the bias is removed, all of them become similar to the target. In this way, for a phase ramp, any block extracted from the interferogram is a candidate for the filtering. In fact, together with the blocks selected in Fig. 5.3, now also blocks with different phase values can be selected, as shown in Fig. 5.4. Increasing the number of candidates, goes obviously to the benefit of estimation quality. Before turning to the problem of estimating and compensating such bias, it is worth underlining that the phase ramp example is by no means exceptional in interferometric phase filtering. These images have very often a locally linear behavior, that is they can be approximated by a phase ramp, for which the above considerations apply. On the contrary, natural images rarely present constant slope regions.

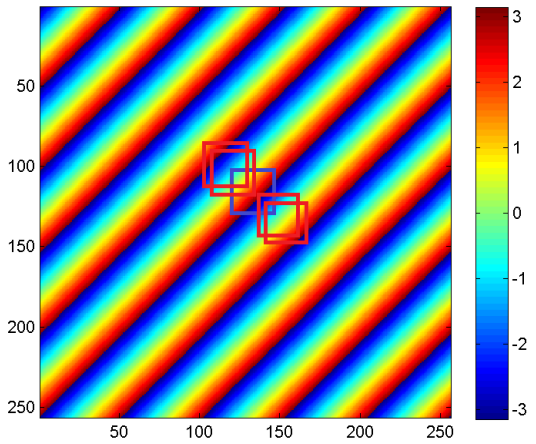

Figure 5.4: Example of nonlocal block selection.

In order to understand whether two blocks share the same topographic structure (or "slope"), no slope or fringe frequency estimator is used. Instead, it is observed that the difference of interferometric phase between blocks with the same topography is constant. If this constant is deleted the phase homogeneity hypothesis is also valid.

A simplified case of 3-pixel blocks is taken as example. The phase values are represented on a polar graph and the correspondence between blocks' pixels is identified by colors and numbers. The case of similar and non similar blocks is shown in Fig. 5.5.

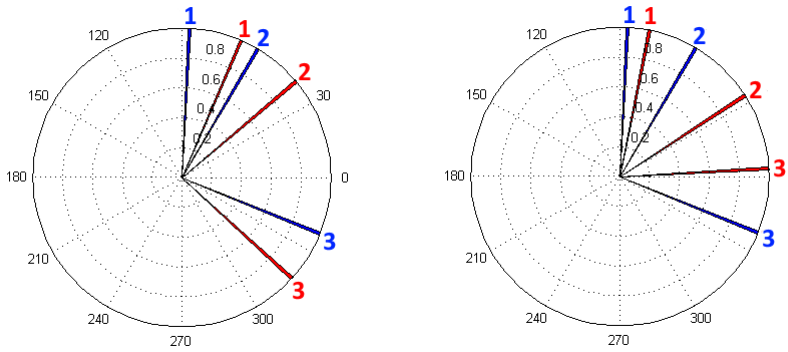

Figure 5.5: Example of similar (a) and non similar (b) blocks.

In order to understand if two blocks are similar, a dissimilarity measure is defined starting from eq. 5.7. In particular, we are interested in the phase offset φ_0 that minimizes such a distance, that is the solution of the following minimization problem:

$$\varphi_0 = \arg\min_{\varphi} \left(1 - \frac{1}{N} \sum_{i=1}^{N} \cos\left(\psi_{p_i} - (\psi_{q_i} + \varphi)\right) \right) \tag{5.18}$$

This results in the new dissimilarity distance and the estimated phase offset:

$$\begin{aligned} D_{\varphi} &= 1 - \left| \tfrac{1}{N} \textstyle\sum_{i=1}^{N} e^{j\left(\psi_{p_i} - \psi_{q_i}\right)} \right| \\ \varphi_0 &= \arg\left(\textstyle\sum_{i=1}^{N} e^{j\left(\psi_{p_i} - \psi_{q_i}\right)} \right) \end{aligned} \tag{5.19}$$

In practice, these are respectively amplitude and argument of the phase correlation between the two interferogram blocks under comparison. The phase offset that is removed during the similarity computation is then reinserted after the phase filtering.

This approach is first tested in a simplified framework: two versions of the Non-Local-Means algorithm are compared using the dissimilarity measures in 5.7 and 5.19, respectively. The case of a phase ramp is taken once again as example of a non-stationary scene. As quality measures the Root Mean-Squared-Error (RMSE) on phase estimations and the visual inspection of the relative error maps are considered. Apart from the improvement in the RMSE, the result in Fig. 5.8 show a better fringe preservation for the algorithm with phase offset compensation. In the next section the topography-based approach is also used in the proposed InSAR-BM3D algorithm.

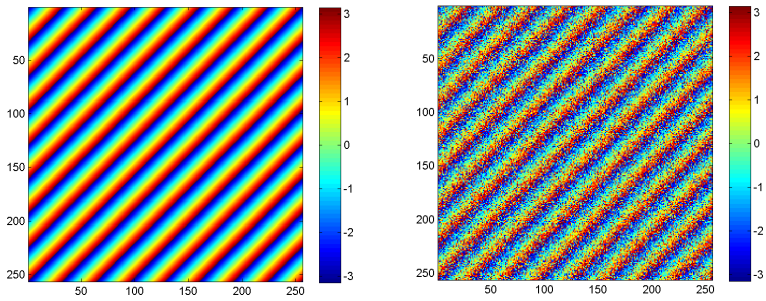

(a) **(b)**

Figure 5.6: True (a) and noisy (b) interferometric phase ramp.

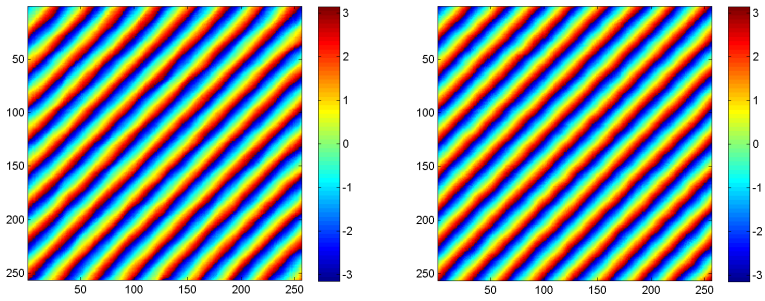

(a) **(b)**

Figure 5.7: Estimated phase with (a) and without (b) phase offset compensation.

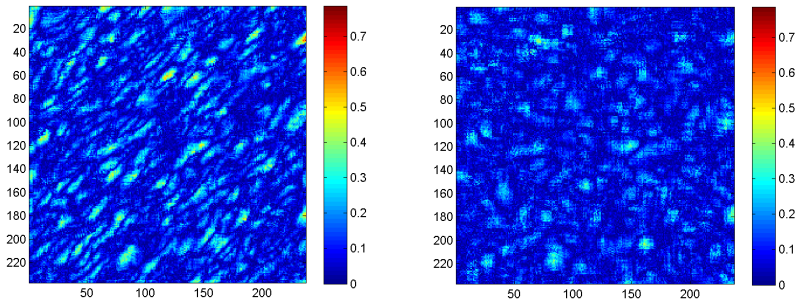

Figure 5.8: Error map on the estimated phase with (a) and without (b) phase offset compensation. RMSE: (a) 0.14 (b) 0.10.

5.5 Experimental results on simulated data

For performance assessment, preliminary experiments have been carried out on simulated data. The aim is to study in a controlled environment the behaviour of the proposed filters in comparison with the state-of-the-art filters. The simulated dataset is formed by setting the underlying amplitude and coherence to a constant value and considering a variable phase structure: a 256x256 *Peaks* function, a 256x256 phase *Ramp* and two 512x512 interferograms generated from natural images, *House* and *Peppers*. The noiseless interferograms are shown in Fig. 5.9.

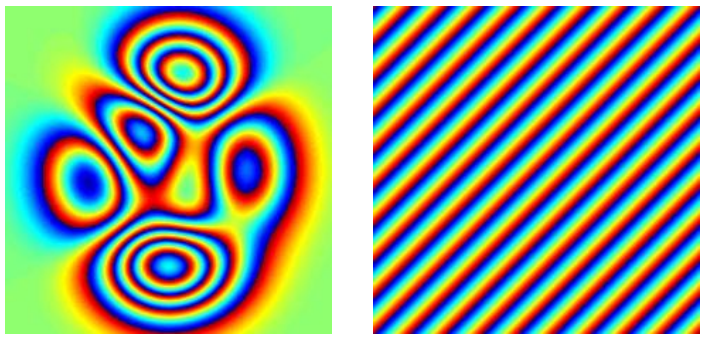

(a) *Peaks* **(b)** *Ramp*

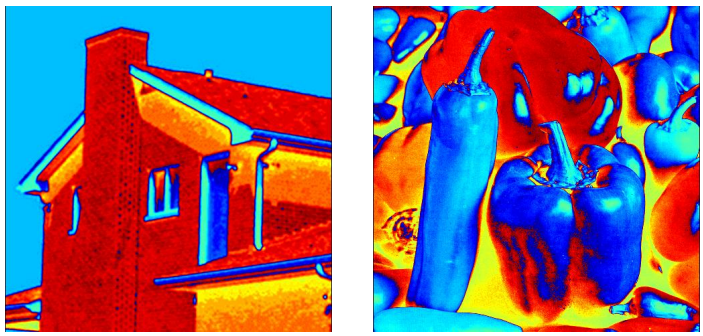

(c) *House* **(d)** *Peppers*

Figure 5.9: Noiseless simulated interferometric phase dataset.

The data are simulated by generating two circular complex standard gaussian processes and correlating them through the matrix L in eq. 5.5, that is the Cholesky decomposition of the desired covariance matrix.

The first two examples in Fig. 5.9 (a)(b) simulate common situations in real operations in which the topography creates phase variations and fringes. More specifically, in (a) a variation of topography it is simulated similar to that occurring in a mountain area and in (b) a constant topography that generates a phase ramp. The other two

examples, instead, can be associated to very small baseline interferograms that are usually not used given their low accuracy on the topography (as described in sec. 2.2.2). However, they are used in the literature [20, 22] and hence we consider them for comparison pourposes.

The proposed algorithm is compared with the NLSAR [22] and NLInSAR [20] filters. Furthermore four different version of the InSAR-BM3D are considered: the version with Hard-Threshold (indicated in short as "HT"), with the Self-Wiener (indicated as "SelfW") and their respective versions with phase offset compensation "HToffset" and "SelfWoffset". All the algorithms share the same nonlocal parameters as search window, set to 21×21 and patch size 8×8. In the proposed algorithms groups of 64 similar blocks are formed in both steps for the first two examples and groups of 32 blocks, again in both steps, for the last two examples.

For each example, the Root Mean-Square-Error (RMSE) is estimated over 10 iterations and the filtered interferograms and the relative error maps are compared by visual inspection.

	Peaks		*Ramp*	
	1st st.	2nd st.	1st st.	2nd st.
NLSAR [22]	/	8285 (82)	/	9087 (141)
NLInSAR [20]	/	1621 (100)	/	1438 (26)
HT	1573 (51)	1443 (53)	1408 (28)	1256 (21)
SelfW	1611 (38)	1441 (41)	1574 (17)	1360 (16)
HToffset	1165 (30)	1048 (32)	1113 (27)	862 (20)
SelfWoffset	1208 (28)	1078 (30)	1141 (18)	881 (19)

Table 5.1: Root-Mean-Square-Error (×10000). In paretheses the st. dev. (×10000).

The RMSE comparison in Tab. 5.1 for the first two examples shows a better performance for HT and SelfW algorithms with respect to the state-of-the-art filters NLSAR and NLInSAR. This result is also confirmed from the visual inspection of Fig. 5.10Fig. 5.11Fig. 5.12Fig. 5.13, where the fringes are better reconstructed. Still better performances are achieved if the phase offset compensation is used. This can be explained with the fact that looking for blocks having a similar topography content instead of just a similar phase can increase the level of similarity between the grouped blocks. The phase offset compensation can improve the filtering especially for rare blocks like an edge on a circular fringe as in the *Peaks* interferogram. This result can be appreciated in the error maps in Fig. 5.11 and Fig. 5.13: the error in (a,b,c,e) follows the fringe shape, while the algorithms that exploit the phase offset compensation (g,f) have a flatter error.

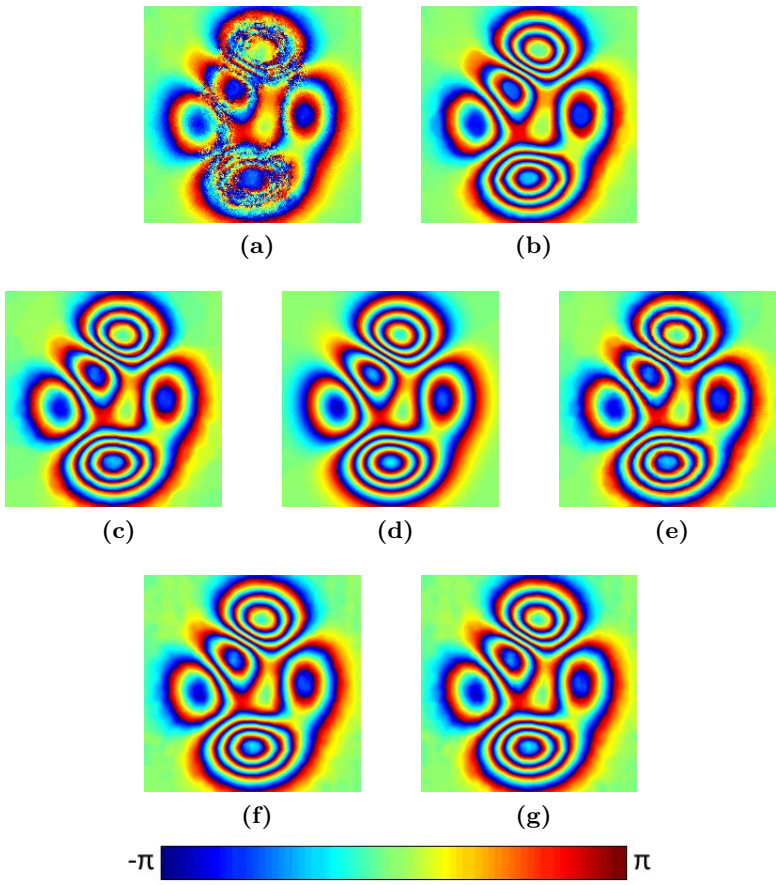

Figure 5.10: Filtered interferometric phase for *Peaks* with the algorithms: NLSAR (a), NLInSAR (b), HT (c), SelfW (e), HToffset (f), SelfWoffset (g). The central image indicates the true interferometric phase (d).

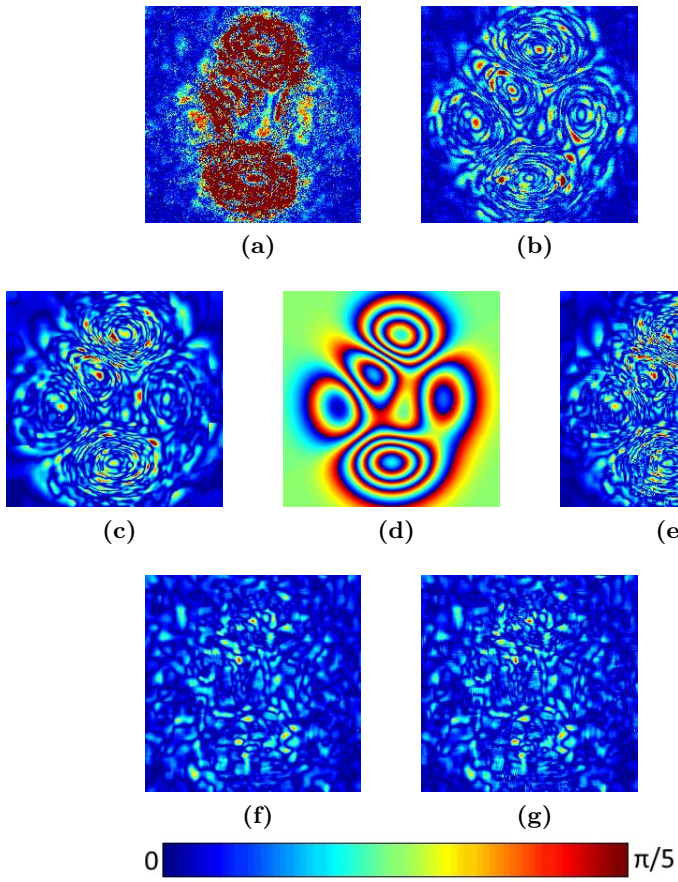

Figure 5.11: Error map for *Peaks* relative to the algorithms: NLSAR (a), NLInSAR (b), HT (c), SelfW (e), HToffset (f), SelfWoffset (g). The central image indicates the true interferometric phase (d).

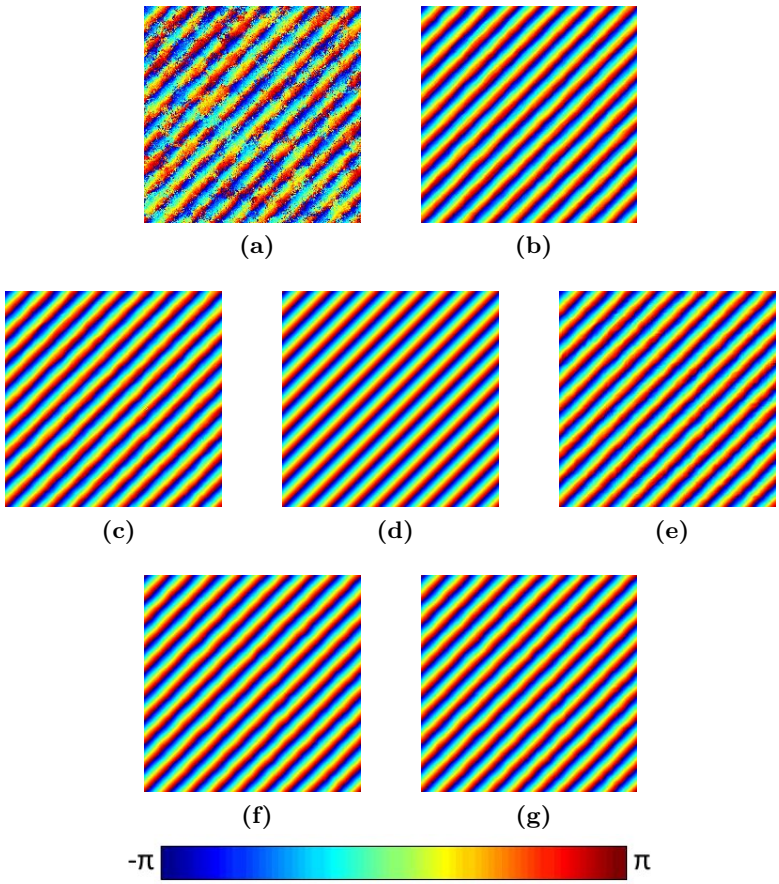

Figure 5.12: Filtered interferometric phase for *Ramp* with the algorithms: NLSAR (a), NLInSAR (b), HT (c), SelfW (e), HToffset (f), SelfWoffset (g). The central image indicates the true interferometric phase (d).

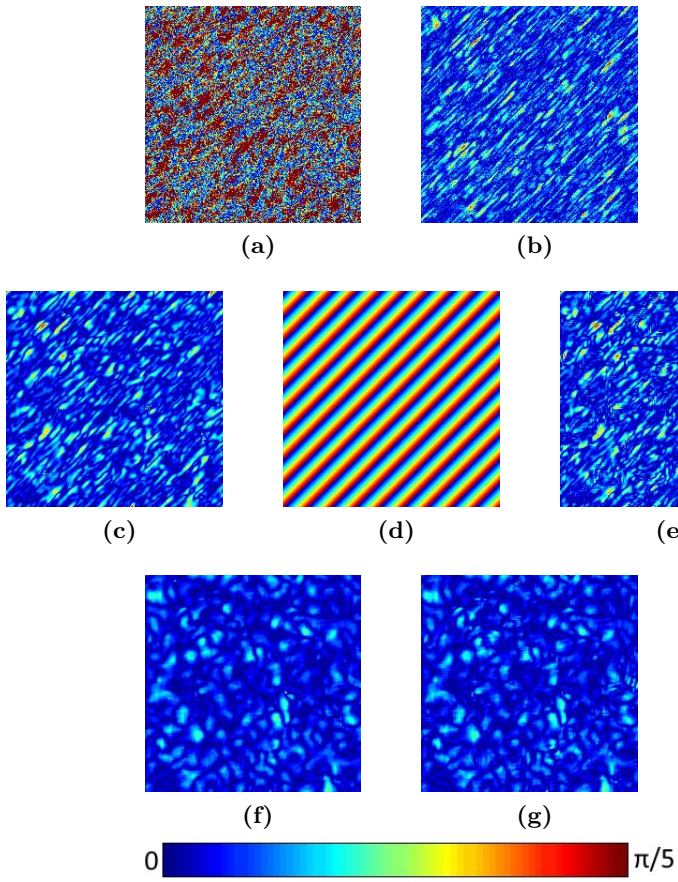

Figure 5.13: Error map for *Ramp* relative to the algorithms: NLSAR (a), NLInSAR (b), HT (c), SelfW (e), HToffset (f), SelfWoffset (g). The central image indicates the true interferometric phase (d).

Similar results can be appreciated for the last two examples where the phase offset compensation is not needed given the flatness of the interferograms. For this kind of data, NLInSAR is known to have a tendency to create a staircase effect in the, also recently investigated in interferometric phase filtering.

	House		*Peppers*	
	1st st.	2nd st.	1st st.	2nd st.
NLSAR [22]	/	3140 (21)	/	4012 (29)
NLInSAR [20]	/	1649 (25)	/	2671 (24)
HT	1545 (17)	1339 (7)	2439 (21)	2244 (13)
SelfW	1444 (10)	1307 (7)	2262 (11)	2176 (11)

Table 5.2: Root-Mean-Square-Error (×10000). In paretheses the st. dev. (×10000).

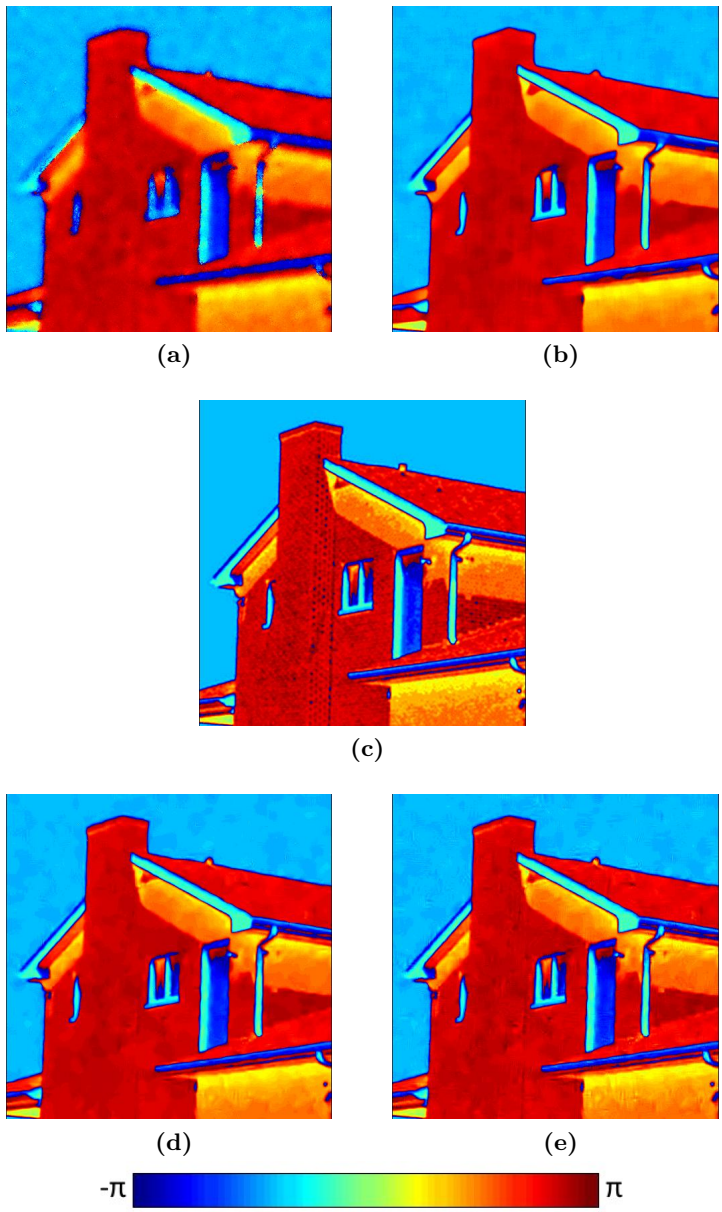

Figure 5.14: Filtered interferometric phase for *House* with the algorithms: NLSAR (a), NLInSAR (b), HT (d), SelfW (e). The central image indicates the true interferometric phase (c).

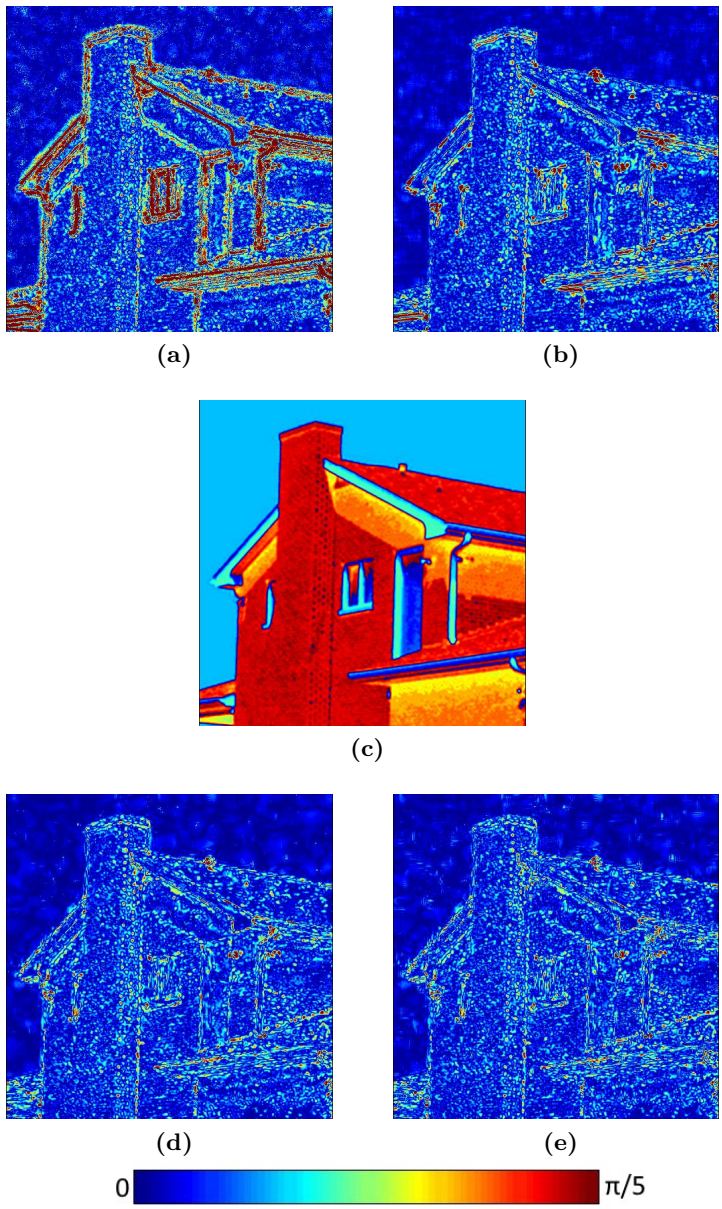

Figure 5.15: Error map for *House* relative to the algorithms: NLSAR (a), NLInSAR (b), HT (d), SelfW (e). The central image indicates the true interferometric phase (c).

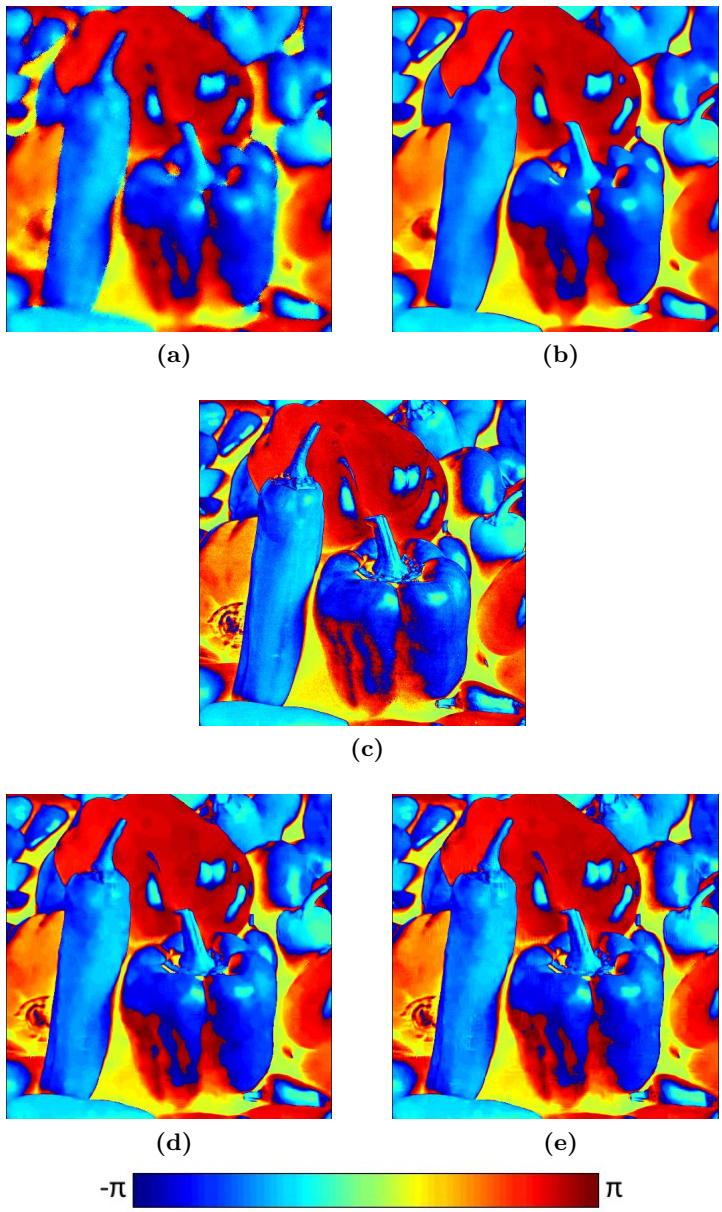

Figure 5.16: Filtered interferometric phase for *Peppers* with the algorithms: NLSAR (a), NLInSAR (b), HT (d), SelfW (e). The central image indicates the true interferometric phase (c).

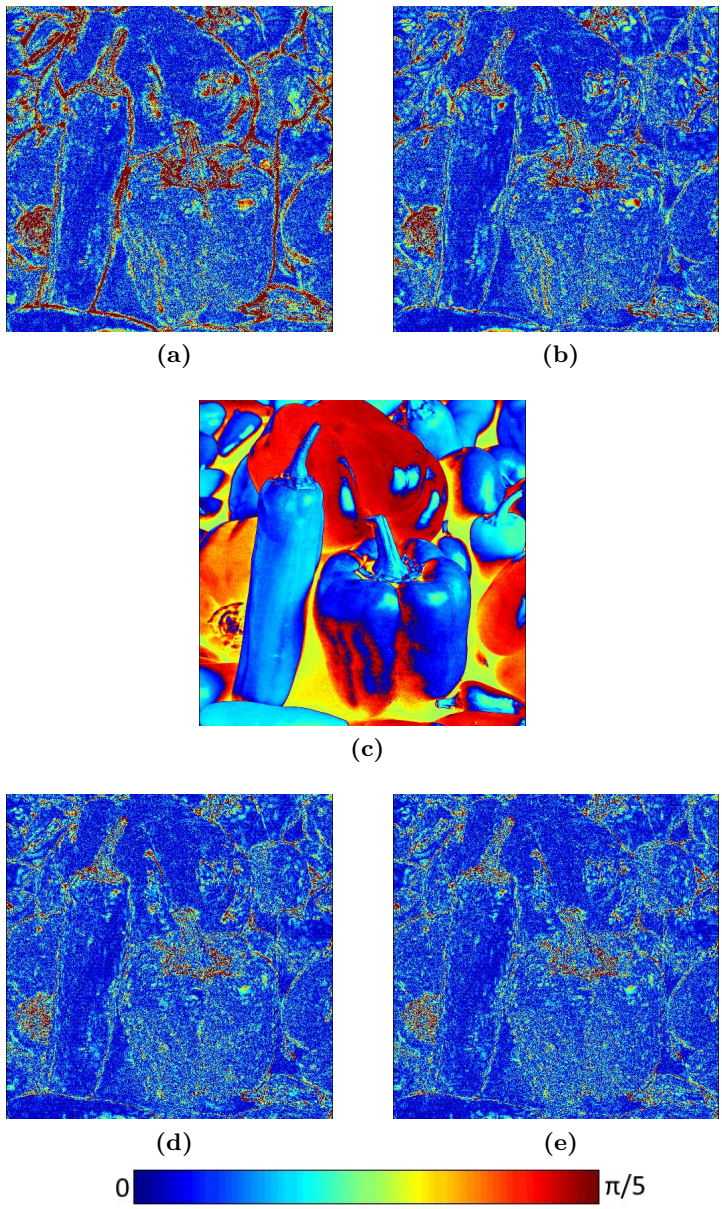

Figure 5.17: Error map for *Peppers* relative to the algorithms: NL-SAR (a), NLInSAR (b), HT (d), SelfW (e). The central image indicates the true interferometric phase (c).

5.6 Experimental results on real data

For the assessment of the performances on a real-world SAR image, a dataset of 4 Tandem-X pairs has been considered. The NLInSAR is compared with the InSAR-BM3D HT algorithm and a 3×3 boxcar filtering is taken as a reference of the true underlying signal.

By comparing the InSAR-BM3D with the reference boxcar filter, the algorithm shows to preserve more details with respect to the NLInSAR algorithm that, instead, tends to smooth the signal and create large flat areas, as it can be noticed from the crop in Fig. 5.22. On the other hand the InSAR-BM3D tends to filter less the areas where the SLC's amplitude is very large. This behavior is due to the fact that few large amplitude values in the group average may push the coherence towards 1, and this results in a underestimation of the noise variance with a consequent underfiltering. An example of this behavior is shown in the crop of Fig. 5.23. Given that the SAR amplitude has a wide dynamic range it is very likely to find this behavior in the filterd interferogram and hence it should be corrected by compensating the noise variance estimation with corrective terms. This problem is similar to the underfiltering that happen for the NLInSAR and NLSAR in the case of rare patches and that is resolved by fixing a desired minimum amount of looks.

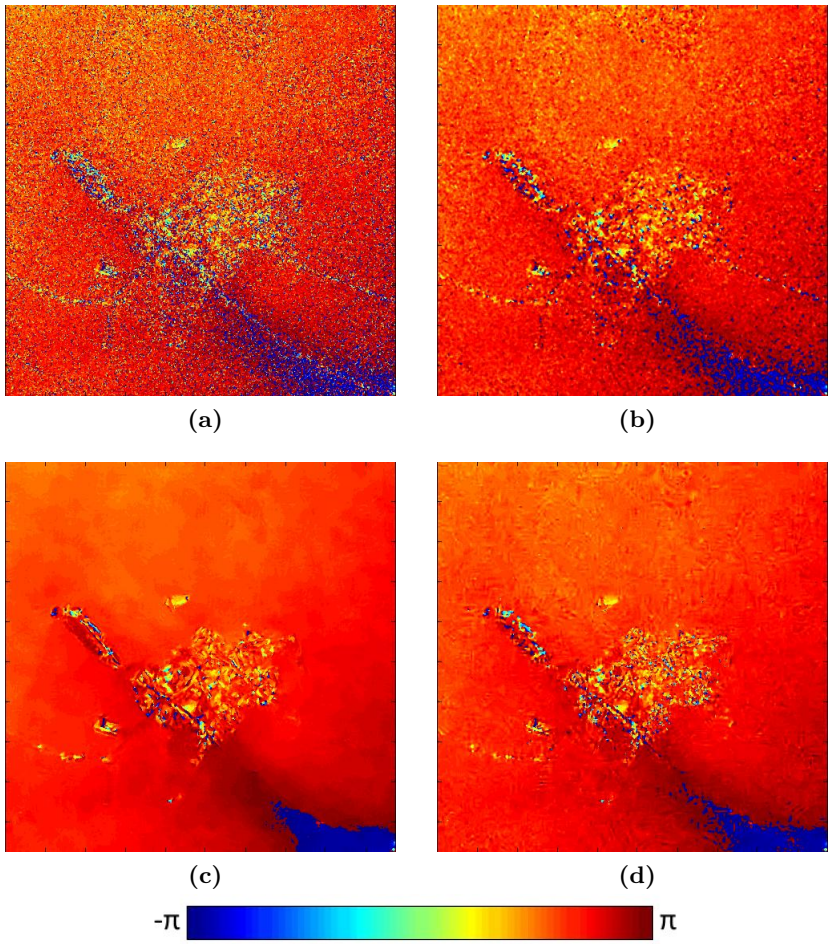

Figure 5.18: Tandem-X data relative to the city of *Euskirchen*. Noisy (a), Boxcar 3×3 (b), NLInSAR (c) and InSAR-BM3D HT (d)

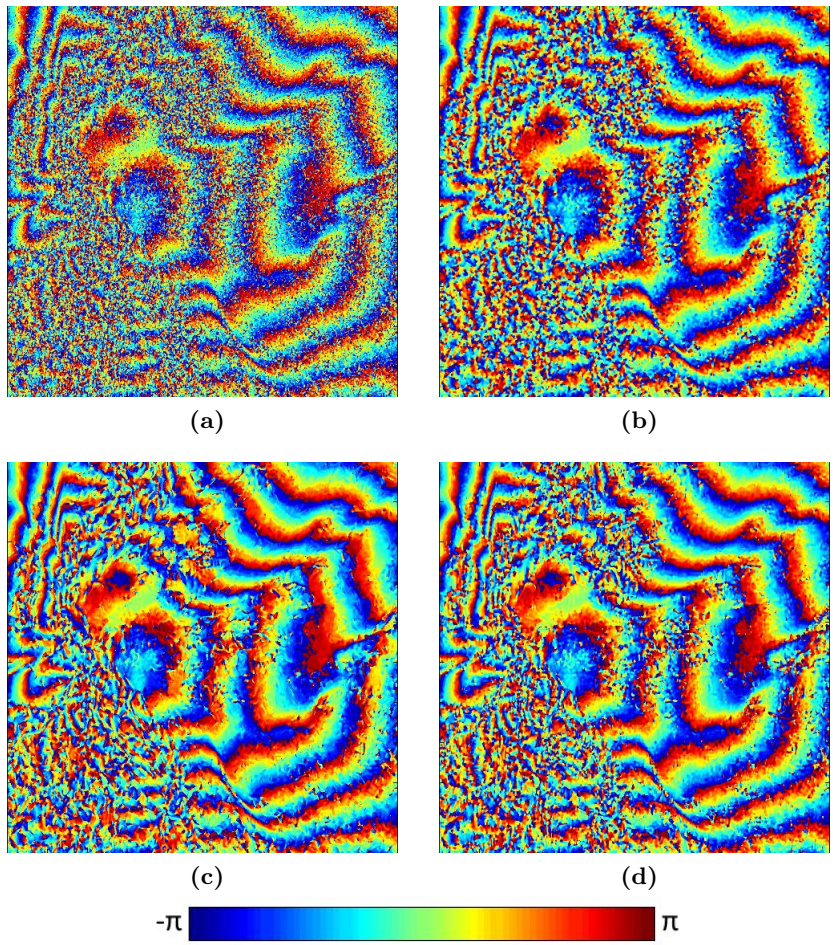

Figure 5.19: Tandem-X data relative to the city of *Java Surabaya*. Noisy (a), Boxcar 3×3 (b), NLInSAR (c) and InSAR-BM3D HT (d)

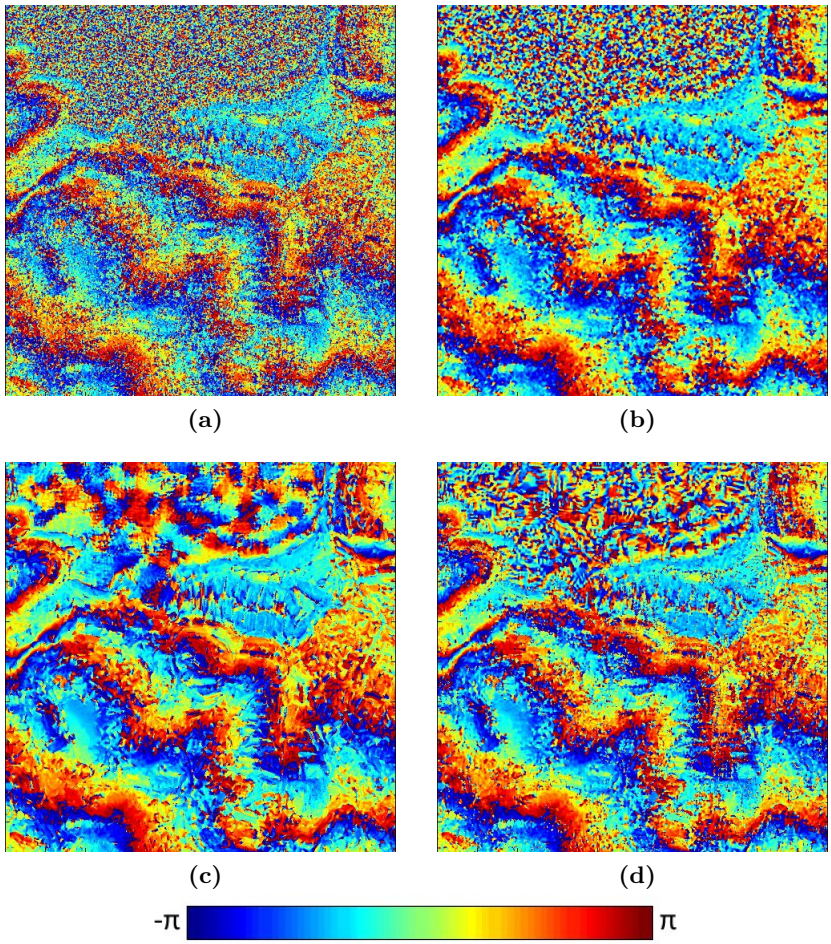

Figure 5.20: Tandem-X data relative to the city of *Marseille*. Noisy (a), Boxcar 3×3 (b), NLInSAR (c) and InSAR-BM3D HT (d)

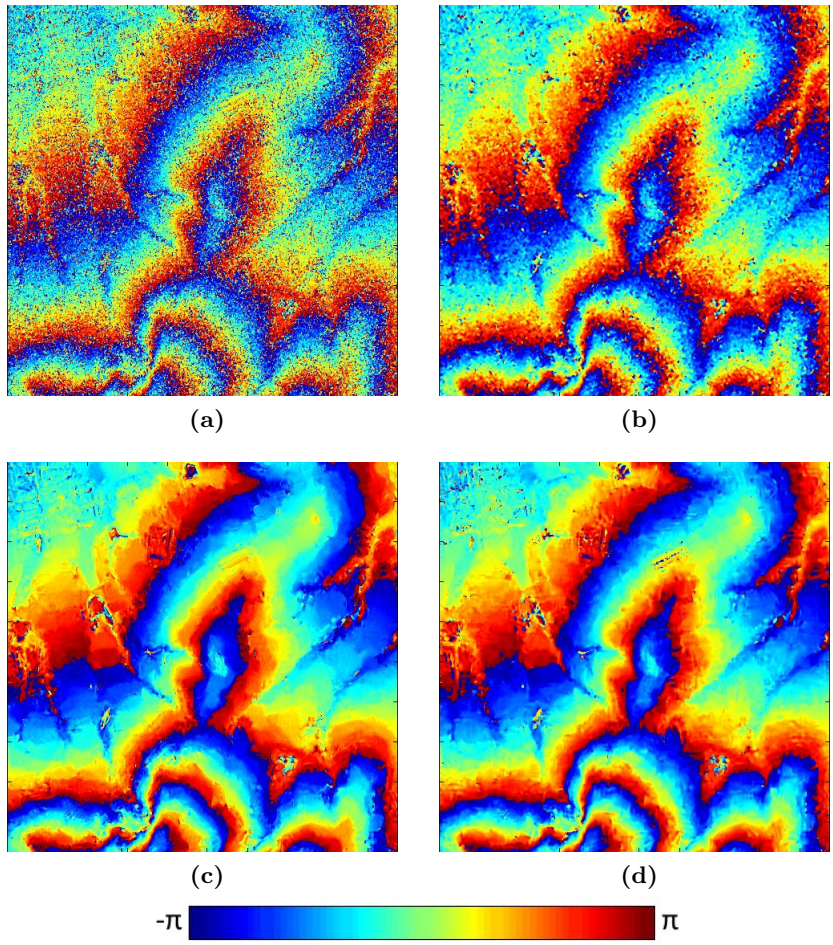

Figure 5.21: Tandem-X data relative to the city of *Weihai*. Noisy (a), Boxcar 3×3 (b), NLInSAR (c) and InSAR-BM3D HT (d)

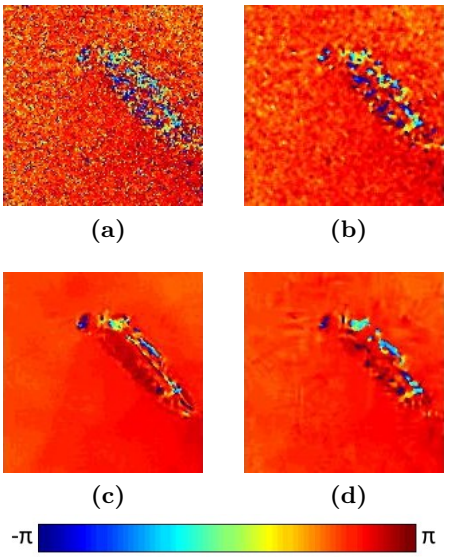

Figure 5.22: Crop from the *Euskirchen* data. Noisy (a), Boxcar 3×3 (b), NLInSAR (c) and InSAR-BM3D HT (d).

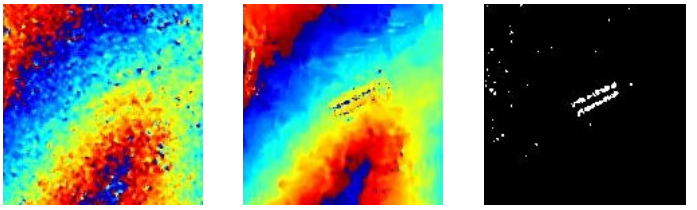

Figure 5.23: Crop from the *Weihai* data. Boxcar 3×3 (a), InSAR-BM3D HT (b) and threshold on amplitude values (c).

6 Conclusion

The thesis work has investigated the use of nonlocal approaches for InSAR parameter estimation in single-pass and multi-pass Interferometry. Thanks to modern SAR imaging systems, multitemporal applications are today possible over a long time span and at very-high resolution. The classical approach to multipass processing is a low-resolution analysis in which all generated interferogram are multilooked and subsampled in order to extract a reliable low-resolution information on the area of interest. This is the case, for example, of Differential Interferometry used to manage emergency situations, where data resolution is often traded off with processing time in order to make results quickly available. When high-resolution analysis is required, however, temporal information can be exploited through nonlocal processing tools in order to improve InSAR parameter estimation with no loss of resolution. In the present thesis work, Adaptive Multilooking has been investigated in the framework of the Small BAseline Subset (SBAS) processing chain. Two similarity measures have been compared, as well as various pre-filtering procedures, in order to improve the pixel similarity computation. The results have been first evaluated on simulated data and then on low- and high-resolution real data: ENVISAT and COSMO-SkyMED. The work has shown that the temporal information can be successfully exploited at this aim, and that a similarity measure specifically designed on speckle statistic can further improve the estimation.

In single-pass applications, aiming at interferometric phase estimation, one can rely on the interferogram spatial information as already shown in [20, 22]. In this thesis work, it has been shown that combining the nonlocal criteria with more complex filtering methods, as transform-domain shrinkage, further improvements can be obtained in InSAR phase estimation. The nonlocal approach suits well the characteristic of the interferometric signal given its redundancy and self-similarity. By exploiting this property, large groups of similar blocks can be created in order to achieve a sparser representation of the signal in the transformed domain. An interferometric phase filter, called InSARBM3D, is proposed and multiple solutions for transform domain filtering are investigated. The algorithm is tested on simulated and on TANDEM-X real data.

In the nonlocal context a filtering criterion based on the relative-topography content of the interferometric phase is developed in order to further improve the phase estimation. The criterion starts from noticing that two interferogram blocks can bring the same information on the topography while having a phase offset. By looking for topographic similarity, rather than phase similarity, the filtering can be further improved since more similar and less noisy blocks can be found in the search window. The validity of this approach is first investigated in the simplified context of the Non-Local-Means algorithm to show its basic behavior and then it is merged in the proposed InSARBM3D algorithm. It is shown experimentally that the proposed method can improve results significantly.

Bibliography

[1] Alberto Alonso-González, Carlos López-Martínez, Philippe Salembier, and Xinping Deng. Bilateral distance based filtering for polarimetric sar data. *Remote Sensing*, 5(11):5620–5641, 2013.

[2] Fabrizio Argenti and Luciano Alparone. Speckle removal from sar images in the undecimated wavelet domain. *Geoscience and Remote Sensing, IEEE Transactions on*, 40(11):2363–2374, 2002.

[3] Richard Bamler and Philipp Hartl. Synthetic aperture radar interferometry. *Inverse problems*, 14(4):R1, 1998.

[4] Ireneusz Baran, Mike P Stewart, Bert M Kampes, Zbigniew Perski, and Peter Lilly. A modification to the goldstein radar interferogram filter. *IEEE Transactions on Geoscience and Remote Sensing*, 41(9):2114–2118, 2003.

[5] Paolo Berardino, Gianfranco Fornaro, Riccardo Lanari, and Eugenio Sansosti. A new algorithm for surface deformation monitoring based on small baseline differential sar interferograms. *Geoscience and Remote Sensing, IEEE Transactions on*, 40(11):2375–2383, 2002.

[6] Lorenzo Bruzzone, Mattia Marconcini, Urs Wegmüller, and Andreas Wiesmann. An advanced system for the automatic clas-

sification of multitemporal sar images. *Geoscience and Remote Sensing, IEEE Transactions on*, 42(6):1321–1334, 2004.

[7] Antoni Buades, Bartomeu Coll, and Jean-Michel Morel. A review of image denoising algorithms, with a new one. *Multiscale Modeling & Simulation*, 4(2):490–530, 2005.

[8] Antoni Buades, Bartomeu Coll, and Jean-Michel Morel. The staircasing effect in neighborhood filters and its solution. *IEEE transactions on Image Processing*, 15(6):1499–1505, 2006.

[9] Priyam Chatterjee and Peyman Milanfar. Patch-based near-optimal image denoising. *Image Processing, IEEE Transactions on*, 21(4):1635–1649, 2012.

[10] Jiong Chen, Yilun Chen, Wentao An, Yi Cui, and Jian Yang. Nonlocal filtering for polarimetric sar data: A pretest approach. *Geoscience and Remote Sensing, IEEE Transactions on*, 49(5):1744–1754, 2011.

[11] Mihai Ciuc, Philippe Bolon, Emmanuel Trouvé, Vasile Buzuloiu, and Jean-Paul Rudant. Adaptive-neighborhood speckle removal in multitemporal synthetic aperture radar images. *Applied Optics*, 40(32):5954–5966, 2001.

[12] Mauro Coltelli, Gianfranco Fornaro, Giorgio Franceschetti, Riccardo Lanari, Maurizio Migliaccio, João R Moreira, Konstantinos P Papathanassiou, Giuseppe Puglisi, Daniele Riccio, and Marcus Schwäbisch. Sir-c/x-sar multifrequency multipass interferometry: A new tool for geological interpretation. *Journal of Geophysical Research: Planets (1991–2012)*, 101(E10):23127–23148, 1996.

[13] Davide Cozzolino, Sara Parrilli, Giuseppe Scarpa, Giovanni Poggi, and Luisa Verdoliva. Fast adaptive nonlocal sar despeck-

ling. *Geoscience and Remote Sensing Letters, IEEE*, 11(2):524–528, 2014.

[14] J. C. Curlander and R. N. Mc Donough. Synthetic aperture radar - systems and signal processing. *Wiley Series in Remote Sensing & Image Processing*, 1991.

[15] Kostadin Dabov, Alessandro Foi, Vladimir Katkovnik, and Karen Egiazarian. Color image denoising via sparse 3d collaborative filtering with grouping constraint in luminance-chrominance space. In *Image Processing, 2007. ICIP 2007. IEEE International Conference on*, volume 1, pages I–313. IEEE, 2007.

[16] Kostadin Dabov, Alessandro Foi, Vladimir Katkovnik, and Karen Egiazarian. Image denoising by sparse 3-d transform-domain collaborative filtering. *Image Processing, IEEE Transactions on*, 16(8):2080–2095, 2007.

[17] C. A. Deledalle, L. Denis, and F. Tupin. How to compare noisy patches? patch similarity beyond gaussian noise. *International Journal of Computer Vision*, 99(1):86–102, 2012.

[18] Charles-Alban Deledalle, Loic Denis, Giovanni Poggi, Florence Tupin, and Luisa Verdoliva. Exploiting patch similarity for sar image processing: the nonlocal paradigm. *Signal Processing Magazine, IEEE*, 31(4):69–78, 2014.

[19] Charles-Alban Deledalle, Loïc Denis, and Florence Tupin. Iterative weighted maximum likelihood denoising with probabilistic patch-based weights. *Image Processing, IEEE Transactions on*, 18(12):2661–2672, 2009.

[20] Charles-Alban Deledalle, Loïc Denis, and Florence Tupin. Nl-

insar: Nonlocal interferogram estimation. *Geoscience and Remote Sensing, IEEE Transactions on*, 49(4):1441–1452, 2011.

[21] Charles-Alban Deledalle, Loıc Denis, Florence Tupin, Andreas Reigber, and Marc Jäger. Additional illustrations of nl-sar method for resolution-preserving (pol)(in) sar denoising, 2014.

[22] Charles-Alban Deledalle, Loïc Denis, Florence Tupin, Andreas Reigber, and Marc Jašger. Nl-sar: A unified nonlocal framework for resolution-preserving (pol)(in) sar denoising. *Geoscience and Remote Sensing, IEEE Transactions on*, 53(4):2021–2038, 2015.

[23] Charles-Alban Deledalle, Florence Tupin, and Loïc Denis. Patch similarity under non gaussian noise. In *Image Processing (ICIP), 2011 18th IEEE International Conference on*, pages 1845–1848. IEEE, 2011.

[24] Gerardo Di Martino, Mariana Poderico, Giovanni Poggi, Daniele Riccio, and Luisa Verdoliva. Benchmarking framework for sar despeckling. *Geoscience and Remote Sensing, IEEE Transactions on*, 52(3):1596–1615, 2014.

[25] David L Donoho. Denoising by soft-thresholding," dept. of statistics, 1992.

[26] Angela Errico, Cesario Vincenzo Angelino, Luca Cicala, Giuseppe Persechino, Claudia Ferrara, Massimiliano Lega, Andrea Vallario, Claudio Parente, Giuseppe Masi, Raffaele Gaetano, et al. Detection of environmental hazards through the feature-based fusion of optical and sar data: a case study in southern italy. *International Journal of Remote Sensing*, 36(13):3345–3367, 2015.

[27] A. Ferretti, C. Prati, and F. Rocca. An overview of sar interferometry. *ESA workshop*, 1997.

[28] Alessandro Ferretti, Alfio Fumagalli, Fabrizio Novali, Claudio Prati, Fabio Rocca, and Alessio Rucci. A new algorithm for processing interferometric data-stacks: Squeesar. *Geoscience and Remote Sensing, IEEE Transactions on*, 49(9):3460–3470, 2011.

[29] Alessandro Ferretti, Claudio Prati, and Fabio Rocca. Nonlinear subsidence rate estimation using permanent scatterers in differential sar interferometry. *Geoscience and Remote Sensing, IEEE transactions on*, 38(5):2202–2212, 2000.

[30] Alessandro Ferretti, Claudio Prati, and Fabio Rocca. Permanent scatterers in sar interferometry. *Geoscience and Remote Sensing, IEEE Transactions on*, 39(1):8–20, 2001.

[31] G Fornaro and V Pascazio. Sar interferometry and tomography: Theory and applications. *Communications and Radar Signal Processing*, 2, 2013.

[32] G Fornaro, A Pauciullo, and F Serafino. Deformation monitoring over large areas with multipass differential sar interferometry: a new approach based on the use of spatial differences. *International Journal of Remote Sensing*, 30(6):1455–1478, 2009.

[33] Gianfranco Fornaro, Fabrizio Lombardini, Antonio Pauciullo, Diego Reale, and Federico Viviani. Tomographic processing of interferometric sar data: Developments, applications, and future research perspectives. *Signal Processing Magazine, IEEE*, 31(4):41–50, 2014.

[34] Gianfranco Fornaro, Antonio Pauciullo, and Diego Reale. A null-space method for the phase unwrapping of multitemporal sar interferometric stacks. *Geoscience and Remote Sensing, IEEE Transactions on*, 49(6):2323–2334, 2011.

[35] Gianfranco Fornaro, Antonio Pauciullo, Diego Reale, and Simona Verde. Multilook sar tomography for 3-d reconstruction and monitoring of single structures applied to cosmo-skymed data. *Selected Topics in Applied Earth Observations and Remote Sensing, IEEE Journal of*, 7(7):2776–2785, 2014.

[36] Gianfranco Fornaro, Diego Reale, and Francesco Serafino. Four-dimensional sar imaging for height estimation and monitoring of single and double scatterers. *Geoscience and Remote Sensing, IEEE Transactions on*, 47(1):224–237, 2009.

[37] Gianfranco Fornaro, Simona Verde, Diego Reale, and Antonio Pauciullo. Caesar: An approach based on covariance matrix decomposition to improve multibaseline–multitemporal interferometric sar processing. *Geoscience and Remote Sensing, IEEE Transactions on*, 53(4):2050–2065, 2015.

[38] Giorgio Franceschetti, Vito Pascazio, and Gilda Schirinzi. Iterative homomorphic technique for speckle reduction in synthetic-aperture radar imaging. *JOSA A*, 12(4):686–694, 1995.

[39] Victor S Frost, Josephine Abbott Stiles, K Sam Shanmugan, and Julian C Holtzman. A model for radar images and its application to adaptive digital filtering of multiplicative noise. *Pattern Analysis and Machine Intelligence, IEEE Transactions on*, (2):157–166, 1982.

[40] Sihua Fu, Xuejun Long, Xia Yang, and Qifeng Yu. Directionally adaptive filter for synthetic aperture radar interferometric phase images. *Geoscience and Remote Sensing, IEEE Transactions on*, 51(1):552–559, 2013.

[41] R. Gaetano, G. Masi, G. Poggi, L. Verdoliva, and G. Scarpa. Marker-controlled watershed-based segmentation of multireso-

lution remote sensing images. *IEEE Transactions on Geoscience and Remote Sensing*, 53(6):2987–3004, June 2015.

[42] R. Gaetano, G. Masi, G. Scarpa, and G. Poggi. A marker-controlled watershed segmentation: Edge, mark and fill. In *Geoscience and Remote Sensing Symposium (IGARSS), 2012 IEEE International*, pages 4315–4318, July 2012.

[43] Raffaele Gaetano, Donato Amitrano, Giuseppe Masi, Giovanni Poggi, Giuseppe Ruello, Luisa Verdoliva, and Giuseppe Scarpa. Exploration of multitemporal cosmo-skymed data via interactive tree-structured mrf segmentation. *Selected Topics in Applied Earth Observations and Remote Sensing, IEEE Journal of*, 7(7):2763–2775, 2014.

[44] Fabio Gatelli, A Monti Guamieri, Francesco Parizzi, Paolo Pasquali, Claudio Prati, and Fabio Rocca. The wavenumber shift in sar interferometry. *Geoscience and Remote Sensing, IEEE Transactions on*, 32(4):855–865, 1994.

[45] Sandeep P Ghael, Akbar M Sayeed, and Richard G Baraniuk. Improved wavelet denoising via empirical wiener filtering. In *Optical Science, Engineering and Instrumentation'97*, pages 389–399. International Society for Optics and Photonics, 1997.

[46] Dennis C Ghiglia and Mark D Pritt. *Two-dimensional phase unwrapping: theory, algorithms, and software*, volume 4. Wiley New York:, 1998.

[47] D Gnanadurai and V Sadasivam. Undecimated wavelet based speckle reduction for sar images. *Pattern Recognition Letters*, 26(6):793–800, 2005.

[48] Kanika Goel and Nico Adam. An advanced algorithm for de-

formation estimation in non-urban areas. *ISPRS Journal of Photogrammetry and Remote Sensing*, 73:100–110, 2012.

[49] Richard M Goldstein and Charles L Werner. Radar interferogram filtering for geophysical applications. *Geophysical Research Letters*, 25(21):4035–4038, 1998.

[50] Joseph W Goodman. Some fundamental properties of speckle. *JOSA*, 66(11):1145–1150, 1976.

[51] JW Goodman. Statistical optics. 1985. *Willey, New York*, 1988.

[52] Leroy C Graham. Synthetic interferometer radar for topographic mapping. *Proceedings of the IEEE*, 62(6):763–768, 1974.

[53] Haitao Guo, Jan E Odegard, Markus Lang, Ramesh A Gopinath, Ivan W Selesnick, and C Sidney Burrus. Wavelet based speckle reduction with application to sar based atd/r. In *Image Processing, 1994. Proceedings. ICIP-94., IEEE International Conference*, volume 1, pages 75–79. IEEE, 1994.

[54] Ramon Hanssen[1], Alessandro Ferretti, Marco Bianchi, Rossen Grebenitcharsky[1], Frank Kleijer[1], and Ayman Elawar[1]. Atmospheric phase screen (aps) estimation and modeling for radar interferometry. 2005.

[55] Lorenzo Iannini and A Monti Guarnieri. Atmospheric phase screen in ground-based radar: Statistics and compensation. *Geoscience and Remote Sensing Letters, IEEE*, 8(3):537–541, 2011.

[56] Mi Jiang, Xiaoli Ding, and Zhiwei Li. Hybrid approach for unbiased coherence estimation for multitemporal insar. *Geoscience and Remote Sensing, IEEE Transactions on*, 52(5):2459–2473, 2014.

[57] Mi Jiang, Xiaoli Ding, Zhiwei Li, Xin Tian, Wu Zhu, Chisheng Wang, and Bing Xu. The improvement for baran phase filter derived from unbiased insar coherence. *Selected Topics in Applied Earth Observations and Remote Sensing, IEEE Journal of*, 7(7):3002–3010, 2014.

[58] Marian Kazubek. Wavelet domain image denoising by thresholding and wiener filtering. *Signal Processing Letters, IEEE*, 10(11):324–326, 2003.

[59] Darwin T Kuan, Alexander A Sawchuk, Timothy C Strand, and Pierre Chavel. Adaptive noise smoothing filter for images with signal-dependent noise. *Pattern Analysis and Machine Intelligence, IEEE Transactions on*, (2):165–177, 1985.

[60] Riccardo Lanari, Gianfranco Fornaro, Daniele Riccio, Maurizio Migliaccio, Konstantinos P Papathanassiou, João R Moreira, Marcus Schwabisch, Luciano Dutra, Giuseppe Puglisi, Giorgio Franceschetti, et al. Generation of digital elevation models by using sir-c/x-sar multifrequency two-pass interferometry: the etna case study. *Geoscience and Remote Sensing, IEEE Transactions on*, 34(5):1097–1114, 1996.

[61] Hoonyol Lee and Jian Guo Liu. Topographic phase corrected coherence estimation using multi-pass differential sar interferometry: differential coherence. In *Geoscience and Remote Sensing Symposium, 2000. Proceedings. IGARSS 2000. IEEE 2000 International*, volume 2, pages 776–778. IEEE, 2000.

[62] Jong-Sen Lee. Digital image enhancement and noise filtering by use of local statistics. *Pattern Analysis and Machine Intelligence, IEEE Transactions on*, (2):165–168, 1980.

[63] Jong-Sen Lee. Refined filtering of image noise using local statis-

tics. *Computer graphics and image processing*, 15(4):380–389, 1981.

[64] Jong-Sen Lee. Digital image smoothing and the sigma filter. *Computer Vision, Graphics, and Image Processing*, 24(2):255–269, 1983.

[65] Jong-Sen Lee, Mitchell R Grunes, Dale L Schuler, Eric Pottier, and Laurent Ferro-Famil. Scattering-model-based speckle filtering of polarimetric sar data. *Geoscience and Remote Sensing, IEEE Transactions on*, 44(1):176–187, 2006.

[66] Jong-Sen Lee, Karl W Hoppel, Stephen Mango, Allen R Miller, et al. Intensity and phase statistics of multilook polarimetric and interferometric sar imagery. *Geoscience and Remote Sensing, IEEE Transactions on*, 32(5):1017–1028, 1994.

[67] Jong-Sen Lee, Konstantinos P Papathanassiou, Thomas L Ainsworth, Mitchell R Grunes, and Andreas Reigber. A new technique for noise filtering of sar interferometric phase images. *Geoscience and Remote Sensing, IEEE Transactions on*, 36(5):1456–1465, 1998.

[68] Jong-Sen Lee, Jen-Hung Wen, Thomas L Ainsworth, Kun-Shan Chen, and Alex Jianzhong Chen. Improved sigma filter for speckle filtering of sar imagery. *Geoscience and Remote Sensing, IEEE Transactions on*, 47(1):202–213, 2009.

[69] ZW Li, XL Ding, Cheng Huang, JJ Zhu, and YL Chen. Improved filtering parameter determination for the goldstein radar interferogram filter. *ISPRS Journal of Photogrammetry and Remote Sensing*, 63(6):621–634, 2008.

[70] A Lopes, E Nezry, R Touzi, and H Laur. Structure detection and

statistical adaptive speckle filtering in sar images. *International Journal of Remote Sensing*, 14(9):1735–1758, 1993.

[71] Armand Lopes, Ridha Touzi, and E Nezry. Adaptive speckle filters and scene heterogeneity. *Geoscience and Remote Sensing, IEEE Transactions on*, 28(6):992–1000, 1990.

[72] Carlos Lopez-Martinez and Xavier Fabregas. Modeling and reduction of sar interferometric phase noise in the wavelet domain. *Geoscience and Remote Sensing, IEEE Transactions on*, 40(12):2553–2566, 2002.

[73] Giuseppe Masi, Giuseppe Scarpa, Raffaele Gaetano, and Giovanni Poggi. A watershed-based segmentation technique for multiresolution data. In *Image Analysis and Processing–ICIAP 2013*, pages 241–250. Springer Berlin Heidelberg, 2013.

[74] Didier Massonnet, Marc Rossi, Cesar Carmona, Frederic Adragna, Gilles Peltzer, Kurt Feigl, and Thierry Rabaute. The displacement field of the landers earthquake mapped by radar interferometry. *Nature*, 364(6433):138–142, 1993.

[75] Yasuyuki Matsushita and Stephen Lin. A probabilistic intensity similarity measure based on noise distributions. In *Computer Vision and Pattern Recognition, 2007. CVPR'07. IEEE Conference on*, pages 1–8. IEEE, 2007.

[76] M Kivanc Mihcak, Igor Kozintsev, and Kannan Ramchandran. Spatially adaptive statistical modeling of wavelet image coefficients and its application to denoising. In *Acoustics, Speech, and Signal Processing, 1999. Proceedings., 1999 IEEE International Conference on*, volume 6, pages 3253–3256. IEEE, 1999.

[77] Peyman Milanfar. A tour of modern image filtering: New in-

sights and methods, both practical and theoretical. *Signal Processing Magazine, IEEE*, 30(1):106–128, 2013.

[78] Alberto Moreira, Pau Prats-Iraola, Marwan Younis, Gerhard Krieger, Irena Hajnsek, and Konstantinos P Papathanassiou. A tutorial on synthetic aperture radar. *Geoscience and Remote Sensing Magazine, IEEE*, 1(1):6–43, 2013.

[79] Victor D Navarro-Sanchez and Juan M Lopez-Sanchez. Spatial adaptive speckle filtering driven by temporal polarimetric statistics and its application to psi. *Geoscience and Remote Sensing, IEEE Transactions on*, 52(8):4548–4557, 2014.

[80] J-M Nicolas, F Tupin, and H Maître. Smoothing speckled sar images by using maximum homogeneous region filters: An improved approach. In *Geoscience and Remote Sensing Symposium, 2001. IGARSS'01. IEEE 2001 International*, volume 3, pages 1503–1505. IEEE, 2001.

[81] Chris Oliver and Shaun Quegan. *Understanding synthetic aperture radar images*. SciTech Publishing, 2004.

[82] A. Papoulis. Probability, random variables and stochastic processes. *McGraw-Hill*, 1965.

[83] A. Parizzi and R. Brcic. Adaptive insar stack multilooking exploiting amplitude statistics: A comparison between different techniques and practical results. *IEEE Geoscience and Remote Sensing Letters*, 8(3):441–445, 2001.

[84] Sara Parrilli, Mariana Poderico, Cesario Vincenzo Angelino, and Luisa Verdoliva. A nonlocal sar image denoising algorithm based on llmmse wavelet shrinkage. *Geoscience and Remote Sensing, IEEE Transactions on*, 50(2):606–616, 2012.

[85] Antonio Pepe and Riccardo Lanari. On the extension of the

minimum cost flow algorithm for phase unwrapping of multitemporal differential sar interferograms. *Geoscience and Remote Sensing, IEEE Transactions on*, 44(9):2374–2383, 2006.

[86] G Poggi, F Sica, L Verdoliva, G Fornaro, D Reale, and S Verde. Non-local methods for filtering interferometric sar datasets. In *Advances in Radar and Remote Sensing (TyWRRS), 2012 Tyrrhenian Workshop on*, pages 136–139. IEEE, 2012.

[87] C Prati and F Rocca. Limits to the resolution of elevation maps from stereo sar images. *TitleREMOTE SENSING*, 11(12):2215–2235, 1990.

[88] Claudio Prati and E Rocca. Improving slant-range resolution with multiple sar surveys. *Aerospace and Electronic Systems, IEEE Transactions on*, 29(1):135–143, 1993.

[89] Diego Reale, Walter Franze, Antonio Pauciullo, Francescopaolo Sica, Simona Verde, and Gianfranco Fornaro. Detection of single scatterers in multilook sar tomography. In *Urban Remote Sensing Event (JURSE), 2015 Joint*, pages 1–4. IEEE, 2015.

[90] E Rodriguez and JM Martin. Theory and design of interferometric synthetic aperture radars. In *Radar and Signal Processing, IEE Proceedings F*, volume 139, pages 147–159. IET, 1992.

[91] Giuseppe Scarpa, Giuseppe Masi, Raffaele Gaetano, Luisa Verdoliva, and Giovanni Poggi. Dynamic hierarchical segmentation of remote sensing images. In *Image Analysis and Processing–ICIAP 2013*, pages 371–380. Springer Berlin Heidelberg, 2013.

[92] Marius Schmitt, Johannes L Schonberger, and Uwe Stilla. Adaptive covariance matrix estimation for multi-baseline insar data stacks. *Geoscience and Remote Sensing, IEEE Transactions on*, 52(11):6807–6817, 2014.

[93] Marius Schmitt and Uwe Stilla. Adaptive multilooking of airborne ka-band multi-baseline insar data of urban areas. In *Geoscience and Remote Sensing Symposium (IGARSS), 2012 IEEE International*, pages 7401–7404. IEEE, 2012.

[94] Marius Schmitt and Uwe Stilla. Adaptive multilooking of airborne single-pass multi-baseline insar stacks. *Geoscience and Remote Sensing, IEEE Transactions on*, 52(1):305–312, 2014.

[95] MS Seymour and IG Cumming. Maximum likelihood estimation for sar interferometry. In *Geoscience and Remote Sensing Symposium, 1994. IGARSS'94. Surface and Atmospheric Remote Sensing: Technologies, Data Analysis and Interpretation., International*, volume 4, pages 2272–2275. IEEE, 1994.

[96] F Sica, L Alparone, F Argenti, G Fornaro, A Lapini, and D Reale. Benefits of blind speckle decorrelation for insar processing. In *SPIE Remote Sensing*, pages 92430D–92430D. International Society for Optics and Photonics, 2014.

[97] Francescopaolo Sica, Diego Reale, Giovanni Poggi, Luisa Verdoliva, and Gianfranco Fornaro. Nonlocal adaptive multilooking in sar multipass differential interferometry. *Selected Topics in Applied Earth Observations and Remote Sensing, IEEE Journal of*, 8(4):1727–1742, 2015.

[98] Rui Song, Huadong Guo, Guang Liu, Zbigniew Perski, and Jinghui Fan. Improved goldstein sar interferogram filter based on empirical mode decomposition. *Geoscience and Remote Sensing Letters, IEEE*, 11(2):399–403, 2014.

[99] Rui Song, Huadong Guo, Guang Liu, Zbigniew Perski, Huanyin Yue, Chunming Han, and Jinghui Fan. Improved goldstein sar interferogram filter based on adaptive-neighborhood technique.

Geoscience and Remote Sensing Letters, IEEE, 12(1):140–144, 2015.

[100] Michael A Stephens. Use of the kolmogorov-smirnov, cramér-von mises and related statistics without extensive tables. *Journal of the Royal Statistical Society. Series B (Methodological)*, pages 115–122, 1970.

[101] Zhiyong Suo, Zhenfang Li, and Zheng Bao. A new strategy to estimate local fringe frequencies for insar phase noise reduction. *Geoscience and Remote Sensing Letters, IEEE*, 7(4):771–775, 2010.

[102] Zhiyong Suo, Jinqiang Zhang, Ming Li, Qingjun Zhang, and Chao Fang. Improved insar phase noise filter in frequency domain.

[103] Tanja Teuber and Annika Lang. A new similarity measure for nonlocal filtering in the presence of multiplicative noise. *Computational Statistics & Data Analysis*, 56(12):3821–3842, 2012.

[104] Carlo Tomasi and Roberto Manduchi. Bilateral filtering for gray and color images. In *Computer Vision, 1998. Sixth International Conference on*, pages 839–846. IEEE, 1998.

[105] R Touzi. Estimation of stationary and nonstationary coherence in sar imagery. In *Geoscience and Remote Sensing Symposium Proceedings, 1998. IGARSS'98. 1998 IEEE International*, volume 5, pages 2659–2661. IEEE, 1998.

[106] Ridha Touzi, Armand Lopes, Jérôme Bruniquel, and Paris W Vachon. Coherence estimation for sar imagery. *Geoscience and Remote Sensing, IEEE Transactions on*, 37(1):135–149, 1999.

[107] Emmanuel Trouvé, Marcello Caramma, and Henri Maître.

Fringe detection in noisy complex interferograms. *Applied Optics*, 35(20):3799–3806, 1996.

[108] Emmanuel Trouve, Jean-Marie Nicolas, and Henri Maitre. Improving phase unwrapping techniques by the use of local frequency estimates. *Geoscience and Remote Sensing, IEEE Transactions on*, 36(6):1963–1972, 1998.

[109] Fawwaz T Ulaby, Richard K Moore, Adrian K Fung, and Artech House. *Microwave remote sensing: active and passive*, volume 1. Addison-Wesley Reading, MA, 1981.

[110] Lars MH Ulander and J Askne. Repeat-pass sar interferometry over forested terrain. *Geoscience and Remote Sensing, IEEE Transactions on*, 33(2):331–340, 1995.

[111] Gabriel Vasile, Emmanuel Trouvé, Jong-Sen Lee, and Vasile Buzuloiu. Intensity-driven adaptive-neighborhood technique for polarimetric and interferometric sar parameters estimation. *Geoscience and Remote Sensing, IEEE Transactions on*, 44(6):1609–1621, 2006.

[112] Gabriel Vasile, Emmanuel Trouvé, Ivan Petillot, Philippe Bolon, Jean-Marie Nicolas, Michel Gay, Jocelyn Chanussot, Tania Landes, Pierre Grussenmeyer, Vasile Buzuloiu, et al. High-resolution sar interferometry: Estimation of local frequencies in the context of alpine glaciers. *Geoscience and Remote Sensing, IEEE Transactions on*, 46(4):1079–1090, 2008.

[113] Luisa Verdoliva, Raffaele Gaetano, Giuseppe Ruello, and Giovanni Poggi. Optical-driven nonlocal sar despeckling. *Geoscience and Remote Sensing Letters, IEEE*, 12(2):314–318, 2015.

[114] Nan Wu, Da-Zheng Feng, and Junxia Li. A locally adaptive

filter of interferometric phase images. *Geoscience and Remote Sensing Letters, IEEE*, 3(1):73–77, 2006.

[115] H. Xie, L. Pierce, and F. Ulaby. Statistical properties of logarithmically transformed speckle. *IEEE Transactions on Geoscience and Remote Sensing*, 40(3):721–727, 2002.

[116] Leonid Yaroslavsky. *Digital picture processing: an introduction*, volume 9. Springer Science & Business Media, 2012.

[117] Qifeng Yu, Xia Yang, Sihua Fu, Xiaolin Liu, and Xiangyi Sun. An adaptive contoured window filter for interferometric synthetic aperture radar. *Geoscience and Remote Sensing Letters, IEEE*, 4(1):23–26, 2007.

[118] Howard Zebker, John Villasenor, et al. Decorrelation in interferometric radar echoes. *Geoscience and Remote Sensing, IEEE Transactions on*, 30(5):950–959, 1992.

[119] Howard A Zebker and Richard M Goldstein. Topographic mapping from interferometric synthetic aperture radar observations. *Journal of Geophysical Research: Solid Earth*, 91(B5):4993–4999, 1986.

[120] Chaoying Zhao, Qin Zhang, Xiaoli Ding, and Jing Zhang. An iterative goldstein sar interferogram filter. *International journal of remote sensing*, 33(11):3443–3455, 2012.

[121] Xiao Xiang Zhu, Richard Bamler, Marie Lachaise, Fathalrahman Adam, Yilei Shi, and Michael Eineder. Improving tandem-x dems by non-local insar filtering. In *EUSAR 2014; 10th European Conference on Synthetic Aperture Radar; Proceedings of*, pages 1–4. VDE, 2014.

Acknowledgments

This thesis work would not have been possible without the support of my supervisors: Prof. Giovanni Poggi and Prof. Annalisa Verdoliva at University of Naples "Federico II", Dr. Gianfranco Fornaro and Dr. Diego Reale that guided my research work at the *Istituto per il Rilevamento Elettromagnetico dell'Ambiente* IREA-CNR. I thank Prof. Xiaoxiang Zhu and Prof. Richard Bamler, for giving me the opportunity to spend a year at the MF Institute of the *Deutsches Zentrum für Luft- und Raumfahrt* (DLR) working with them and their research group. It has been a great experience, both under a professional and a human point of view.